

Quasar detection
in the
UBC-NASA multi-narrowband survey.

by

KATIA BRAGLIA

Laurea in Astronomia, Universita' degli Studi di Bologna, Italy, 1999

A THESIS SUBMITTED IN PARTIAL FULFILMENT OF
THE REQUIREMENTS FOR THE DEGREE OF

MASTER OF SCIENCE

in

THE FACULTY OF GRADUATE STUDIES

(Department of Physics and Astronomy)

We accept this thesis as conforming
to the required standard

THE UNIVERSITY OF BRITISH COLUMBIA

August 11, 2002

© KATIA BRAGLIA, 2002

In presenting this thesis in partial fulfilment of the requirements for an advanced degree at the University of British Columbia, I agree that the Library shall make it freely available for reference and study. I further agree that permission for extensive copying of this thesis for scholarly purposes may be granted by the head of my department or by his or her representatives. It is understood that copying or publication of this thesis for financial gain shall not be allowed without my written permission.

Department of Physics and Astronomy

The University Of British Columbia
Vancouver, Canada

Date 08/13/2002

ABSTRACT

The goal of this thesis is to select quasars by applying a novel analysis to the UBC-NASA Multi-Narrow band Survey (UNMS1) catalog. The database consists of drift-scan observations taken with the 3-m NASA Liquid Mirror Telescope (LMT) in 1996-1997 and in 1999, using 35 narrow band filters, from 4500 to 9500 Å, and 4 broad bands (B , V , R , I), necessary for calibration purposes.

The method presented here is based on the comparison between UNMS1 catalog sources and stellar, galaxy, and quasar templates through a χ^2 minimization procedure combined with Bayesian analysis. The χ^2 parameter is useful to determine which model is the best fit for an observed Spectral Energy Distribution (SED); the odds ratio parameter, from the Bayes' theorem, is necessary in order to know the most likely category the source belongs, and it involves information such as the number of models for each category and the surface densities of stars, galaxies and quasars at a given magnitude.

After the method was applied to templates, treated as test-objects, it is concluded that more than 85% of quasar candidates, selected with at least 30 filter measurements, are correctly classified: the misclassification is due mostly to the similarity between stellar models and quasars when important spectral features are missed.

Of all the 39040 selected sources, 3056 quasar candidates were identified:

most of them have typical redshift ($z \sim 0.3 - 4$), apparent V magnitude ($V \sim 16 - 20$) and spectral index ($\alpha \sim -2 - 0.8$), but there is also a non-negligible number of objects localized well outside these ranges. Analysing the position of these sources in the redshift - V magnitude plane, redshift - spectral index plane and V magnitude - spectral index plane, it is possible to identify misclassified quasars and remove them away from the sample.

The final list of quasar candidates includes 2294 objects, among which 1 is in common with Veron's quasar catalog.

CONTENTS

ABSTRACT	ii
CONTENTS	iv
LIST OF TABLES	vii
LIST OF FIGURES	ix
I THESIS	1
1 INTRODUCTION	2
1.1 RECENT SURVEYS AND METHODS TO FIND QUASARS.	5
2 LIQUID MIRROR TELESCOPES.	13
2.1 LIQUID MIRROR TELESCOPES IN THE PAST.	13
2.2 THE NODO LIQUID MIRROR TELESCOPE.	15
2.3 DATA COLLECTION.	17
2.4 LMT ADVANTAGES.	19
2.5 LMT DISADVANTAGES.	20
2.6 LMT TECHNICAL ISSUES.	22
2.7 DATA ANALYSIS.	23
2.7.1 OBJECT DETECTION AND PHOTOMETRY.	23

2.7.2	ASTROMETRIC AND PHOTOMETRIC CALIBRATION.	25
2.7.3	THE OBJECT CATALOG.	26
2.8	CHARACTERISTICS OF THE SURVEY.	27
2.8.1	PHOTOMETRIC SELECTION CRITERIA.	30
3	QUASI STELLAR OBJECTS.	33
3.1	QSO'S FUNDAMENTAL CHARACTERISTICS.	33
3.2	QSO STRUCTURE.	38
4	THE UNMS QUASAR SURVEY.	41
4.1	THE UNMS1 CATALOG.	41
4.2	METHOD.	44
4.3	TEMPLATES.	48
4.3.1	STELLAR TEMPLATES.	48
4.3.2	GALAXY TEMPLATES.	50
4.3.3	QUASAR TEMPLATES.	51
4.4	METHOD CALIBRATION FROM TEMPLATES.	58
4.4.1	A FIRST ANALYSIS.	60
4.4.2	χ^2 MINIMIZATION METHOD AND ODDS RATIO PROCEDURE APPLIED TO ORIGINAL TEMPLATES.	66
4.4.3	χ^2 AND ODDS RATIO PROCEDURES APPLIED TO ALTERED TEMPLATES.	77
5	QUASARS IN THE UNMS1 CATALOG.	98
5.1	RESULTS.	98
5.1.1	STELLAR CANDIDATES IN THE UNMS SURVEY.	99

5.1.2	GALAXY CANDIDATES IN THE UNMS SURVEY. . .	100
5.2	PROPERTIES OF QUASAR CANDIDATES.	107
5.2.1	THE NUMBER - REDSHIFT DISTRIBUTION. . . .	107
5.2.2	THE NUMBER - APPARENT V MAGNITUDE DIS- TRIBUTION.	110
5.2.3	THE NUMBER - SPECTRAL INDEX α DISTRIBU- TION.	112
5.3	DISCUSSION.	114
5.4	QUASAR CANDIDATES.	119
5.5	IDENTIFICATION.	123
6	SUMMARY AND CONCLUSIONS.	124
	BIBLIOGRAPHY	127

LIST OF TABLES

1.1	Area covered, epoch, magnitude, $\Delta\lambda$ and number of expected or detected quasar candidates for the most recent optical QSO surveys.	6
2.1	Filter specifications. (a) mean wavelength (nm), from transmission curve; (b) bandwidth (nm): equivalent width/central transmission; (c) log of central frequency (Hz): $c/\text{mean wavelength}$; (d) log frequency bandwidth: $0.434 \times \text{bandwidth}/\text{mean wavelength}$; (e) central transmission; (f) equivalent width (nm): integral of transmission curve.	29
3.1	Inventory of emission lines [23].	37
4.1	Parameters in the UNMS1 catalog.	42
4.2	Flux corrections by Remi Cabanac [priv. comm.].	43
4.3	Surface densities for stars, galaxies and quasars in the broad bands: the units are num/deg^2 for the B and I filters, and num/deg^2 0.5 mag in the R and V bands. The “a” case is for $B < 19.5$ and the “b” is for $B > 19.5$	47
4.4	Parameters in Pickles’ stellar library.	49
4.5	Spectral templates from Kinney & Calzetti galaxies’ library. .	51
4.6	Fitted power-law index.	54

4.7	Power-law index in frequency and wavelength for quasar templates in the UV and optical-near-infrared (Optical-IR) region.	58
4.8	Template sequence for the χ^2 analysis.	69
5.1	Star, galaxy and quasar identifications.	98
5.2	Conversion table between stellar type and number.	102
5.3	Logarithmic star counts [$\# / 10^4 pc^3$] by stellar type and luminosity class from data published in Allen (1973) [1].	102
5.4	Logarithmic star counts [$\# / 10^4 pc^3$] for candidates found in the LMT survey.	103
5.5	Conversion table between galaxy type and number.	103
5.6	Fraction of ellipticals (E), S0 galaxies, Sa+Sb, Sc+Sd and Sm spirals, Irregular (Im) galaxies, Starburst (SB1-6) and UVhot galaxies in the CfA1, CfA2 and LMT galaxy samples.	105
5.7	Equatorial coordinates (RA, DEC), apparent V magnitude and redshift z for the quasar common to Veron's catalog and UNMS1 quasar catalog.	123
6.1	Distribution of star, galaxy and quasar candidates.	125

LIST OF FIGURES

1.1	Evolution of telescope aperture over time.	4
1.2	Two-colour diagram: quasars (points) are well separated by main sequence stars (line with stellar types B0 - M0) (http://ned www.ipac.caltech.ca/Cambridge/Cambridge_1.3.3.html). . . .	9
2.1	Components for a liquid mirror.	16
2.2	Basic optical layout for the UBC-Laval 2.7-m liquid mirror telescope.	18
2.3	Filter transmission curves.	31
3.1	General layout for a quasar spectrum.	35
3.2	Structure of AGN's inner region (http:// nedwww.ipac.caltech. edu/level5/Urryl/UrrylPl.html).	39
4.1	Corrections with the best fit curve.	44
4.2	Kinney-Calzetti's galaxy templates normalized at 4000 Å. . . .	52
4.3	Composite spectrum of 101 quasars, binned to 2 Å.	53
4.4	Composite spectrum: power law fits to the estimated flux are shown.	55
4.5	First part of the composite spectrum in the 300-3400 Å range: it can be noted that the Ly α (1215 Å) and CIV (1549 Å) are among the strongest emission lines.	56

4.6	Second part of the composite “flat” spectrum in the 3400-8550 Å range. H α (6563 Å) and [OIII] (4363 Å) are among the strongest emission lines.	57
4.7	Quasar templates in the rest frame: lines I, II, III and IV represent respectively template I, II, III and IV.	59
4.8	Galactic (blue line) and quasar (red line) templates in the rest frame with Supergiant star templates (green line).	61
4.9	Galactic (blue line) and quasar (red line) templates in the rest frame with bright giant templates (green line).	62
4.10	Galactic (blue line) and quasar (red line) templates in the rest frame with different giant star templates (green line).	63
4.11	Galactic (blue line) and quasar (red line) templates in the rest frame with different subgiant star templates (green line).	64
4.12	Galactic (blue line) and quasar (red line) templates in the rest frame with different main sequence star templates (green line).	65
4.13	Galactic (blue line) and quasar (red line) templates at redshift $z=1.2$ with supergiant star templates (green line).	66
4.14	Galactic (blue line) and quasar (red line) templates at redshift $z=1.2$ with bright giant star templates (green line).	67
4.15	Galactic (blue line) and quasar (red line) templates at redshift $z=1.2$ with giant star templates (green line).	70
4.16	Galactic (blue line) and quasar (red line) templates at redshift $z=1.2$ with sub-giant star templates (green line).	71
4.17	Galactic (blue line) and quasar (red line) templates at redshift $z=1.2$ with main sequence stars (green line).	72

4.18 χ^2 distribution for 4 QSO N.14 at $z=0.3$: line I, II and III come from the comparison respectively to galactic, quasar and stellar templates.	73
4.19 χ^2 distribution for QSO N.15 at $z=1.4$: line I, II and III come from the comparison respectively to galactic, quasar and stellar templates.	74
4.20 χ^2 distribution for QSO N.16 at $z=3.5$: line I, II and III come from the comparison respectively to galactic, quasar and stellar templates.	75
4.21 χ^2 distribution for QSO N.17 at $z=5.6$: line I, II and III come from the comparison respectively to galactic, quasar and stellar templates.	76
4.22 χ^2 distribution for the altered QSO N.14 at $z=0.3$: line I, II and III come from the comparison respectively to galactic, quasar and stellar templates.	78
4.23 χ^2 distribution for the altered QSO N.15 at $z=1.4$: line I, II and III come from the comparison respectively to galactic, quasar and stellar templates.	79
4.24 χ^2 distribution for the altered QSO N.16 at $z=3.5$: line I, II and III come from the comparison respectively to galactic, quasar and stellar templates.	80
4.25 χ^2 distribution for the altered QSO N.17 at $z=5.6$: line I, II and III come from the comparison respectively to galactic, quasar and stellar templates.	81

4.26	Distribution of stellar (hexagon), galaxian (cross) and quasar (triangle) template-objects as classified according to the odds ratio method.	83
4.27	Normalized distribution for correctly classified stars (hexagon) and for objects wrongly classified as stars (cross).	84
4.28	Normalized distribution in the redshift range $z=0-0.6$ for correctly classified galaxies (hexagon) and for objects wrongly classified as galaxies (cross).	85
4.29	Normalized distribution in the redshift range $z=0-0.6$ for correctly classified quasars (hexagon) and for objects wrongly classified as quasars (cross).	86
4.30	Normalized distribution in the redshift range $z=0-0.6$ for correctly classified galaxies (hexagon) and for objects wrongly classified as galaxies (cross).	87
4.31	Normalized distribution in the redshift range $z=0.6-1.2$ for correctly classified quasars (hexagon) and for objects wrongly classified as quasars (cross).	88
4.32	Normalized distribution in the redshift range $z=1.2-4.1$ for correctly classified quasars (hexagon) and for objects wrongly classified as quasars (cross).	89
4.33	Normalized distribution in the redshift range $z=4.1-7$ for correctly classified quasars (hexagon) and for objects wrongly classified as quasars (cross).	90

4.34	Normalized odds ratio distribution for a Sa spiral galaxy (N.4) at redshift 0.2, 0.6, 0.8 and 1.2 in favor of stellar (hexagon), galactic (cross) and quasar (triangle) template.	92
4.35	Normalized odds ratio distribution for a starburst galaxy (N.7) at redshift 0.2, 0.6, 0.8 and 1.2. in favour of stellar (hexagon), galactic (cross) and quasar (triangle) template.	93
4.36	Normalized odds ratio distribution for QSO N.14 at redshift 0.3, 2.1, 4.2 and 7.in favour of stellar (hexagon), galactic (tri- angle) and quasar (cross) template.	94
4.37	Normalized odds ratio distribution for QSO N.15 at redshift 0.3, 2.1, 4.2 and 7. in favour of stellar (hexagon), galactic (triangle) and quasar (cross) template.	95
4.38	Normalized odds ratio distribution for QSO N.16 at redshift 0.3, 2.1, 4.2 and 7.in favour of stellar (hexagon), galactic (tri- angle) and quasar (cross) template.	96
4.39	Normalized odds ratio distribution for QSO N.17 at redshift 0.3, 2.1, 4.2 and 7.in favour of stellar (hexagon), galactic (tri- angle) and quasar (cross) template.	97
5.1	Star counts by spectral types.	99
5.2	Galaxy distribution by the morphological type.	104
5.3	Distribution of galaxy counts with spectral type and redshift. .	106
5.4	Redshift distribution of quasar candidates.	108
5.5	The redshift distribution for quasars in the Hewett&Burbidge catalog (top) and in the Sloan Sky Survey catalog (bottom). .	109
5.6	The V magnitude distribution for quasar candidates.	111

5.7	The V magnitude distribution from the Hewett&Burbidge catalog.	112
5.8	Spectral index distribution for quasar candidates in the UNMS1 catalog.	114
5.9	The spectral index distribution by Warren et al. (top picture, upper line) and by Francis et al. (bottom).	115
5.10	Quasar candidates in the redshift - V magnitude plane. . . .	117
5.11	Quasar candidates in the redshift - spectral index plane. . . .	118
5.12	Quasar candidates in the spectral index - V magnitude plane.	119
5.13	The number - redshift distribution for the "cleaned" set of quasars.	120
5.14	The number - V magnitude distribution for the "cleaned" set of quasars.	121
5.15	The number - α distribution for the "cleaned" set of quasars. .	122

PART I

Thesis

CHAPTER 1

INTRODUCTION

Quasars were first discovered in 1963, when several faint radio sources inside the 3rd Cambridge Catalogue of Discrete Radio Sources (3C) were identified as optical objects undistinguishable from stars [13]. Their diameters, smaller than 1 arc sec, indicated an unusually high surface brightness in the optical and radio spectral regions. Their positions, away from the galactic equator, suggested an extragalactic nature.

The name *quasar* (*quasi stellar radio source*) was coined because of their stellar appearance and the fact that their radio emission is comparable to that of Cygnus A.

The first discovered quasar was 3C 273 [62], a star-like source identified as the optical counterpart of a radio galaxy whose position was known accurately. First considered a stellar object, its real extragalactic nature became clear only after Alan Sandage saw broad emission lines at positions unusual for stars and M. Schmidt identified a continuum and strong emission features with redshift $z=0.158$, implying a distance around 950 Mpc [73].

In 1965 Sandage and Veron [61], working on the identification of radio sources, realized that there were many galaxies very similar to stars on photographic plates, having a compact structure, a high surface brightness and weak radio emission or no emission at all. It was therefore necessary to distinguish between QSRs (Quasi Stellar Radio sources), with radio emission,

and QSOs (Quasi Stellar Objects), with little or no emission [13].

It was eventually realized how important these “new” objects were, not only as peculiar sources (as described in §3, they radiate an amount of energy around 10^{53} - 10^{55} Joule from regions as small as the Solar System), but also for their role in cosmology and for what could be understood about host galaxies, and the nature and properties of the material between the observer and the source.

The small angular size and faintness of QSOs is a challenge for their detection: the faintest objects can be investigated only by the largest telescopes, characterized by a greater light-gathering power and a superior resolution. The light-gathering power of a telescope depends on the objective’s area: the bigger it is, the more light is collected in a given time yielding bright images of even distant objects.

The telescope’s resolving power is the ability to reveal fine details: according to the formula

$$\theta = 1.22 \frac{\lambda}{D} \quad (1.1)$$

where θ is the angular distance between two bodies, λ is the observation wavelength and D is the primary mirror diameter, the resolving power can be improved either by increasing the diameter D or reducing the wavelength λ . Since the optical wavelength range of the electromagnetic spectrum spans from 4500 Å to 9500 Å, progress has come from larger diameters.

Fig 1.1 shows the evolution of telescope’s aperture over time: the diameter has increased slowly with time due to the difficulty of producing accurate optics (both in terms of casting the primary mirror substrate and of polishing

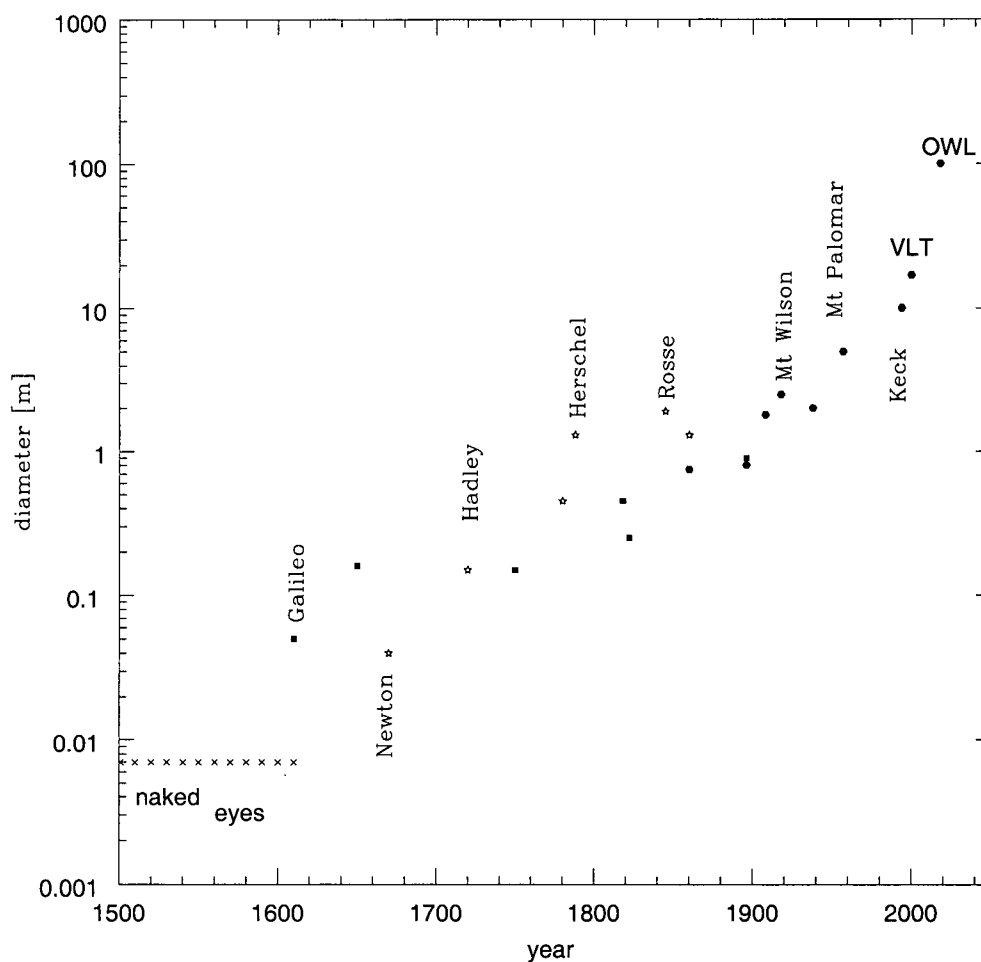


Figure 1.1: Evolution of telescope aperture over time.

it).

Sophisticated technology has overcome this problem, but more time has been necessary to improve the ground-based optical telescope resolution, proportionate to the diameter of the primary lens or mirror. Images produced by

large telescopes suffer various problems because of the Earth's atmosphere. Its turbulent nature causes density changes over small distances, creating regions where the light is refracted in nearly random directions; in this situation the image of a point source is effectively blurred.

Correctors to remove optical aberrations and adaptive optics to counter atmospheric turbulence are now functioning on most modern telescopes.

Though the liquid mirror telescope (LMT) technology still needs developments, the optics production and other factors (such as the mount, required to support telescopes often heavy and to move them with accuracy) are not an issue and this fact and other advantages, such as the low cost with respect to a conventional glass telescopes, make it a really interesting and alternative technological project, described in detail in chapter §2.

1.1 Recent surveys and methods to find quasars.

The scientific goal of this thesis is to find quasars using a novel method which is applied to a database of objects observed with the NASA LMT. Beside a detailed description of the method, it is also useful to compare this survey to those which characterized the last decade or earlier, with particular attention to the Sloan, and discuss briefly how they selected quasar candidates.

Table 1.1 shows the area, the epoch, the limiting magnitude, the spectral coverage and the number of objects found in the most important optical surveys.

The LMT-NODO survey is explained in detail in §2; nevertheless some

Survey	Ref.	Epoch	Area	magn	$\Delta\lambda$	quasars
			(deg ²)		Å	
MBQS	[52]	1978-1981	109	B17.6	3500-7000	32
PBQS	[63]	1981	10714	B16.2	U,B	114
PTQS	[65]	1985-1989	61	R22	4400-7500	232
LBQS	[34]	1986-1989	454	B19	3400-5100	1058
HNQS	[32]	1988-1998	14000	R18.6	3600-6500	376
HBQS	[18]	1989	153	B18.8	U,B,V,R	284
AAT	[11]	1989-1990	1.6	B21	3500-6400?	420
EQS	[27]	1989-1997	330	B18.5	U,B,V,R,I	224
AQS	[28]	1990	14019	R15.4	B,V,R	46
HSQS	[31]	1990-1994	10000	B17.5	3200-5400	160
FQS	[12]	1991	0.9	B22	U,b _j ,r _f ,I	66
APM1	[71]	1991-1995	2500	B19	B,R,I	31
SA94	[17]	1992	10	B19.9	U,B,V	200
LMT	[39]	1996-1999	20	B21.5	4500-9500	~ 3000
TQS	[64]	1997	20	B21.3	U,B,V	368
2dF	[68]	1997-2002	740	B20.9	U,B _j ,R	25000
SDSS	[79]	1998-...	10225	g23.3	4000-7500	10 ⁵
APM2	[72]	1999-2000	5500	B20.8	B _j ,R,I	31

Table 1.1: Area covered, epoch, magnitude, $\Delta\lambda$ and number of expected or detected quasar candidates for the most recent optical QSO surveys.

points can be made here.

Compared to these surveys, the limiting magnitude reached by the UBC-NASA Multiband Survey (UNMS1) catalog (21-22 mag in the most sensitive bands) is inferior only to those of the Palomar Transit (22 mag), Faint (22.3 mag) and Sloan Digital (23 mag) surveys. This means these surveys include fainter objects than those observed by the liquid mirror telescope.

Considering the sky area covered, regions observed by the LMT-NODO survey overlap those studied by the Sloan and the Hamburg North surveys.

Therefore, observations taken with the liquid mirror telescope are matched only by those of the Sloan survey. This fact, which could turn out useful since it can provide an independent confirmation of quasar candidates selected with the method described in §4, is not surprising: the Sloan Digital Sky Survey (SDSS) [79] is in fact one of the biggest surveys and quasar study (involving mainly quasar clustering effects, QSO evolution and association with galaxies) represents only one of the many fields of investigation (www.astro.princeton.edu/PBOOK/science/quasars.htm). Inside the group of 113 QSOs found so far, 27 have redshift $3.5 \leq z \leq 4.5$ and magnitude $18.55 \leq m_i \leq 20.97$, 4 have redshift $z \geq 4.95$; more than 100000 quasars are expected to be detected when the survey is completed. The method adopted to select quasars varies according to the redshift: at low redshifts ($z \leq 2.2$), the lack of a detectable Balmer jump in spectra helps to distinguish between QSOs and stars; at higher redshifts, the presence of the strong emission line $\text{Ly}\alpha$ and the absorption by the Ly forest cause the broadband colours of quasars to become increasingly redder with redshift. The Hamburg survey (HQS) [32] for the Northern sky and the first APM UKST colour survey

(APM1) [71] base their selection process on these absorption systems as well.

At $3.5 \leq z \leq 5$, quasars and stars occupy different zones of the $g'r'i'z'$ colour space (modified Thuan-Gunn system, see transmission curves in Fig. 1 of [29]) but at $z \geq 5$ the quasar track approaches the red end of the stellar locus in the $r'i'z'$ diagram and new discriminators are required. The selection method is then based on three regions in SDSS colour space:

- $r' - i' \geq 1.35$ and $i' - z' \leq 0.3$;
- $r' - i' \geq 2$ and $i' - z' \leq 0.7$;
- z -band detection only, i.e. $z' \leq 20.8$ and the detection in the other bands is below 5σ .

In addition, an object must be classified as a point source by the SDSS processing software and have $z' \leq 20.8$.

Surveys listed in Table 1.1 use other methods to select quasar candidates.

The ASIAGO-ESO/RASS QSO survey (AQS) [28], derived by merging the RASS (Rosat-All-Sky-Survey) [76], GSC (Guide Star Catalogue) [47], USNO (United States National Observatory) [54] and DSS (Digitized Sky Survey: <http://arch-http.hq.eso.org/dss/dss>) catalogs, found quasars according to their point appearance and a magnitude criterion: $11 \leq V_{GSC} \leq 14.5$ and $13.5 \leq R_{USNO} \leq 15.4$.

Common optical selection criteria are based on colours: in the two-colour diagram showed in Fig. 1.2, quasars are always much brighter in the ultraviolet than main sequence stars with the same $B-V$ colour and the threshold $U-B=-0.4$ is used to separate these two categories.

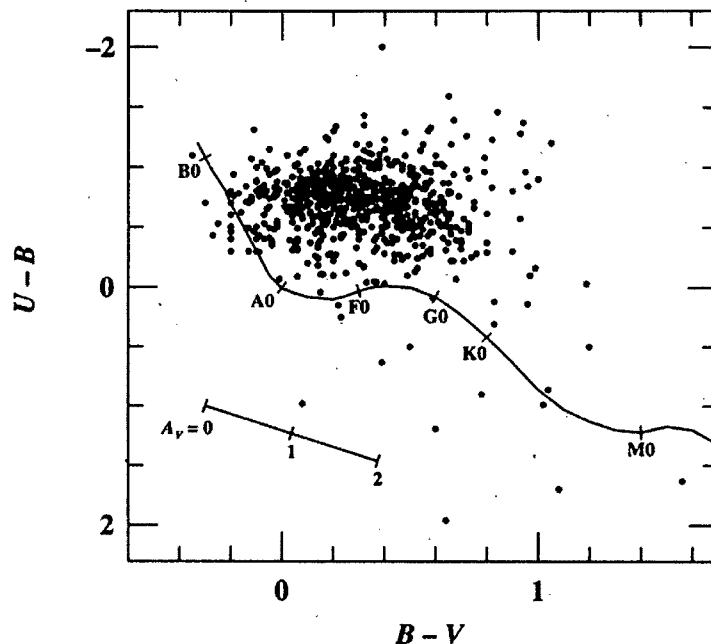


Figure 1.2: Two-colour diagram: quasars (points) are well separated by main sequence stars (line with stellar types B0 - M0) (http://nedwww.ipac.caltech.ca/Cambridge/Cambridge_1.3.3.html).

This method, used in the Palomar Bright QSO survey (PBSQ) [63], the Medium Bright Quasar survey (MBQS) [52], the Homogeneous bright QSO survey (HBQS) [18], the SA 94 QSO survey (SA94) [17] and the Anglo-Australian-Telescope survey (DURHAM/AAT) [11], must be used carefully as that quasar region inside the two-colour diagram is also well populated by white dwarfs that, at B magnitude smaller than 16, are much more numerous than quasars.

Other surveys rely on the red excess: the spectroscopic survey of faint QSOs (FQS) [12] and the second APM UKST colour survey (APM2) [72]

(for which only sources with $B_J - R \geq 2.5$ are considered quasar candidates), are an example.

Techniques with more colours can be more efficient: besides $U-B$ and $B-V$ colours, $U-J$ and $J-F$ (where J is at 12500 \AA and F is at 6250 \AA) are used. Quasars with redshift higher than 2.2 have a colour $J-F$ bluer than stars with the same $U-J$ colour. This method is adequate to find objects no more distant than $z \sim 3.2$.

Multicolour techniques with broader bands, already mentioned for the SDSS, are efficient to identify more distant quasars: this is the way in which the 2dF QSO Redshift survey (2dF) [68] (<http://www.2dfquasar.org>) operated as well.

Other research methods are based on broad lines: the spectrum of a quasar, with strong emission features, is very different, at low resolution, from that of red stars and galaxies. A Grism (grating-lens system), characterized by a prism objective associated to a diffraction grating, allow simultaneous measurements of low resolution spectra for many objects. This led to the discovery of quasars at redshift higher than 4 [22]. This is the case of the Large Bright QSO survey (LBQS) [34] and the Palomar Transit Grism survey (PTGS) [65].

Other possible methods to identify quasars could rely on their variability or on the absence of proper motions. These methods require long exposures on different time scales to separate possible candidates: the Tautenburg survey (TQS) [64] worked in fact on Schmidt plates taken over the last three decades.

Recently, the Principal Component Analysis approach (PCA) has resulted

in successful classification of objects such as stars, galaxies, QSOs etc. from multi-band photometry, using mock catalogs which match as closely as possible the observations of the Large Zenith Telescope (LZT), mentioned in §2 [15]. The PCA is a non-parametric approach already employed with multi-colour photometry (generally fewer than 10 colour bins) or with medium to high-resolution spectroscopy, but it was not tested on spectral energy distribution (SED) with $R \sim 40$.

The PCA methodology can be summarized in this way: from a set of N vectors “ f ” with M elements (where M is the number of filters) and each of them normalized to have unit scalar product, the PCA derives a set of orthogonal eigenvectors e_{λ_j} , using criteria of decreasing maximum variance of the spectra when projected onto the eigenvectors. Then, vectors f_{λ_i} are the linear combinations of eigenvectors e_{λ_j} (where e_1 is the mean vector over f_{λ_i} , e_2 lies in the direction of the highest variance orthogonal to e_1 , etc.) and eigencomponents y_{ij} which are the weight of the “ j^{th} ” eigenvector in the “ i^{th} ” vector.

The main advantage of this approach is that when the vectors f_{λ_i} are correlated (as it is for astronomical SEDs), most of the classification power of the linear combination mentioned above is carried by the first 10 eigenvectors (e_1, \dots, e_{10}) when describing a set of objects of different classes and at different redshift intervals.

In order to use the PCA for spectral classification, one must relate the internal correlations outlined by the PCA with the physical properties of the objects: it is necessary then to apply the PCA to mock catalogs of templates and extract important information for classifying objects and measuring their

redshifts. This was the approach chosen by [15] : once the principal eigen-components of the catalog are measured, the first 10 eigenvectors are used to defined a 10-dimensional eigenbasis, in which each class of objects occupies a given locus, defined by its spectral type among its class, and its redshift for galaxies and quasars. For a median signal-to-noise ratio of 6, 98% of stars, 100% of galaxies and 93% of quasars are correctly classified. This technique, tested only on simulated observations so far, is going to be calibrated on the same data studied in this thesis.

CHAPTER 2

LIQUID MIRROR TELESCOPES.

2.1 Liquid mirror telescopes in the past.

The idea of a liquid mirror telescope dates back to 1850, when a scientist at the Italian Observatory of Naples, Ernesto Capocci, thought to use for astronomical observations a well known physical concept according to which the equilibrium configuration of a liquid surface, which rotates uniformly, assumes just a paraboloid shape with a focal length f

$$f = g/2\omega^2 \quad (2.1)$$

where ω is the rotation angular frequency, g is the gravitational constant. Capocci realized that a highly-dense liquid, such as mercury, might be used as a reflecting surface.

The New Zealander Henry Skey, from the observatory of Dunedin, was the first to build such an instrument in 1872. Unfortunately, the fact it couldn't point and track objects, and complications related to a liquid such as mercury, prevented this kind of telescope from being useful for astronomical research until a century later.

Here is a brief list of the most important liquid mirror telescopes built in the past or still in the development phase [25]:

- in 1992, E. Borra created the first rotating mercury mirror, 1.5 m in diameter, that was able to produce diffraction limited images: it was followed by a second one with a diameter of 2.5 m;
- in March 1994, a 2.7-m telescope designed and built by P. Hickson was used for astronomical observations. Its resolution was limited only by the atmospheric seeing. It was equipped with a CCD operating in TDI mode [36], [37], [38];
- in the Spring of 1996, the 3-m Nasa Orbital Debris Observatory (NODO) built by M. Mulrooney and P. Hickson began operation;
- in 1997, a 3.7-m liquid mirror was completed by Borra [9]: its optical testing is on its way;
- the 6-m Large Zenith Telescope (LZT) was recently built by P. Hickson near Vancouver, British Columbia: it will be operational before the end of 2002.

One of the most ambitious projects for future LMT investigations is LAMA, the Large-Aperture Mirror Array: it is an optical interferometry project based on an array of 18 fixed 10-meter liquid-mirror telescopes, covering a circle of 60-m diameter and with an effective aperture ~ 42 m. Likely located either at an altitude of 5000 meters in Cerro Chajnantor, in Northern Chile or at an altitude of 2800 meters in the Sacramento Mountains of New Mexico, this instrumentation will produce distortion-free diffraction-limited images over a 1 arcmin instantaneous field of view, with pointing and tracking as far as 4° from the zenith (<http://www.astro.ubc.ca/LMT/lama/index.html>).

2.2 The NODO liquid mirror telescope.

The data analyzed and discussed in this thesis were obtained from the NODO liquid mirror telescope in the state of New Mexico, in the Sacramento mountains, at 2756 meters of altitude. This 3-m mirror with a 4.5-m focal length was built by P.Hickson and M. Mulrooney for NASA. The principal objective was to characterize orbital debris, with a second goal of astronomical research [57].

The most important component of the entire structure is the mirror support: a styrofoam core enclosed by Kevlar. This material was chosen because of its light weight, high stiffness, and good dampening characteristics. The Kevlar surface is covered by a layer of polyurethane, created by spincasting. The final surface, which is parabolic to within a fraction of a millimeter, is then covered by 1.5 mm of spinning mercury. A thin oxide layer forms over the surface after the mercury is exposed for a few hours to air and it has the advantages of dampening surface waves and eliminating the evaporation. The reflectivity of Mg is in the range 70 - 80%. The structure is able to support 170 kg of mercury without vibration and with a maximum deviation from a paraboloid around 0.1 mm. The deviation of the mercury surface from a perfect parabola is approximately $\lambda/20$, where λ is the wavelength.

To achieve this performance, there are two fundamental requirements: a stable rotational velocity and the rotation axis alignment parallel to the gravitational field of the Earth. The first requirement is obtained using a synchronous motor which drives the mirror support: the rotation period is approximately 6 seconds. The second requirement is achieved by employing a precise air bearing and a three-point mount with which the rotation axis

can be aligned to within 0.25 arcseconds [9].

The basic mirror setup is shown in Fig. 2.1.

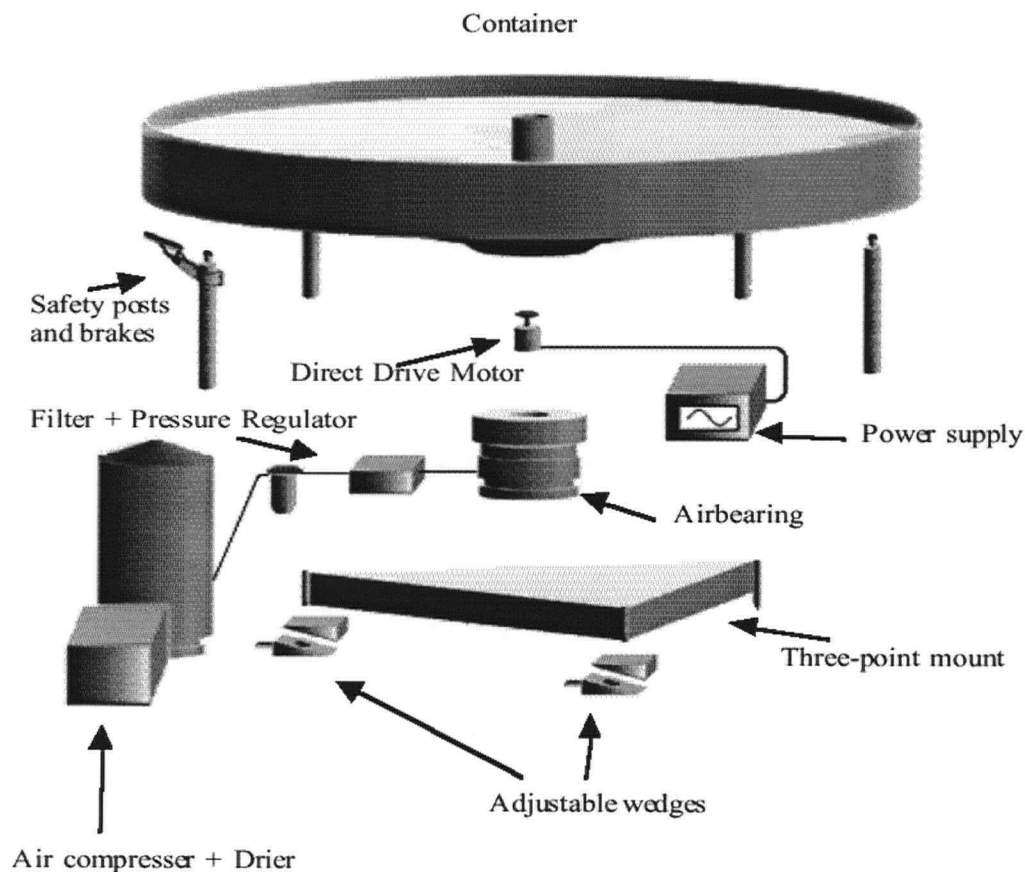


Figure 2.1: Components for a liquid mirror.

The telescope structure consists of a steel tripod 5.8 meters high which supports correcting lenses, filters, an alignment system, focus mechanism and a CCD camera.

The corrector contains 4 elements which reduce the optical aberrations (especially field distortions) to less than 1 arcsec over a 0.5° field at infrared

and optical wavelengths.

The NODO LMT's basic layout is similar to that shown Fig 2.2 for the UBC-Laval 2.7-m liquid mirror telescope: main differences are in the absence of the brace at half the height and of the drive belt. The drive system includes a motor stator (which is mounted directly on the air-bearing base), a rotor (which is attached to the rotating spindle) and an optical encoder (which senses the angular velocity).

2.3 Data collection.

A front illuminated 2048×2048 pixel Loral CCD (for 1996-1997 observations) and a back illuminated 1024×1024 SITE CCD (for 1999 observations) are the detectors used for this survey. The first chip, for which the light enters through thin polysilicon gates of the parallel register, is transparent to long wavelength and opaque for wavelengths shorter than 4000 \AA . The second device, for which the light enters through the thinned backside of the CCD register where there is no gate structure, exhibits high sensitivity to light up to the near-infrared regions of the spectrum due to its thickness reduced to $10 \text{ }\mu\text{m}$. Both devices don't show a good response in the blue. Each pixel has a size of $15 \text{ }\mu\text{m}$ with an image scale of 0.6 arcsec/pixel for the first detector, and a size of $24 \text{ }\mu\text{m}$ with an image scale of $0.96 \text{ arcsec/pixel}$ for the second detector, in right ascension and declination. The CCD is situated inside a Dewar and is cooled thermically to a temperature of -30°C , reducing the dark current level.

During observations, the CCD is scanned continuously in the time-delay

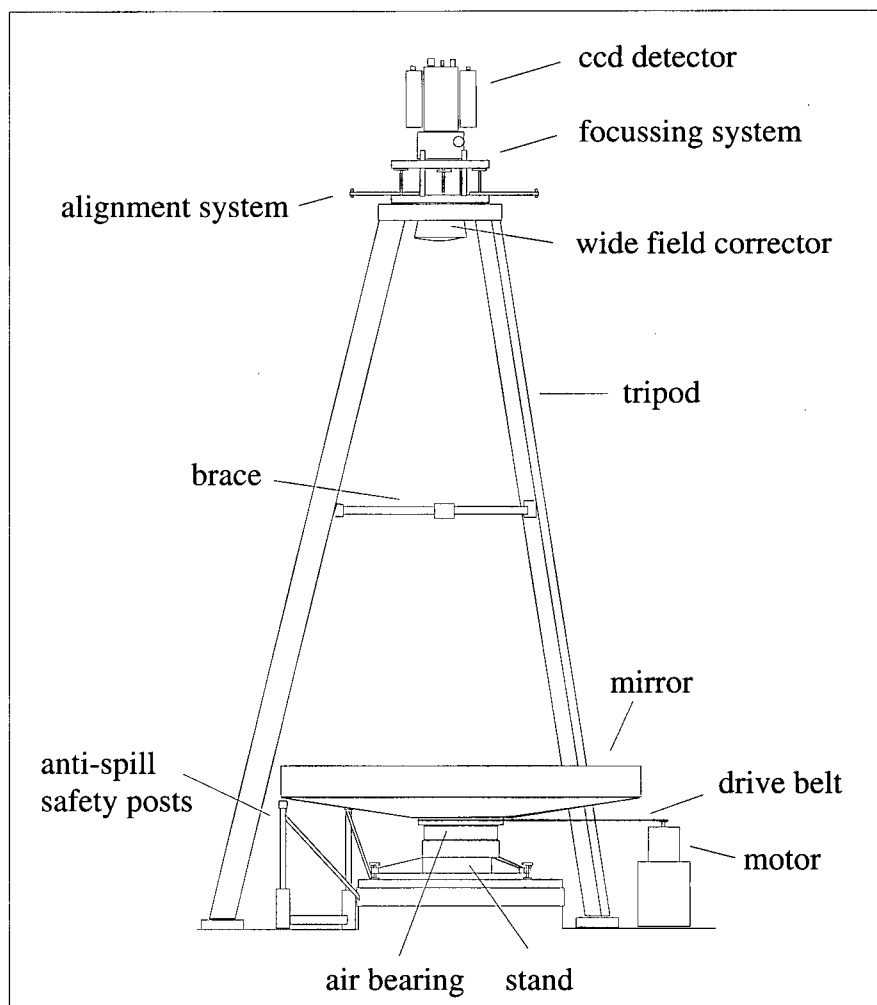


Figure 2.2: Basic optical layout for the UBC-Laval 2.7-m liquid mirror telescope.

integrate (TDI) mode [51]. In this operation, the charges accumulated by the CCD are moved across it at the siderial rate. The effective integration time is around 97 seconds for the 2048×2048 CCD and 78 seconds for the 1024×1024 CCD. This represents an object's cross in time along the chip due to our planet's rotation. Data are accumulated continuously at a rate of ~ 50 Kb/sec for a total of 1.8 Gb each night. Software written by P. Hickson supplies interactive control of data acquisition parameters and a continuous display of image data; zoom and contrast controls on the display allow one to monitor the focus and to check image quality during observations.

The Loral CCD is connected to a photometric controller which, being designed for high-speed operation (necessary for satellite debris observations), has a relatively-high read noise ($28e^-$); for the SITE CCD the read noise is of $11e^-$. This fact represents a limit for the detector, particularly at short wavelengths where the sky is not so luminous and the CCD does not have a good response [39]. This fact could influence the study of quasars in this thesis since the selection process is based on the comparison of the observed source and templates: if features in the blue are missed or not very accurate, it is likely to misclassify the source.

2.4 LMT advantages.

For clear reasons of construction, the LMT is a non-steerable instrument and it observes objects inside a narrow strip of sky passing through the zenith. Here we can find the first advantage: only zenith observations minimize the atmospheric extinction and refraction, allowing one to observe

with the best seeing.

The increasing interest in LMTs is justified by numerous practical advantages with respect to conventional telescopes: all the challenges related to the mounting, which supports most of the telescope weight, and to the trailing of celestial bodies, are here eliminated.

The simple general design of the entire instrument simplifies maintenance. Dust can be removed from the mirror surface in less than a hour losing a negligible amount of mercury: this allows one to use the telescope continuously with the opportunity of observing the variability of certain sources night by night.

LMTs are well-suited for many different kinds of surveys, from large-scale structure to galactic evolution, galaxy luminosity function evolution, QSO observations, supernovae rates, gravitational lenses and cosmology. All these research topics would be difficult to study continuously with conventional telescopes.

Most of the success of this type of instrument is due also to its low cost: an order of magnitude lower than a conventional telescope with the same aperture.

2.5 LMT disadvantages.

Since the liquid mirror rotates around a vertical axis, the field is limited to $\sim 0.5^\circ$ square near the zenith and, thanks to the terrestrial rotation, the survey studies a narrow strip of sky, whose extent depends on the integration time.

The mechanical disadvantages, such as the lack of tracking and directed pointing, might be overcome in the near future using correctors with movable optics [42], correctors with movable mirrors [8], introducing magnetic particles into the liquid and deforming its configuration through magnetic fields or using a viscous liquid, covered by a very thin reflecting film so that the instrument can point a few tens of degrees off the zenith without altering its parabolic shape [10].

Star-trail curvature, which affects observations away from the celestial equator, can be distinguished from other problems since these trails are lightly concave, to North direction, about an amount which depends on the size of the CCD and is practically constant over the entire field. At NODO latitude, the peak-to-edge curvature is around 3.3 arcsec. This problem could be avoided by using a corrector having tilted and decentred lenses [40]. For this telescope, the curvature produced by the rotation of the field is smaller than the average seeing, around 2 arcsec.

The field distortion, experienced by the NODO telescope with its original 3-elements corrector (later replaced by a low distortion 4-element design), is a more serious issue: it causes an increasing degree of image smearing from the center of the field to the extremities North and South (up to 2 degrees). Just for this reason the survey is limited to 75% of the field, starting from the center [39].

Different factors must be accounted for the image degradation: seeing, instrumental aberrations, and the TDI observation mode.

Aberrations of a parabolic mirror depend on the field angle: using the corrector, they are smaller than 1 arcsec, negligible with respect to the see-

ing.

The final contribution to the image aberration comes from TDI: this observation mode is necessary since the instrument does only zenith observations and then it is fundamental that images of all the sources drift at the same rate on parallel linear tracks, otherwise there will be an image spread. This requirement is challenged by the star-trail curvature mentioned above and the sidereal rate varying with declination: there appear errors dependent on the latitude and increasing proportionally to the square of the angular field of view. Since the magnitude of the effect is typically 1-2 arcsec, it is important to use 4-optical-element correctors at the prime focus [40].

2.6 LMT technical issues.

As already mentioned, the layout of this telescope is very simple, but this doesn't mean that the telescope is free from technical difficulties, some of them already solved and other in search of a solution.

Besides the technical problem to give a uniform rotation to the mirror, today solved with a modern drive system, a real difficulty is the formation of surface waves, which degrades the image quality. Such waves can result from two causes: vibration transmission from the floor to the mirror; inaccuracy in leveling the mercury (avoided with a better alignment between the mirror rotation axis and the gravitational field) and an unstable rotation speed. Some optical tests carried out at Laval University on the quality of a mercury surface [3] showed that the total amplitude of ripples is between $\lambda/10$ and $\lambda/15$ at 5000 Å.

Vibrations can be caused by wind as well: the mercury surface doesn't tolerate turbulent local air velocities, stronger than 12 m/s. The telescope enclosure must therefore provide wind protection.

2.7 Data analysis.

2.7.1 Object detection and photometry.

Before data analysis, it is necessary to subtract the *dark current* and the sky, and to correct for response variations (flat field).

The *dark current* is corrected using data accumulated in TDI mode with the CCD covered; the flat field is obtained from observations on nights with moon-brightened cloudy skies. Cosmic rays and stellar images are removed by median filtering.

Once these corrections are done, consecutive CCD rows are put together in blocks of 2048 overlapping lines: the sky subtraction is then obtained by subtracting the mode (the most common value inside the distribution) of each line and row. After this procedure, since the good uniformity of CCD images, systematic background variations are lower than 0.02%.

The object detection and the photometry are done on individual data blocks: in order to diminish the noise, the object identification is conducted on a smoothed image copy, obtained using a 5×5 pixel boxcar filter which provides a five-fold reduction in background noise. In each block, the background mean standard deviation is determined eliminating iteratively the stellar images row by row: then, all the pixels with a value exceeding the mean by 2.5 standard deviation are marked, areas of contiguous pixels are

identified and the outline of each of them is considered the object isophote.

For sources inside the image, the first three moments about the intensity distribution are determined within the isophote considered:

- the zero-order moment, the isophotal flux;
- the first-order moment, from which the image coordinates can be obtained;
- the second-order moment, from which the inertia tensor is determined and whose eigenvalues give the major axis, the minor axis and the position angle of the intensity distribution.

All the measurements are done on the un-smoothed image and inside the area of the object isophote determined from the smoothed image.

Since raw isophotal magnitudes are not realistic for dim objects (an increasing fraction of light falls outside the isophote and adding flux from outside the same isophote increases the measurement noise), a correction is applied to these magnitudes depending on the flux and on the mean intensity inside the isophote registered. This correction was calculated assuming the relationship between the intensity and the flux is the same as for a Gaussian intensity profile, which is a good approximation to seeing-altered profiles of the faintest galaxies in the image.

In order to identify and separate objects whose images overlap, the detection algorithm is repeated with increasing detection thresholds of surface brightness: at each step, the area inside the isophotal outline of an object previously detected is examined. The isophote level is increased until either the object no longer reaches the threshold, or it breaks into two parts. In the latter case, the total flux and the isophotal flux of the "initial" source is divided between the two parts, proportionally to their isophotal fluxes.

For data obtained with this telescope, the fraction of objects which suffer blending is around 1%.

The photometry program produces a list of all the sources recorded in one night of observation: instrumental magnitudes, positions, errors, image parameters and the full-width at half-maximum intensity (FWHM).

Instrumental coordinates were obtained by applying corrections for aberration and nutation of the coordinates of the image centroids, and then referring these value to the standard epoch (J2000).

2.7.2 Astrometric and photometric calibration.

For the astrometric calibration process the USNO A1 stellar catalog, produced by the US Naval Observatory for the Precise Measurement Machine Project [55], was used. The first stage is to find a number of astrometric reference stars from the astrometry file and then to fit the astrometric data using the nearest calibration star.

Astrometric fitting equations in right ascension and declination are based on 7 parameters including offsets and linear and quadratic scale factors for both the coordinates. The resulting coordinates have typical errors around 0.3 arcsec, both in right ascension and declination.

The photometric calibration was conducted using spectro-photometric stars inside the survey field. These were calibrated by observations conducted at the *Kitt Peak National Observatory*: 22 stars were chosen to cross the telescope field every 30 minutes, producing a calibration accurate to within $\sim 5\%$ at every wavelength [41].

For each band, the product between the filter transmission curve and the

specific flux for the standard star is integrated to give the magnitude zero point in that band.

To account for possible sky transparency variations during the observation, a second order polynomial is fit to the magnitude zero points from the standard stars and applied to the instrumental magnitudes to give the calibrated values for all the objects.

AB magnitudes are used, defined in this way:

$$m_\nu = -56.10 - 2.5 \log(f_\nu) \quad (2.2)$$

where f_ν is the average specific flux for the filter passband in $W m^{-2} Hz^{-1}$ [39].

2.7.3 The object catalog.

In order to obtain the final catalogue of objects, it is necessary to merge the photometry files of all the nights for which the same filter was used.

They were identified as objects all those detected on more than one night (in order to reject cosmic rays and spurious detection of noise), having a difference of magnitude smaller than 1 and the same position to within an error smaller than 3.5 arcsec.

For each night the magnitude error is estimated from the object flux, the isophotal area and the background variance. The average magnitude is determined weighing the magnitude for each night by the reciprocal variances.

The same weights are then used when the average values for other photometric and astrometric parameters are calculated.

The final photometric errors are calculated easily: for each source, the

variance of the mean is found from the magnitude variances and this allowed the estimation of the random noise.

The total error, the sum of random and systematic one, is estimated by calculating directly the variance in the magnitude obtained on different nights. The highest of this estimation is kept for final record.

The entire procedure gives a single photometric file for each band and then, in order to obtain the SED (Spectral Energy Distribution), the final files correspondent to all the bands must be grouped.

2.8 Characteristics of the survey.

The survey was conducted in different narrow bands covering 20.13° square of sky, centered at the declination of $+33^\circ$ and at right ascension from 10hr to 18hr.

The observation in a band is done by inserting a glass filter between the corrector lenses and the CCD window. A filter is positioned at the beginning of the observation and used for all the night. This survey is based on observations taken in 1996, 1997 and 1999 using 35 narrow band-filters covering 454 - 993 nm, and 4 broad band-filters: $B(440\text{ nm})$, $V(550\text{ nm})$, $R(700\text{ nm})$, $I(900\text{ nm})$. These filters, being broader than the narrow ones, reach a fainter limiting magnitude and they make easier the comparison with other broad-band photometries. Table 2.1 shows the characteristics for narrow filters.

Fig 2.3 displays their transmission curves. The fact blue filters have lower transmission curves (a lower percentage of photons is received at wave-

ID	λ_0^a	$\Delta\lambda^b$	$\log(\nu)^c$	$\Delta\log(\nu)^d$	t_0^e	W^f
948	947.7	39.08	14.5003	0.019	0.933	36.43
925	924.5	40.04	14.5111	0.019	0.928	36.96
906	906.3	35.32	14.5198	0.018	0.900	31.71
883	883.1	41.28	14.5311	0.021	0.924	38.10
868	867.9	35.10	14.5388	0.018	0.952	33.38
844	843.8	35.58	14.5509	0.019	0.932	33.09
825	824.8	33.67	14.5608	0.018	0.950	31.96
806	805.9	34.62	14.5709	0.019	0.936	32.27
788	787.5	33.31	14.5809	0.019	0.927	30.85
770	769.6	31.86	14.5910	0.018	0.937	29.79
752	752.4	33.25	14.6008	0.019	0.955	31.72
735	734.7	32.17	14.6111	0.019	0.940	30.17
719	718.7	30.54	14.6208	0.019	0.954	29.13
704	704.4	29.88	14.6293	0.019	0.930	27.78
688	688.0	29.20	14.6397	0.019	0.936	27.30
671	671.3	29.08	14.6503	0.019	0.933	27.10
655	654.6	27.99	14.6612	0.019	0.930	26.03
641	641.1	23.98	14.6705	0.016	0.919	21.99
629	628.7	26.39	14.6789	0.018	0.952	25.10
614	613.7	23.62	14.6893	0.018	0.910	21.45
598	597.6	24.31	14.7010	0.018	0.717	17.41
586	585.6	23.10	14.7099	0.018	0.720	16.63
571	571.1	21.71	14.7207	0.017	0.750	16.26

Table 2.1: Continue.

ID	λ_0^a	$\Delta\lambda^b$	$\log(\nu)^c$	$\Delta\log(\nu)^d$	t_0^e	W^f
557	557.0	21.35	14.7314	0.017	0.707	15.05
545	545.1	21.00	14.7409	0.017	0.726	15.22
533	532.7	22.76	14.7505	0.019	0.730	16.59
519	519.0	22.72	14.7609	0.022	0.679	15.38
510	510.2	22.36	14.7698	0.019	0.689	15.39
498	498.1	21.91	14.7798	0.019	0.670	14.66
486	486.0	20.22	14.7904	0.019	0.752	15.18
476	475.6	19.30	14.7998	0.018	0.690	13.31
466	465.9	18.48	14.8090	0.018	0.673	12.42
455	454.5	17.67	14.8196	0.018	0.632	11.17

Table 2.1: Filter specifications. (a) mean wavelength (nm), from transmission curve; (b) bandwidth (nm): equivalent width/central transmission; (c) log of central frequency (Hz): c/mean wavelength; (d) log frequency bandwidth: $0.434 \times \text{bandwidth}/\text{mean wavelength}$; (e) central transmission; (f) equivalent width (nm): integral of transmission curve.

lengths shorter than 600 nm) and the exposure time is the same for each filter, influence signal-to-noise ratios in such a way that, for blue bands, the signal-to-noise ratios result lower than those of red filters.

Each filter was used on more than one night in order to recognize cosmic rays, to create an independent estimate of the photometric accuracy and to improve the object signal-to-noise ratio. The sequence of the filter observations depended on lunar phase. In order to minimize the effect of the moon

on the sky brightness, the red and infrared bands were used when the moon was bright and the blue filter were used when the moon was new.

2.8.1 Photometric selection criteria.

The recorded objects are limited by the surface brightness, by the apparent magnitude and by the angular separation.

In order to distinguish an object, the surface brightness must exceed the detection threshold for a minimum number of connected pixels corresponding to a minimum area of $A_m = 1.788 \text{ arcsec}^2$. Then, if f and \bar{i} are respectively the flux and the median intensity inside the isophote, the first selection criterion is

$$f/\bar{i} \geq A_m. \quad (2.3)$$

To record the object

$$\bar{i} > i_m \quad (2.4)$$

where i_m is the detection intensity threshold: to maximize the number of detected objects, i_m is set to the lowest possible level allowed by the background noise, which is generally dominated by the sky light and varies according to the lunar phase. The formula 2.4 represents the second criterion.

The third criterion requires a minimum signal-to-noise ratio ζ . The noise is due to both the image's Poissonian noise and the background noise, then

$$f > \zeta^2(g + \sigma^2/\bar{i}) \quad (2.5)$$

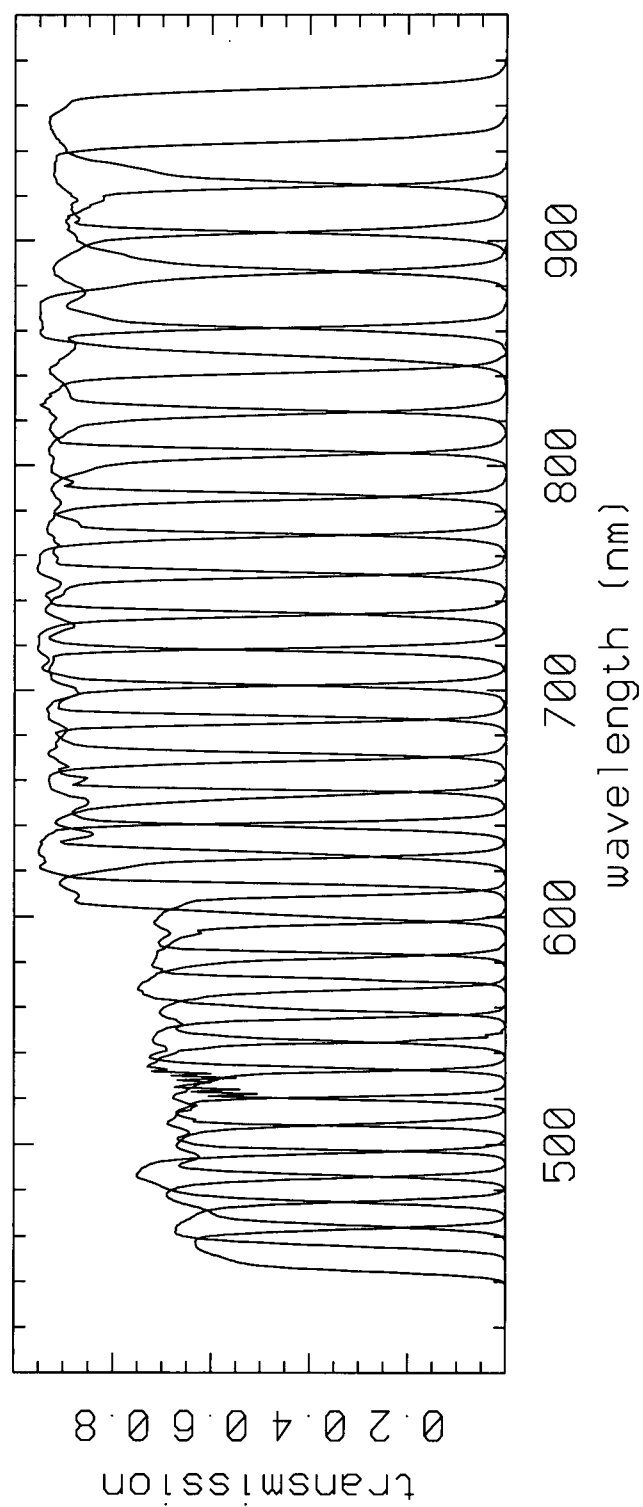


Figure 2.3: Filter transmission curves.

where σ is the background noise variation and g is the system gain (signal produced by a single photo-electron).

The limiting magnitude for each block of survey data can be estimated from the surface brightness, by the minimum area required to find the object and by the seeing FWHM. This function can change on short time scales since it depends on atmospheric conditions.

CHAPTER 3

QUASI STELLAR OBJECTS.

3.1 QSO's fundamental characteristics.

Schmidt described the optical properties of quasars in 1964 in the following way [13]:

- starlike objects identified with radio sources;
- variable light;
- large UV lines in spectra;
- broad emission lines in spectra;
- large redshift of the spectrum.

Since then, many surveys have been completed at different frequencies and much has been learnt about quasars.

Now we know that even though quasars were first found as radio sources, only 10% of those optically selected are radio loud, with a power higher than $10^{26} \text{ W Hz}^{-1}$. Their radio structure is not so different from that of giant ellipticals. Their X emission is very strong as well, $L_X \sim 10^{21} - 10^{23} \text{ W Hz}^{-1}$ [22].

Since the liquid mirror telescope works in the optical range, it is useful to describe quasar optical properties in detail.

In general the optical luminosity is extremely high: typical values are around $L_{opt} \sim 10^{22} - 10^{24} \text{ watt Hz}^{-1}$ which corresponds to an absolute

magnitude $M_{opt} \sim -11$ - -28 (to make a comparison, the absolute magnitude of giant ellipticals is -22 - -23).

The optical variability, from weeks to a few months, is of few tenths of magnitude. From that, it is possible to calculate the linear scale implied by the duration of this variation through this formula:

$$D \leq c\tau_0 = c\tau/(1+z) \quad (3.1)$$

where τ_0 and τ are respectively the time variation in the quasar's and in the observer's frame. It is found that all the energy comes from a region smaller than $10^{16} - 10^{17}$ cm in diameter; this situation can be explained only by means of relativistic effects.

The general trend for a quasar spectrum beyond the optical range is shown in Fig. 3.1. It is characterized by a continuum plus strong absorption and emission lines. The continuum is well approximated by a power law

$$f_\nu \propto \nu^\alpha \quad (3.2)$$

where f_ν is the monochromatic flux at frequency ν and α is the spectral index: different values of this parameter were found from surveys, but the most common range is $[-2, 0.8]$ as we describe in §4. In the optical region the continuum tends to flatten and it shows a more or less pronounced "UV Bump" or "Big Blue Bump", a real deviation from the power law. It has been proposed by Shields [69], that the blue bump might be due to thermal emission from the surface of an optically thick but geometrically thin accretion disc which surrounds the central source. The emitted spectrum is then the superposition of black bodies of temperatures decreasing from the inner

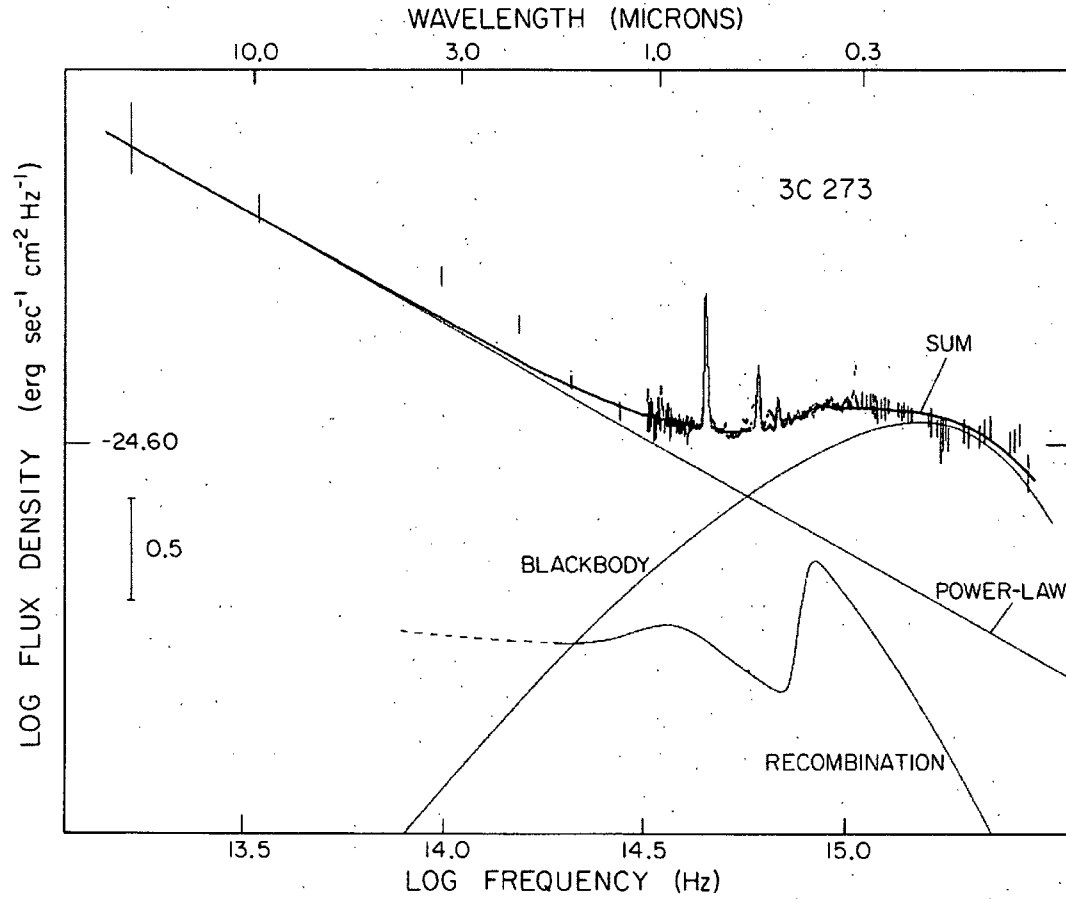


Figure 3.1: General layout for a quasar spectrum.

radius to the outer radius of the disc. Many features of this emission could be explained by accretion disc models which are based on possible matter accretion with some angular momentum, provided that an adequate source of viscosity is available to transport this angular momentum towards the outer regions of the nucleus [69].

Table 3.1 lists the most important quasar emission lines in the UV and

optical range.

These lines are so important to identify quasars that if a few of them are missed, since the method is based on the comparison between the observed SED and models, it is likely to misclassify objects.

Many lines which fall in the UV range are detectable from optical instruments only at high redshift, according to the relation

$$\lambda_{obs} = \lambda_{em}(1 + z) \quad (3.3)$$

where λ_{obs} is the observation wavelength, λ_{em} is the rest frame wavelength and z is the redshift.

Besides numerous and strong emission lines, absorption features are also observed. Since they are caused by material between the observer and the luminous source along the line of sight, the absorbing material has a redshift smaller than the quasar. For the same object, three categories of absorption lines can be found:

- *metallic systems*: groups of two or three lines at wavelengths very close to each other and with the same redshift. The most common are CIV λ 1548/1551 Å and Mg II λ 2796/2803 Å but also C, N, O, Si, S, Al and Zn systems can be present.

- the *L α forest*: at emission wavelengths lower than 1260 Å there are many weak and narrow absorption lines which have the dramatic effect of strongly reducing the quasar emission intensity. In this case, each line has its own redshift.

- *broad absorption lines*: very large features which begin from the blue part of strong emission lines and extend for many thousands of km sec⁻¹.

line	Å
Ly β	1025.7
O VI	1035
Ly α	1215.7
N V	1241.5
O I + [S II]	1305
Si IV + O IV	1400.0
C IV	1549
He II	1640
Al III	1859
C III	1909
Mg II	2800
Ne V	3426
[O II]	3728
Ne III	3869
H δ	4101.7
H γ	4340.5
[O III]	4363
He II	4686.5
H β	4861
He I	5875.6
H α	6563

Table 3.1: Inventory of emission lines [23].

Their connection to strong emission lines is perhaps due to fact they originate close to the quasar.

3.2 QSO structure.

Quasars are the most powerful sources among AGNs, a heterogeneous class of objects characterized by a great manifestation of energy which cannot be explained by ordinary stellar processes.

There is a growing convergence of opinions that AGNs are in reality the same type of object: it might be possible to develop a model common to most AGNs which could account for factors such as variability, evolution and orientation effects.

The variability is a significant problem: since many objects show a variable emission over few years, it is easy to put them into the wrong category. Fairall 9, a quasar with a Sy1 spectrum, became a Sy2 galaxy decreasing its magnitude by a factor of 3 in 5 years, or a BL Lac, PKS0521-36, became a Sy1 galaxy in less than 6 years.

The evolution factor could be important if the variability time was very long and systematic: for example, since quasars radio loud show an optical/UV/X luminosity which decreases slowly and systematically to the point to be negligible, we could think of this transformation from quasars to radio-galaxies as a sort of evolution.

Recently, attention has focussed on models that explain AGNs' observational characteristics as due to different orientations with which objects are seen from Earth, with different accretion rates and masses of the cen-

tral black hole and with something which prevents the radiation from being isotropic. According to the most recent model, a funnel-shaped thin shell outflow creates all these features (fig. 3.3).

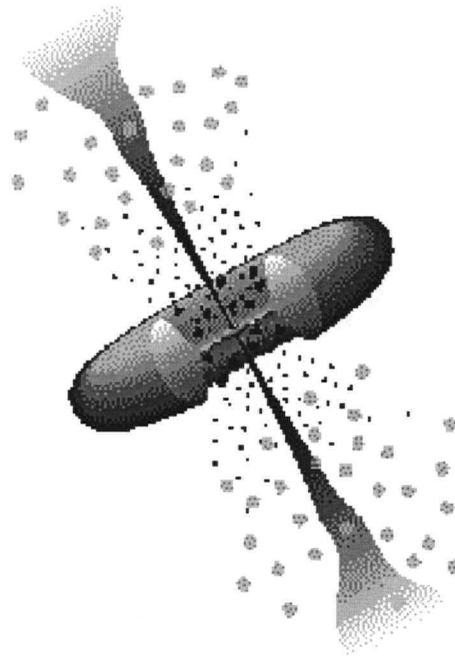


Figure 3.2: Structure of AGN's inner region ([http:// nedwww.ipac.caltech.edu/level5/Urryl/UrryPl.html](http://nedwww.ipac.caltech.edu/level5/Urryl/UrryPl.html)).

In more detail, a torus of opaque material such as dust, with a radius of few parsecs, surrounds a nucleus which is likely a 10^{17} cm black hole, from which a thermal and not-thermal continuum is emitted.

Inside the torus there is a Broad Line Region (BLR), dense and highly mobile clouds, and outside the torus there is a Narrow Line Region (NLR), less dense and slow clouds. Sometimes a relativistic jet can emerge from the nucleus and relativistic effects will be seen if the line of sight is close to the

jet direction. Looking at directly into the jet, we should see OVV (Optical Violent Variable, characterized by an exceptional optical variability) and BL Lac objects (with a great activity and variability from the radio to the X-part of the spectrum). If the BLR material is absent or the boosting doppler in the optical continuum is very strong, the BLRs shouldn't be visible. At a larger angle, radio quasars should appear. When the central source is obscured but the BLRs are partially covered, broad line radio galaxies (BLRG) could be observed. Increasing the angle, with the central source and the BLRs now obscured, only the narrow lines are visible: this is a NLRG, narrow line radio galaxy. When the radio jet is very weak or absent, it is likely to have a radio quiet quasar or Seyfert 1 (mainly associated to spiral galaxies having strong emission continuum with broad and forbidden narrow emission lines) when the central source is not covered, or a Seyfert 2 (with broad and narrow emission lines and a non-negligible X-ray emission) when the nucleus is obscured. Even without a collimated jet, one can expect a strong wind from the nucleus, able to blow away part of the torus or a BLR cloud: in this case a Broad Absorption Line quasar (BAL) could be the end result.

CHAPTER 4

THE UNMS QUASAR SURVEY.

4.1 The UNMS1 catalog.

The UNMS1 catalog [Hickson, P., priv. comm.] includes more than 2000000 objects: Table 4.1 displays parameters provided for each object, besides their spectral energy distribution (SED) in as many as 35 narrow bands and 4 broad bands. Parameters “nband” and “pa” represent respectively the number of bands in which an object was observed and the angle between the image semi-major axis and the line North-South direction, measured from East to West starting from North. Details about filters were given in §2.

As explained in §4.4.3, only objects with reliable flux measurements in 30 or more filters were used in this study: the selected sample contains 39040 objects.

Recently Remi Cabanac (ESO), using Principal Component Analysis on bright stars, discovered that UNMS1 SEDs show a systematic deviation from spectra published by Pickles [56]. The UNMS1 SEDs tend to be brighter at long and short wavelengths. This could result from an error in the absolute calibration derived from KPNO observations. To make the UNMS1 catalog more consistent with that of Pickles, the original fluxes $F_{orig}(filter_i)$ were corrected according to the relation

parameter	abbr.	units
Right Ascension	ra	hh:mm:ss
Declination	dec	deg:arcmin:arcsec
band number	nband	
semimajor axis	a	arcsec
semiminor axis	b	arcsec
position angle	pa	grad
broad bands	B-V-R-I	mag
narrow bands	14.48 - 14.82	mag

Table 4.1: Parameters in the UNMS1 catalog.

$$F_{corr}(filter_i) = F_{orig}(filter_i)/C(filter_i) \quad (4.1)$$

where $F_{corr}(filter_i)$ is the corrected flux in the “ i^{th} ” filter and $C(filter_i)$ is the correction correspondent to this filter. This formula can be directly applied to narrow bands since the largest bandwidth is around 40 Å; for broad bands the most accurate way to proceed is to convolve the transmission curves with the best fit curve of the discrete set of corrections, according to the formula

$$C(filter_i) = \frac{\sum_k C_{\lambda_k} W_{\lambda_k}^i}{\sum_k W_{\lambda_k}^i} \quad (4.2)$$

where C_{λ_k} is the value from the correction curve and $W_{\lambda_k}^i$ is the transmission curve value for the “ i^{th} ” filter at wavelength λ_k . Table 4.2 shows the flux corrections provided by Remi Cabanac.

Λ	correction	Λ	correction
4541.0	1.180418	6873.0	0.925380
4865.0	1.059962	7033.0	0.923201
4979.0	0.992161	7197.0	0.915377
5095.0	1.055990	7364.0	0.908164
5213.0	1.031924	7536.0	0.948763
5335.0	0.967368	7711.0	0.941986
5459.0	0.990099	7891.0	0.950050
5586.0	0.997617	8075.0	1.010598
5716.0	0.997977	8263.0	1.015200
5850.0	0.958713	8455.0	1.033491
5986.0	0.996552	8652.0	1.087448
6125.0	0.937052	8854.0	1.064739
6268.0	0.964520	9060.0	1.109830
6414.0	0.903055	9271.0	1.204436
6563.0	0.893435	9487.0	1.224466

Table 4.2: Flux corrections by Remi Cabanac [priv. comm.].

The best fitting curve, found from a χ^2 minimization procedure, is

$$C_\lambda = 2.893959 - 5.80649710^{-4}\lambda + 4.26502710^{-8}\lambda^2 \quad (4.3)$$

and it is graphically represented by the line in Fig. 4.2 with the discrete set of corrections.

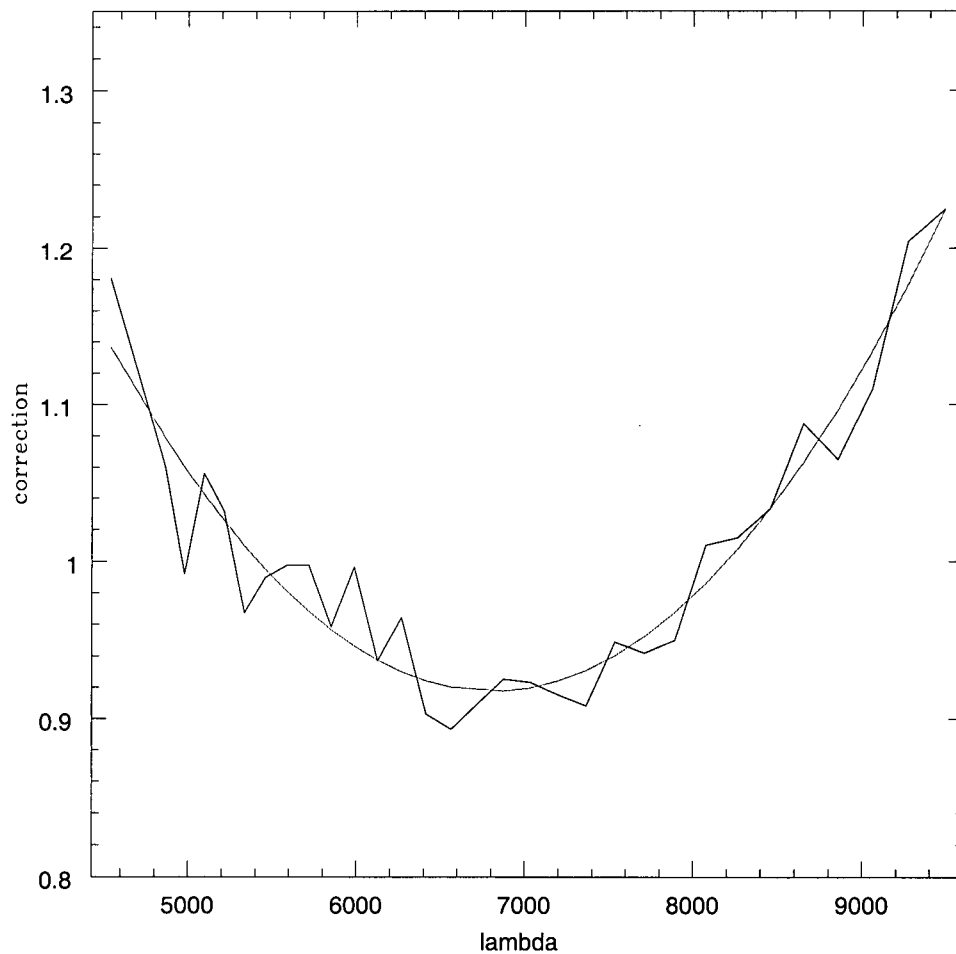


Figure 4.1: Corrections with the best fit curve.

4.2 Method.

The method used to separate quasars from stars and galaxies is based on the χ^2 minimization procedure combined with a Bayesian approach.

According to the Bayesian theory, given two models and a data set, it

is often more useful to consider the ratio of model probabilities than the probabilities directly [30].

The so-called *odds ratio* in favor of the model M_i over the model M_j is defined as

$$O_{ij} = \frac{p(M_i|D, I)}{p(M_j|D, I)} \quad (4.4)$$

where $p(M_i|D, I)$ is the probability of “ i^{th} ” model M_i given the data D and the prior information I . According to Bayes’ theorem, the posterior probability of the model M_i based on data and the prior information is

$$p(M_i|D, I) = \frac{p(M_i|I)p(D|M_i, I)}{p(D|I)} \quad (4.5)$$

where $p(M_i|I)$ is the probability of the model M_i given the prior information I , $p(D|M_i, I)$ is the global likelihood for the model M_i (data influence the choice of the model) and $p(D|I)$ is the probability of data given the prior information (this parameter is independent of the model).

Substituting these terms in (4.7), the odds ratio becomes:

$$O_{ij} = \frac{p(M_i|I)p(D|M_i, I)}{p(M_j|I)p(D|M_j, I)} = \frac{p(M_i|I)}{p(M_j|I)} B_{ij} \quad (4.6)$$

where B_{ij} is the *Bayesian factor*.

If $p(\theta|M_i, I)$ is the prior probability of each sub-model of that specific category M_i , characterized by the parameter θ (it is reasonable to take this probability equal to $1/N_i$, where N_i is the total number of sub-models of that category) and $p(D|\theta, M_i, I)$ is the posterior probability of the template (the likelihood function of that template), the global likelihood of the model M_i is defined as

$$\begin{aligned}
p(D|M_i, I) &= \int p(\theta|M_i, I)p(D|\theta, M_i, I) d\theta \\
&= \frac{1}{N_i} \int p(D|\theta, M_i, I) d\theta \\
&= \frac{1}{N_i} \sum_{\theta_i=1}^{N_i} p(D|\theta_i, M_i, I)
\end{aligned} \tag{4.7}$$

For one template of the category M_i , the maximum likelihood for “N” detected bands is just the product of the individual probability functions for the observed fluxes and the model fluxes in the same filter: assuming a Gaussian distribution, the maximum likelihood is then [4]

$$p(D|\theta_i, M_i, I) = \prod_{n=1}^N \left[\frac{1}{\sigma_n \sqrt{2\pi}} \right] \exp \left[-\frac{1}{2} \sum_{n=1}^N \left[\frac{F_n - AF_n^T}{\sigma_n} \right]^2 \right] \tag{4.8}$$

where F_n and σ_n are the observed flux and its error in the “ n^{th} ” filter, F_n^t is the template flux in the “ n^{th} ” filter and A is the normalization constant.

The χ^2 parameter is defined as

$$\chi^2 = \sum_{n=1}^N \left[\frac{F_n - AF_n^T}{\sigma_n} \right]^2 \tag{4.9}$$

therefore

$$p(D|\theta_i, M_i, I) = \prod_{n=1}^N \left[\frac{1}{\sigma_n \sqrt{2\pi}} \right] [e^{-\frac{1}{2}\chi^2}] \tag{4.10}$$

Maximizing the likelihood function involves the minimization of the exponent: that involves the χ^2 minimization through the right choice of the normalization constant, which can be found from the condition

$$\frac{\delta \chi^2}{\delta A} = 0. \tag{4.11}$$

The final formula for the odds ratio is

$$O_{ij} = \frac{p(M_i|I)}{p(M_j|I)} \frac{N_j}{N_i} \frac{[e^{-\frac{1}{2}x_i^2}]}{[e^{-\frac{1}{2}x_j^2}]}. \quad (4.12)$$

	stars	galaxies	quasars
B	$10^{(0.162B[i]-0.516)}$	$10^{(0.29*B[i]-2.61)}$	a: $10^{(0.86*B[i]-15.80)}$ b: $-10.95 + 15.61 \cdot 10^{0.28*(B[i]-19.15)}$
V	$10^{(0.15*V[i]+0.05)}$	same as for B filter	same as for B filter
R	$10^{(0.41*R[i]-5.52)}$	$10^{(0.11*R[i]+0.15)}$	same as for B filter
I	$10^{(0.38*I[i]-4.42)}$	$10^{(0.1*I[i]+0.5)}$	same as for the B filter

Table 4.3: Surface densities for stars, galaxies and quasars in the broad bands: the units are num/deg² for the B and I filters, and num/deg² 0.5 mag in the R and V bands. The “a” case is for $B < 19.5$ and the “b” is for $B > 19.5$.

The quantity $p(M_i|I)$ is related to the surface density of quasars, stars and galaxies given the magnitude in a filter. Table 4.3 shows these quantities, extrapolated from other surveys, for the broad bands B , V , R , I . All the consulted quasar surveys report surface densities in the B band: this situation, which explains why V , R , I bands have the same surface density as the B , is due to the fact that these surveys studied quasars at small and medium redshift (0.3 - 3) for which important spectral features, such as the $Ly\alpha$, are still in the B . For high redshift quasars ($z > 3$), the observed flux in the B band is reduced dramatically by the presence of the increasingly prevalent $Ly\alpha$ forest lines and of the higher column density metal-line absorption

systems. For surveys of high redshift quasars, working in the R band or at longer wavelenths is a fundamental prerequisite to select this category of sources: these kind of studies have just started. The unaccuracy to have the same surface density for different broad bands doesn't influence the object classification: the amount of quasars is a really small percentage of that of stars and galaxies in every bands.

The identification is done through a code which, for each object, calculates the odds ratio for every pair of categories (star-galaxy, star-quasar, galaxy-star, galaxy-quasar, quasar-star and quasar-galaxy, six combinations in total), and chooses the highest one: for example, if the highest odds ratio is $O_{s,q}$ between a star and a quasar template, the object in question is identified as a star.

4.3 Templates.

4.3.1 Stellar templates.

Stellar templates were taken from Pickles' database [56]. The stellar spectral library includes 131 flux-calibrated spectra encompassing all normal spectral types and luminosity classes at solar abundances, metal-weak and metal-rich F-K dwarfs and G-K giant components. The library has complete spectral coverage from 1150-10620Å, in steps of 5Å, up to 25000Å for about half of them (mainly later stellar types). Monochromatic fluxes F_λ are tabulated and normalized to unity at 5556 Å.

Table 4.4 shows how these templates are organized inside the library: the

first column gives the library number, the second column the stellar type, and the third column the luminosity class. The first group includes 5 metal-weak and 5 metal-rich G-K V spectra, the third group includes 7 metal-weak and 7 metal-rich G-K III spectra.

library number	stellar type	luminosity class
1-45	O5-M6	V
46-59	B2-K3	IV
60-105	O8-M10	III
106-113	B2-M3	II
114-131	B0-M2	I

Table 4.4: Parameters in Pickles' stellar library.

In order to be compared to the observed spectral energy distributions, these templates must first be convolved with the transmission curves of those filters used in this survey. For the " T^{th} " template, the monochromatic flux integrated over the " i^{th} " filter, F_i^T , is given by

$$F_i^T = \frac{\sum_{k=1}^{39} F_{\lambda_k}^T W_{\lambda_k}^i Q_{\lambda_k}}{\sum_{k=1}^{39} W_{\lambda_k}^i Q_{\lambda_k}} \quad (4.13)$$

where $F_{\lambda_k}^T$ is the template's flux at wavelength λ_k , $W_{\lambda_k}^i$ is the " i^{th} " filter transmission value at wavelength λ_k and Q_{λ_k} is the system response.

Since UNMS1 spectra are given in frequency, F_ν versus ν , monochromatic fluxes in wavelength are converted to fluxes in frequency according to the formula

$$F_\nu = \frac{c}{\lambda^2} F_\lambda \quad (4.14)$$

The system response Q_{λ_k} is approximated by the CCD Quantum Efficiency (QE). CCDs used in this survey don't show any response for wavelengths higher than $1 \mu\text{m}$. Therefore, the sum in (4.4) is carried only as far as $\lambda = 1000 \text{ nm}$: this involves those filters whose transmission curves extend further than this threshold, the broad-band I and the narrow bands $\log(\nu) = 14.48$ and $\log(\nu) = 14.49$ (these narrow filters were used in 1999 only). The procedure was applied to galaxy and quasar templates as well.

4.3.2 Galaxy templates.

Most of the galaxy SEDs were taken from Kinney & Calzetti's library [44] and integrated with few others from Rocca-Volmerange's database [59] in order to have a complete set of templates.

The first group of spectra are given as F_λ versus λ , with the flux in $\text{erg cm}^{-2} \text{s}^{-1} \text{\AA}^{-1}$ and steps of 1.5\AA . The galactic types used are elliptical, bulge, S0, Sa, Sb and Starburst galaxies from 1200\AA to 8000\AA , in some cases up to 10000\AA . Table 4.5 summarizes the template types. All these spectra, normalized at 4000\AA , are shown in Fig. 4.2.

The second group of templates includes Sc and UV-hot E/S0 models, 12.08 Gyr old, extended from far-UV (1220\AA) to $1 \mu\text{m}$ with a spectral resolution of 10\AA .

All the templates were convolved with filter transmission curves in the same way as the stellar templates. Since models provided are built in the rest frame, they were redshifted from $z=0.00$ to $z=1.20$, with step $\delta z=0.01$;

library name	galactic type	colour excess
SB1	starburst galaxy	$E(B-V) < 0.10$
SB2	starburst galaxy	$0.11 < E(B-V) < 0.21$
SB3	starburst galaxy	$0.25 < E(B-V) < 0.35$
SB4	starburst galaxy	$0.39 < E(B-V) < 0.50$
SB5	starburst galaxy	$0.51 < E(B-V) < 0.60$
SB6	starburst galaxy	$0.61 < E(B-V) < 0.70$
S0	S0 galaxy	
Sa	Sa galaxy	
Sb	Sb galaxy	
bulge	bulges templ.	
elliptical	elliptical templ.	

Table 4.5: Spectral templates from Kinney & Calzetti galaxies' library.

in this way, 1573 templates were obtained.

4.3.3 Quasar templates.

The rest-frame template of quasars is the result of merging two templates taken from different authors, in order to cover the largest possible wavelength range (330-8550 Å).

The first SED model comes from Zheng et al. [78] and was constructed using 284 HST FOS spectra of 101 quasars with redshifts $z \geq 0.33$. The uncalibrated spectrum is given in Fig. 4.3 and it covers wavelengths between 350 and 3000 Å in the rest frame.

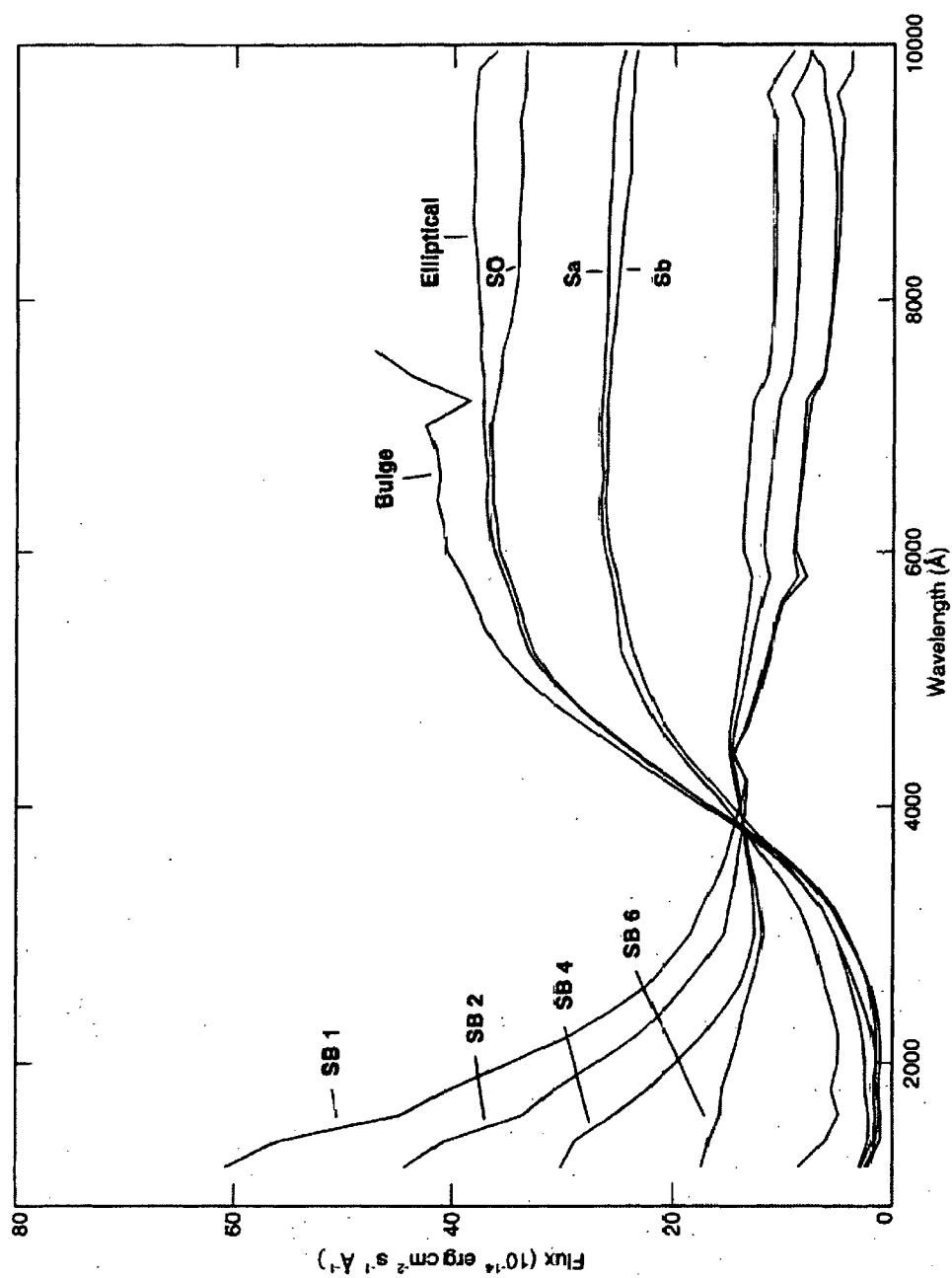


Figure 4.2: Kinney-Calzetti's galaxy templates normalized at 4000 Å.

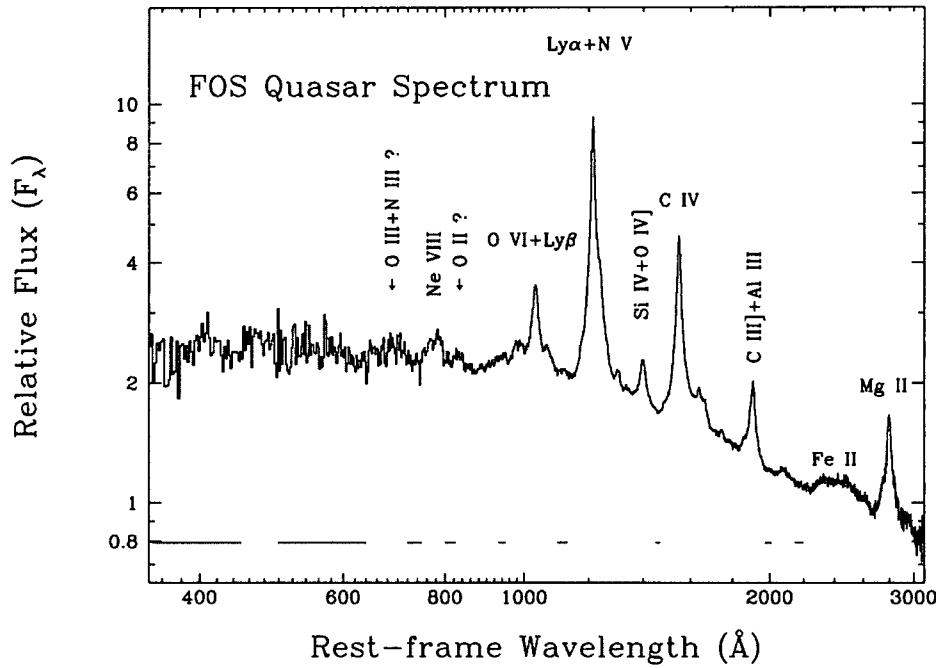


Figure 4.3: Composite spectrum of 101 quasars, binned to 2 Å.

It is clear there is a significant steepening of the continuum slope around 1050 Å. Table 4.6 shows continuum fit parameters using radio-loud quasars, radio-quiet quasars and both types together: power law indexes $\alpha_\nu = -1.96$ for the range 350-1050 Å and $\alpha_\nu = -0.99$ for the range 1050-2200 Å characterize the original template.

The second model, in Fig 4.4, was taken from Vanden Berk et al. [74]. The composite spectrum, with resolution of 1 Å, is the result of a homogeneous data set based on more than 2200 spectra from the Sloan Digital Sky Survey. The median composite template covers a range from 800 to 8555 Å. A double power law with $\alpha_\nu = -0.46$ for $\lambda \leq 4700$ and $\alpha_\nu = -1.58$ for $\lambda \geq 4700$ Å is the

Sample	All Quasars	Radio-loud	Radio-quiet
Number of objects	101	60	41
Mean redshift	0.93	0.87	0.95
Wavelength range (Å):			
1050-2200	-0.99 ± 0.01	-1.02 ± 0.01	-0.86 ± 0.01
600-1050	-2.02 ± 0.05	-2.45 ± 0.05	-1.83 ± 0.03
350-1050	-1.96 ± 0.02	-2.16 ± 0.03	-1.77 ± 0.03

Table 4.6: Fitted power-law index.

best fit. The spectral region blueward of the $\text{Ly}\alpha$ emission line was ignored when calculating the flux density scaling, since the $\text{Ly}\alpha$ forest flux density varies greatly from spectrum to spectrum. This is another reason which explains why this region was then replaced by the first template.

The first step was to integrate these two models. This was done making them completely flat (spectral features were reproduced proportionally to their reciprocal intensities on a null-slope spectral continuum), calculating the normalization constant in the wavelength range they overlap and applying this constant to obtain a unique template. Fig. 4.5 and Fig. 4.6 show this unique “flat” model respectively for the range 300-3400 Å and the range 3400-8550 Å. Many important features such as the $\text{Ly}\alpha$, $\text{Ly}\beta$, $\text{H}\alpha$ and OIII emission lines are well pronounced.

The second step was to build different types of templates introducing various slopes for the spectral continuum. The idea was to look for the largest possible range of the spectral index α_ν cited in papers, and then to divide this range into equal intervals. For the UV part of the template to be

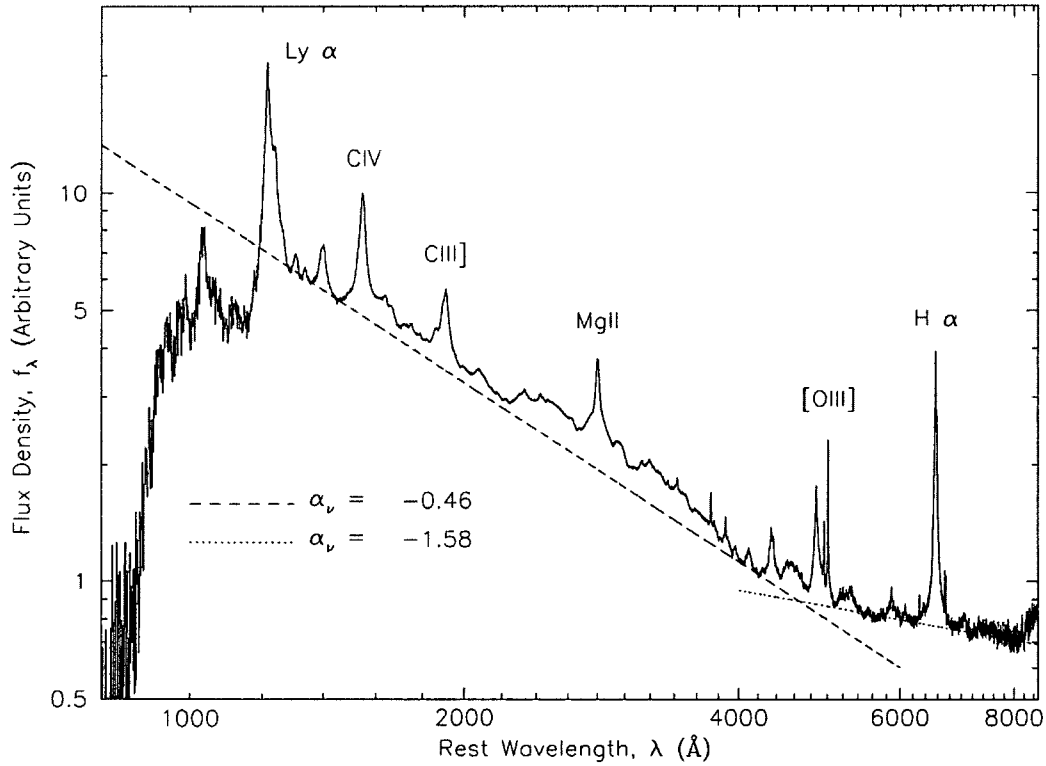


Figure 4.4: Composite spectrum: power law fits to the estimated flux are shown.

constructed, only one value of slope was used, $\alpha_\nu = -1.96$, which is the average between the lowest UV slope in literature, -2.16 from Zheng et. al [78], and the highest value, $\alpha_\nu = -1.76$ found from Hatziminaoglou et. al [33]. The same idea was used for the optical-near infrared (Opt-IR) range: the lowest slope value is -2.5 from Richstone & Schmidt [58] and the highest value is 1 from Hatziminaoglou et. al [33]. Dividing this range into three equal intervals, I obtained those values of α_ν used in the Opt-IR part: -2.5 , -1.33 , -0.16 and 1.01 . Table 4.7 shows all the slopes in frequency and wavelength used for the

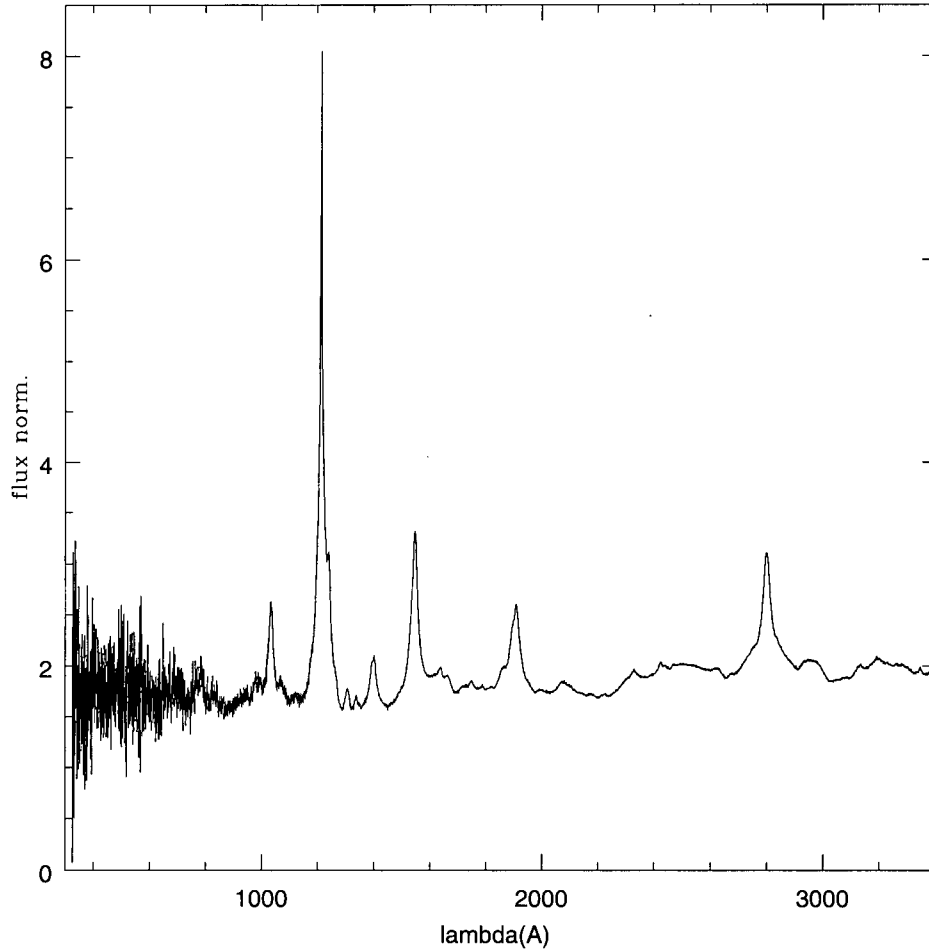


Figure 4.5: First part of the composite spectrum in the 300-3400 Å range: it can be noted that the Ly α (1215 Å) and CIV (1549 Å) are among the strongest emission lines.

quasar templates considering that the relationship between the power law index in frequency and that in wavelength is $\alpha_\lambda = -(\alpha_\nu + 2)$.

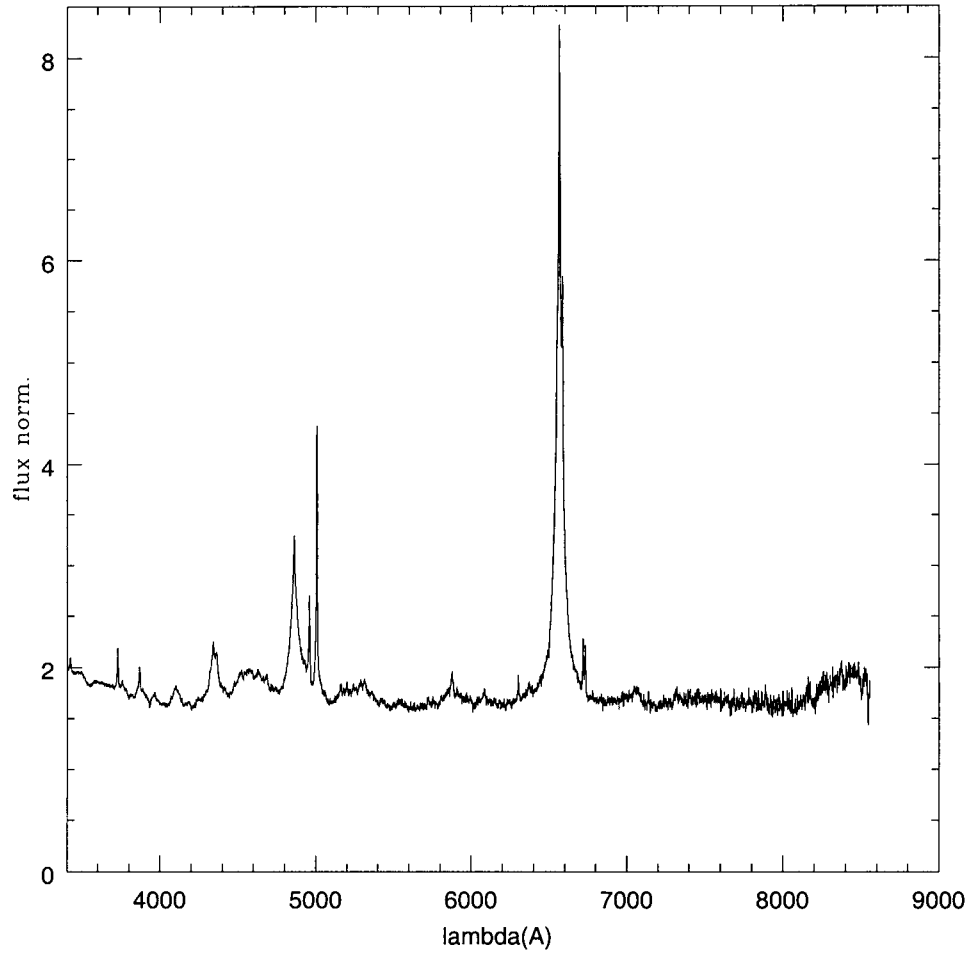


Figure 4.6: Second part of the composite “flat” spectrum in the 3400-8550 Å range. $H\alpha$ (6563 Å) and [OIII] (4363 Å) are among the strongest emission lines.

In Fig 4.7 all the quasar templates (in the rest frame) are shown.

Each of these models was then redshifted to $z=7.00$ with step $\delta z=0.02$,

	α_ν	α_λ	template
UV	-1.96	-0.04	
Opt-IR	-2.5	0.5	I
	-1.33	-0.67	II
	-0.16	-1.84	III
	1	-3	IV

Table 4.7: Power-law index in frequency and wavelength for quasar templates in the UV and optical-near-infrared (Optical-IR) region.

but only those with $z \geq 0.30$ were compared to UNMS1 catalog objects: in total 1344 templates were used. The choice of $z=7.00$ is due to the presence of the $\text{Ly}\alpha$ emission line: as long as it appears inside the optical range, it is a useful tool to identify quasars.

4.4 Method calibration from templates.

So far, we have not calibrated the reliability of quasar detections and how their identification is contaminated from other astronomical objects, especially stars.

A good way to test this method is to apply it to something we already know and to see if results are consistent with this “a priori” knowledge. The idea is to work with templates of each category at different redshifts and to consider them as “test objects”, called also “template-objects”. Results from a pure minimization χ^2 procedure and from the odds ratio procedure are important in order to see if new conditions should be considered when

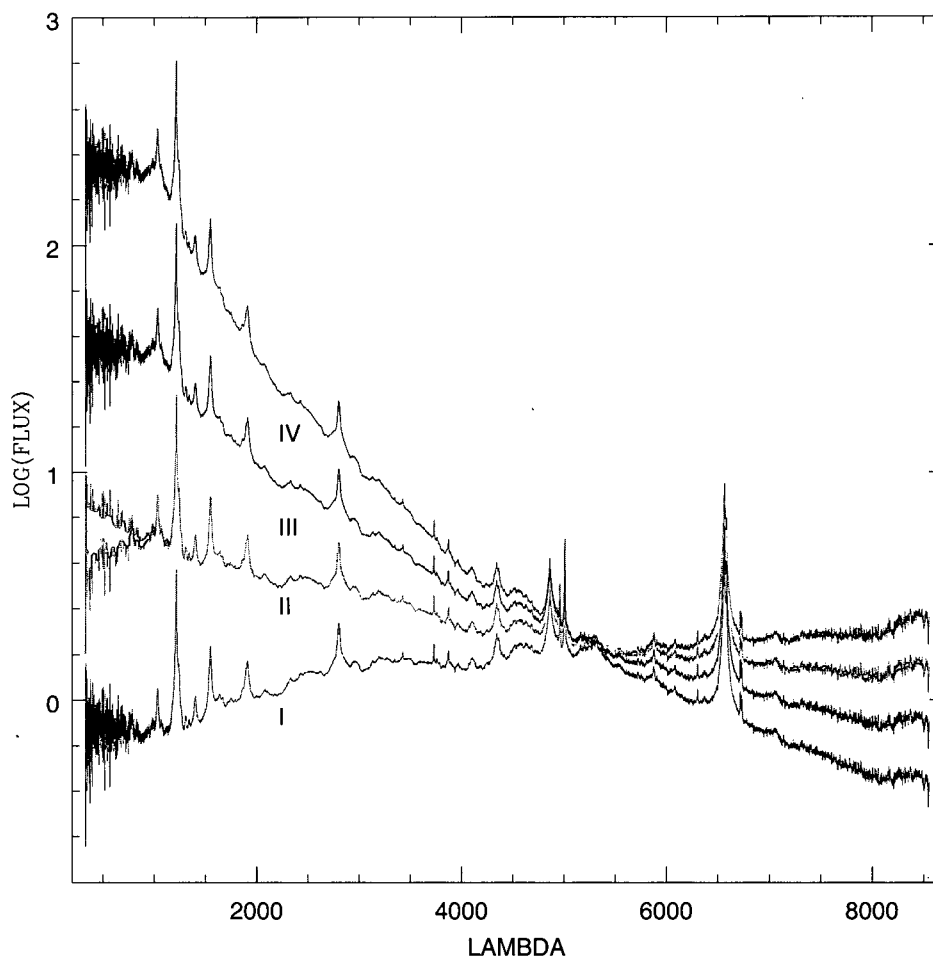


Figure 4.7: Quasar templates in the rest frame: lines I, II, III and IV represent respectively template I, II, III and IV.

the method is applied to real sources.

4.4.1 A first analysis.

As already discussed, the database includes 131 stellar templates, 13 galactic templates spread from redshift $z=0.00$ to $z=1.20$ and step $\Delta z=0.01$ (1573 galaxies in total) and 4 quasar types from $z=0.30$ to $z=7.00$ and step $\Delta z=0.02$ (1344 in total).

For an appropriate analysis, models were normalized to the flux in the filter "671" ($\log(\nu)=14.65$, $\lambda=6716$ Å, see Table 2.1) and plotted in few diagrams.

In this way it is possible to recognize peculiar features that may be important to separate quasars from stars and galaxies.

Fig. 4.8 - 4.12 show all the galactic (blue line) and quasar (red line) templates in the rest frame with different stellar templates (green line): main sequence stars, giant stars, supergiant stars, subgiant stars and bright giant stars. To avoid crowded diagrams, labels were added only to indicate the galactic and quasar models.

Peculiar features at $\log(\nu) = 14.49$, $\log(\nu) = 14.63$, $\log(\nu) = 14.73$ and $\log(\nu) = 14.85$ correspond to the broad bands I , R , V and B .

Quasar templates are truncated at $\log(\nu)=14.56$ since the original high-resolution model was not complete enough to cover the entire optical range. This inconvenient doesn't influence results from the odds ratio method since only quasar models at redshift higher than 0.3 are used. The QSO plots show two evident lines: the $H\alpha$ line at $\log(\nu)=14.66$ and the $H\beta$ at $\log(\nu)=14.79$.

In any of these diagrams, the range $\log(\nu)=14.55$ -14.65 is characterized by a particular feature, common only to quasars and starburst galaxies. If this structure persisted at any redshift, it could be an interesting tool firstly

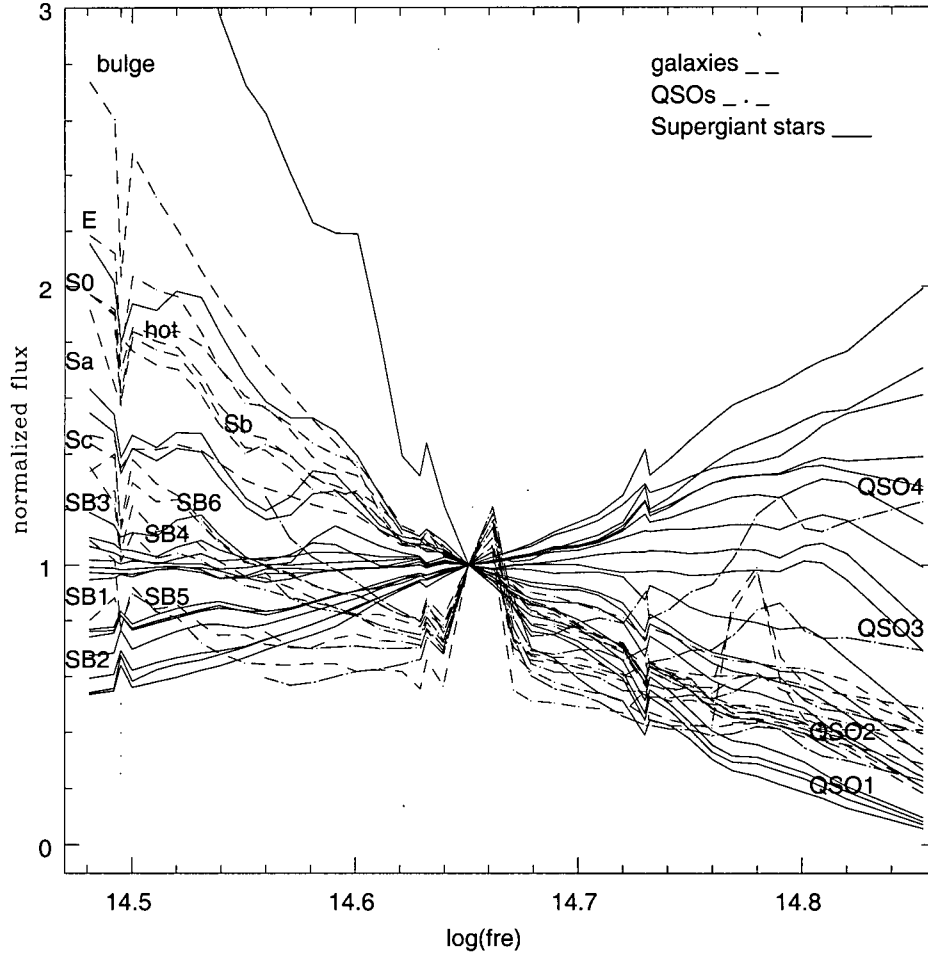


Figure 4.8: Galactic (dashed line) and quasar (dashed-dot line) templates in the rest frame with Supergiant star templates (solid line).

to separate stars from extragalactic objects, and secondly to find quasars using both the Bayesian approach and the χ^2 procedures. In fact if a source is already identified as a quasar by the Bayesian approach and a quasar tem-

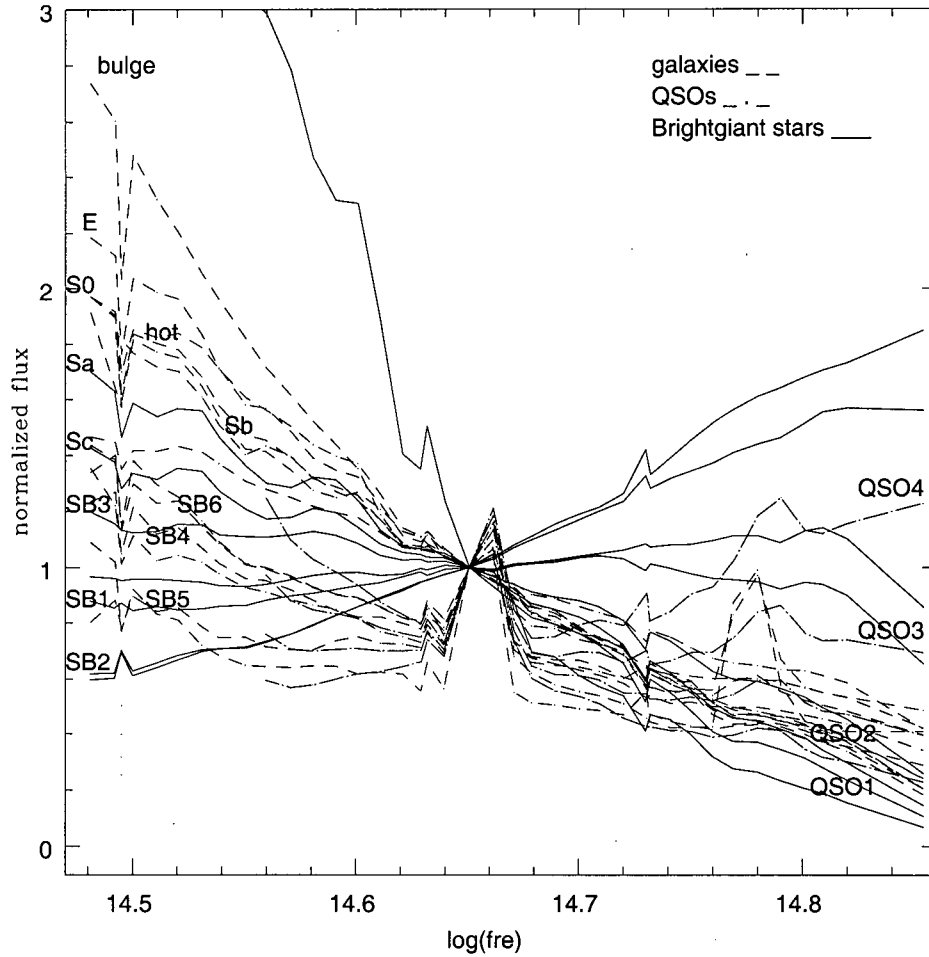


Figure 4.9: Galactic (dashed line) and quasar (dashed-dot line) templates in the rest frame with bright giant templates (solid line).

plate is considered the best fit when the pure χ^2 is calculated only in the region 14.55-14.65, then that object can reasonably be considered a quasar candidate.

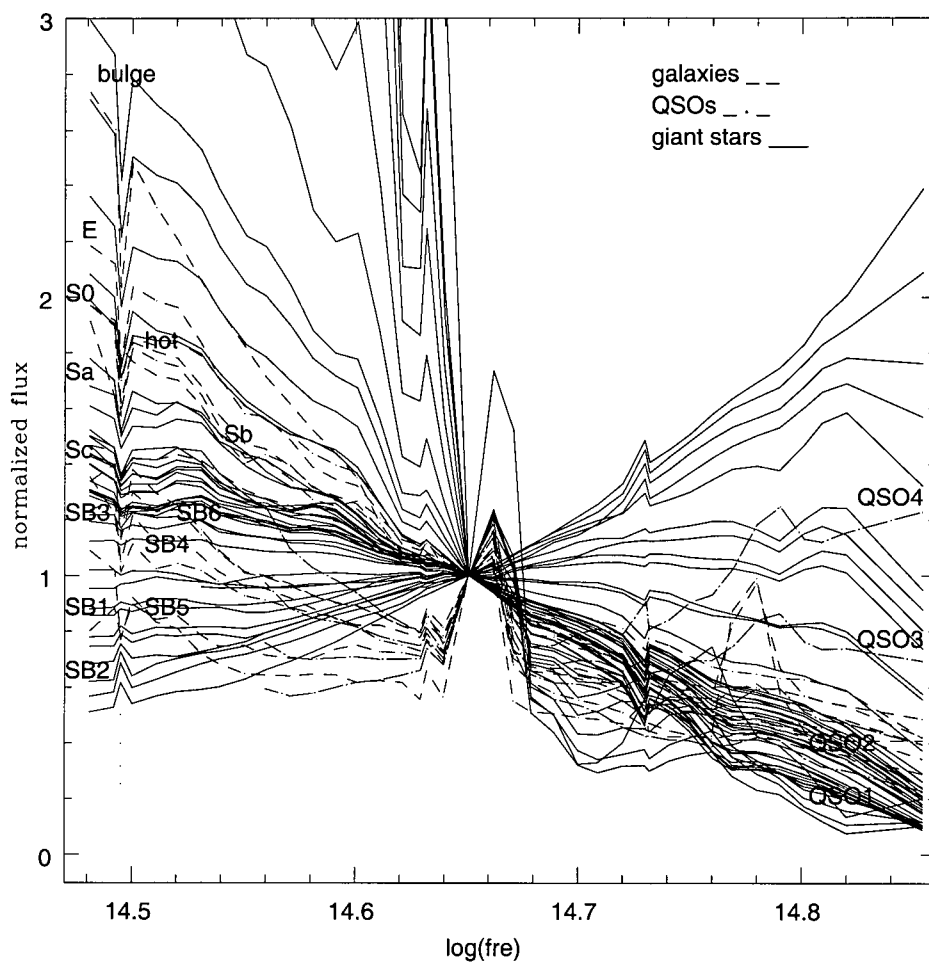


Figure 4.10: Galactic (dashed line) and quasar (dashed-dot line) templates in the rest frame with different giant star templates (solid line).

Fig. 4.13-4.17 show all the galactic and quasars templates at redshift $z=1.2$ with stellar templates. The structure has disappeared and, in another region, the MgII line is now prominent for only two quasar templates. Be-

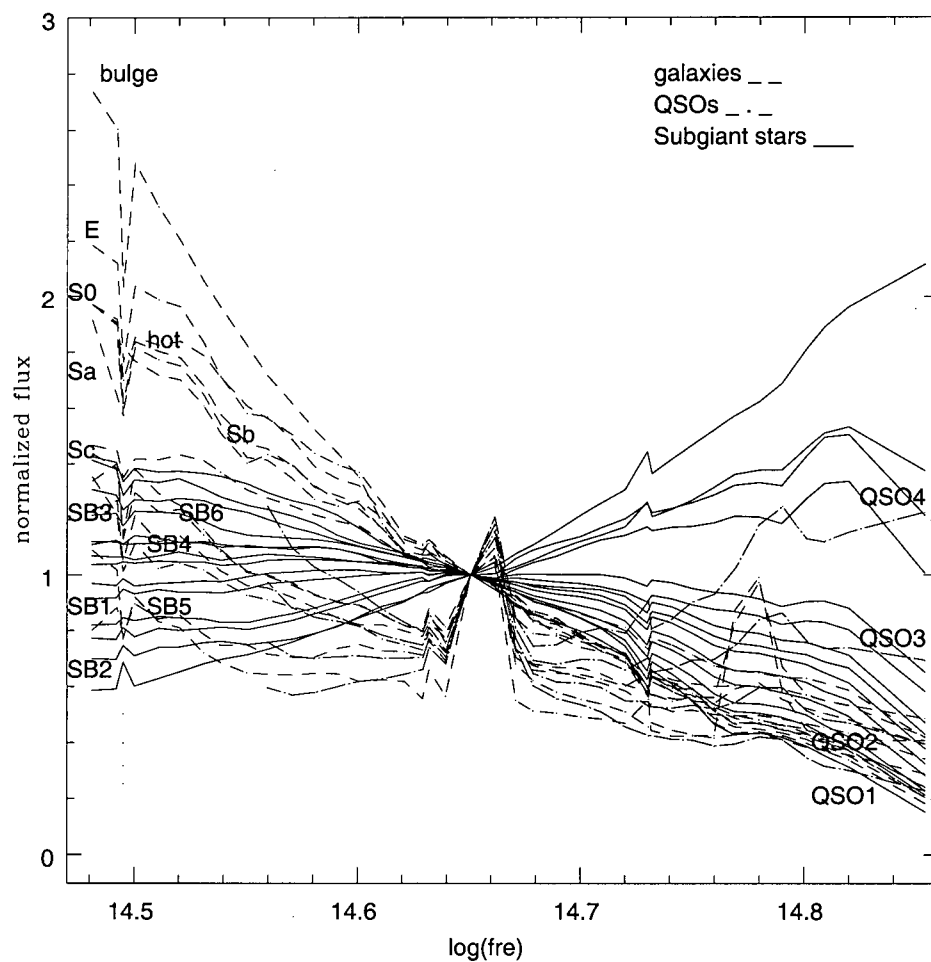


Figure 4.11: Galactic (dashed line) and quasar (dashed-dot line) templates in the rest frame with different subgiant star templates (solid line).

cause these characteristics are a function of redshift, they are not useful for the separation quasars.

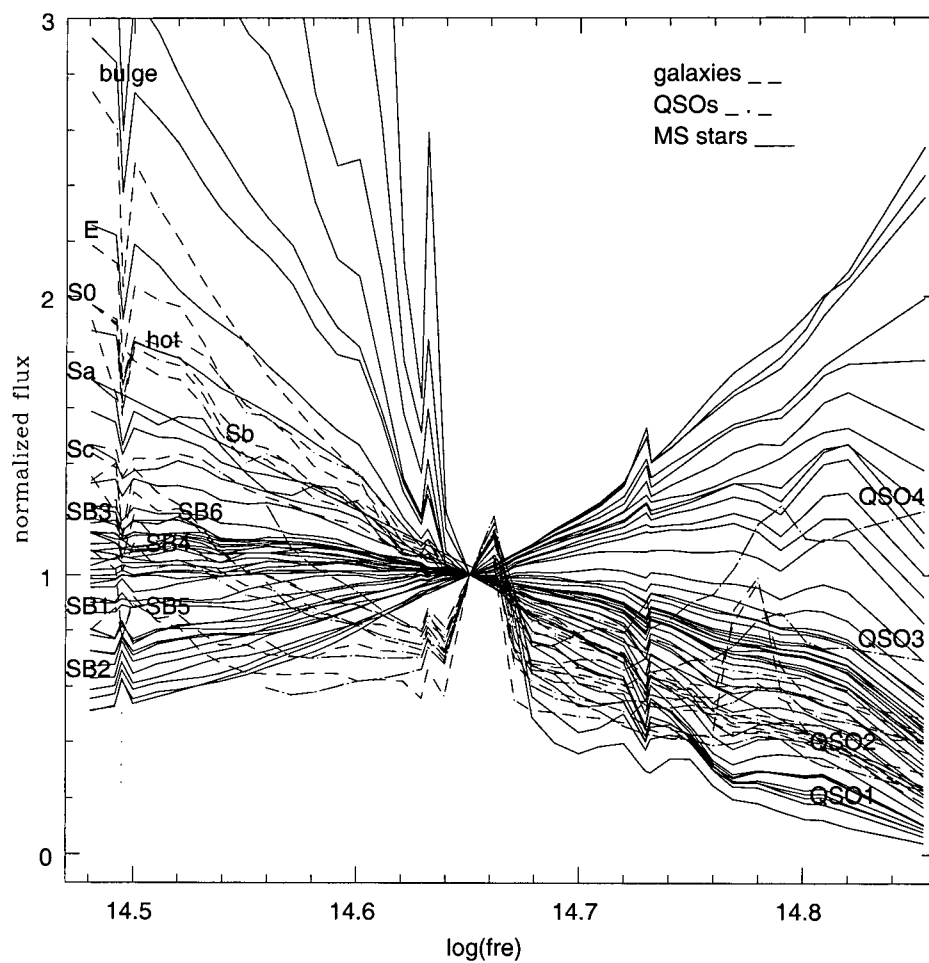


Figure 4.12: Galactic (dashed line) and quasar (dashed-dot line) templates in the rest frame with different main sequence star templates (solid line).

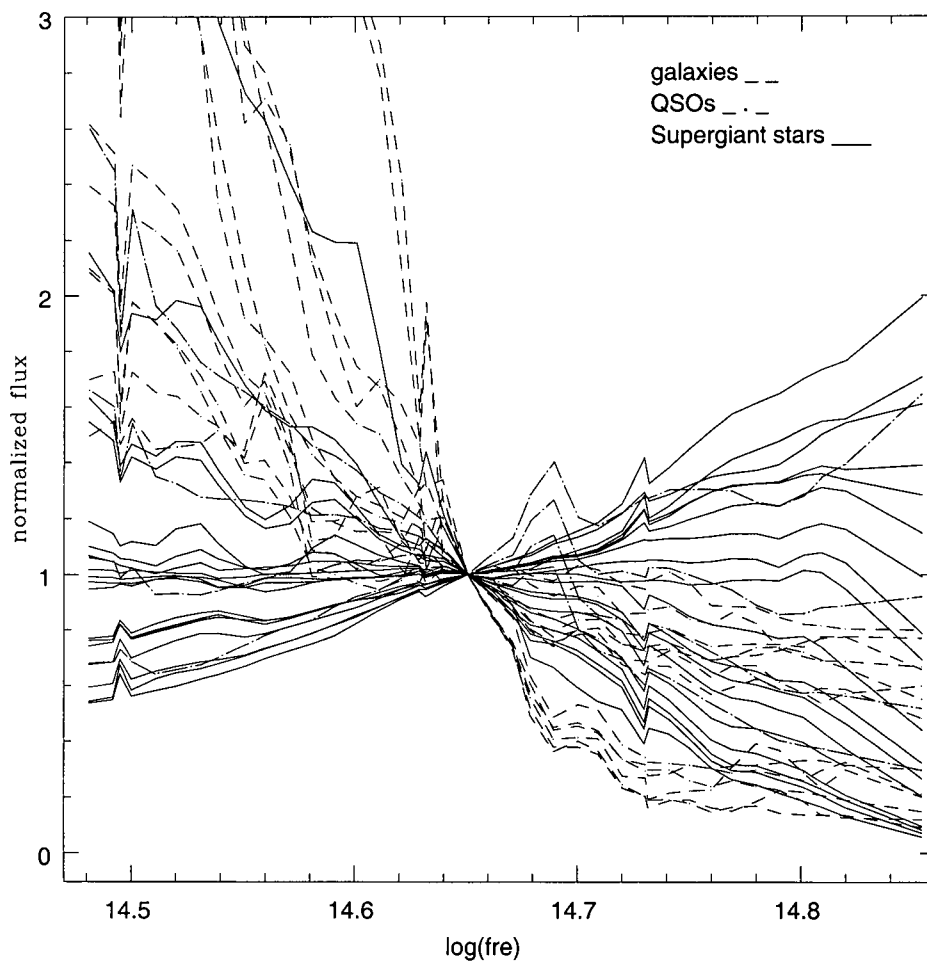


Figure 4.13: Galactic (dashed line) and quasar (dashed-dot line) templates at redshift $z=1.2$ with supergiant star templates (solid line).

4.4.2 χ^2 minimization method and odds ratio procedure applied to original templates.

The first test is to compare each template-object to all the models available, finding not only the one giving the lowest χ^2 and the highest odds ratio

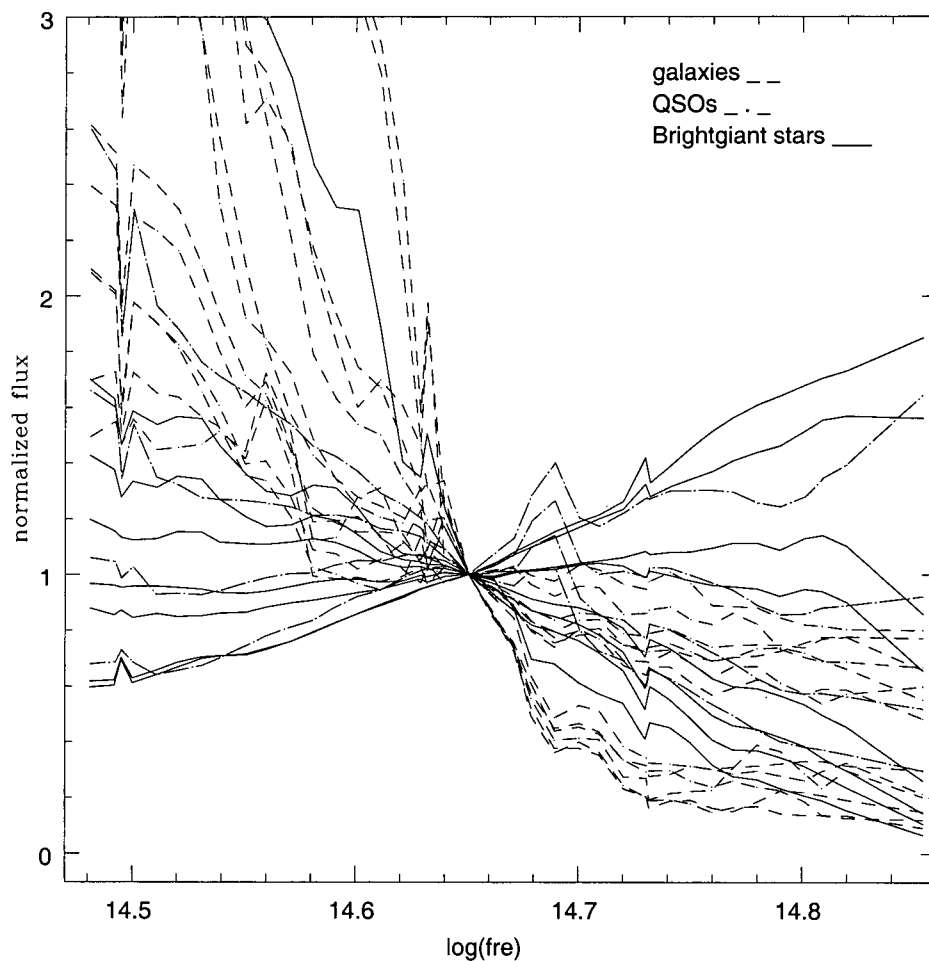


Figure 4.14: Galactic (dashed line) and quasar (dashed-dot line) templates at redshift $z=1.2$ with bright giant star templates (solid line).

but also the χ^2 distribution from all the templates. These were organized firstly according to the stellar and galactic type, and secondly according to the luminosity class for stellar models. Table 4.8 displays this sequence.

N.	TEMPL.	N.	TEMPL.	N.	TEMPL.	N.	TEMPL.
1	elliptical	38	b1v	75	g0iv	112	k3i
2	bulge	39	b2ii	76	g0v	113	k34ii
3	S0	40	b2iv	77	wg0v	114	k3iii
4	Sa	41	b3i	78	rg0v	115	rk3iii
5	Sb	42	b3iii	79	g2i	116	wk3iii
6	Sc	43	b3v	80	g2iv	117	k3iv
7	SB1	44	b5-7v	81	g2v	118	k3v
8	SB2	45	b5i	82	g5i	119	k4i
9	SB3	46	b5ii	83	g5ii	120	k4iii
10	SB4	47	b5iii	84	g5iii	121	wk4iii
11	SB5	48	b6iv	85	wg5iii	122	rk4iii
12	SB6	49	b8i	86	rg5iii	123	k4v
13	UVhot	50	b8v	87	g5iv	124	k5iii
14	QSO1	51	b9iii	88	g5v	125	rk5iii
15	QSO2	52	b9v	89	wg5v	126	k5v
16	QSO3	53	f0i	90	rg5v	127	k7v
17	QSO4	54	f0ii	91	g8i	128	m0iii
18	o8iii	55	f0iii	92	g8iii	129	m0v
19	o5v	56	f0-2iv	93	wg8iii	130	m1iii
20	o9v	57	f0v	94	g8iv	131	m1v
21	a0i	58	f2ii	95	g8v	132	m2i
22	a0iii	59	f2iii	96	k01ii	133	m2iii
23	a0iv	60	f2v	97	k0iii	134	m2v
24	a0v	61	f5i	98	wk0iii	135	m2.5v

Table 4.8: Continue.

N.	TEMPL.	N.	TEMPL.	N.	TEMPL.	N.	TEMPL.
25	a2i	62	f5iii	99	rk0iii	136	m3ii
26	a2v	63	f5iv	100	k0iv	137	m3iii
27	a3iii	64	f5v	101	k0v	138	m3v
28	a3v	65	wf5v	102	rk0v	139	m4iii
29	a47iv	66	f6v	103	k1iii	140	m4v
30	a5iii	67	rf6v	104	wk1iii	141	m5iii
31	a5v	68	f8i	105	rk1iii	142	m5v
32	a7iii	69	f8iv	106	k1iv	143	m6iii
33	a7v	70	f8v	107	k2i	144	m6v
34	b0i	71	wf8v	108	k2iii	145	m7iii
35	b0v	72	rf8v	109	wk2iii	146	m8iii
36	b1i	73	g0i	110	rk2iii	147	m9iii
37	b1-2iii	74	g0iii	111	k2v	148	m10iii

Table 4.8: Template sequence for the χ^2 analysis.

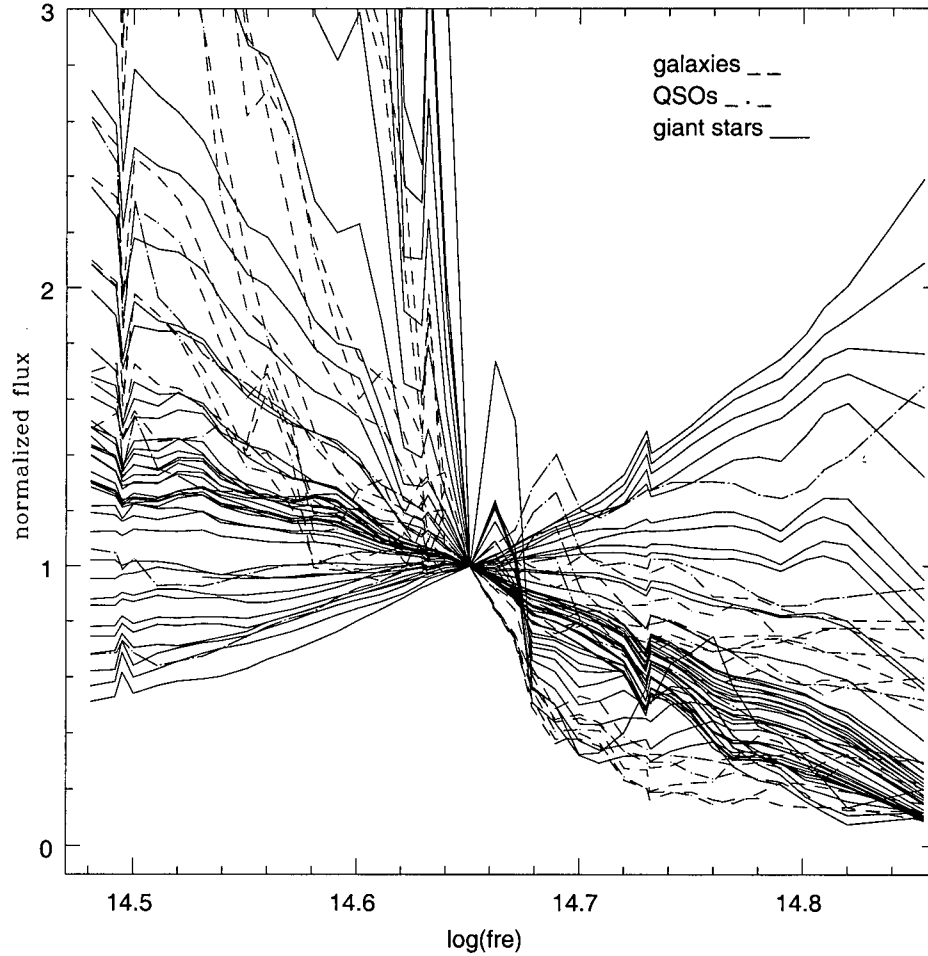


Figure 4.15: Galactic (dashed line) and quasar (dashed-dot line) templates at redshift $z=1.2$ with giant star templates (solid line).

Fig. 4.18-4.21 show the χ^2 distribution for several quasar template-objects when compared to all the 3048 models. This is useful to understand which templates have similar χ^2 and confuse the object identification (this

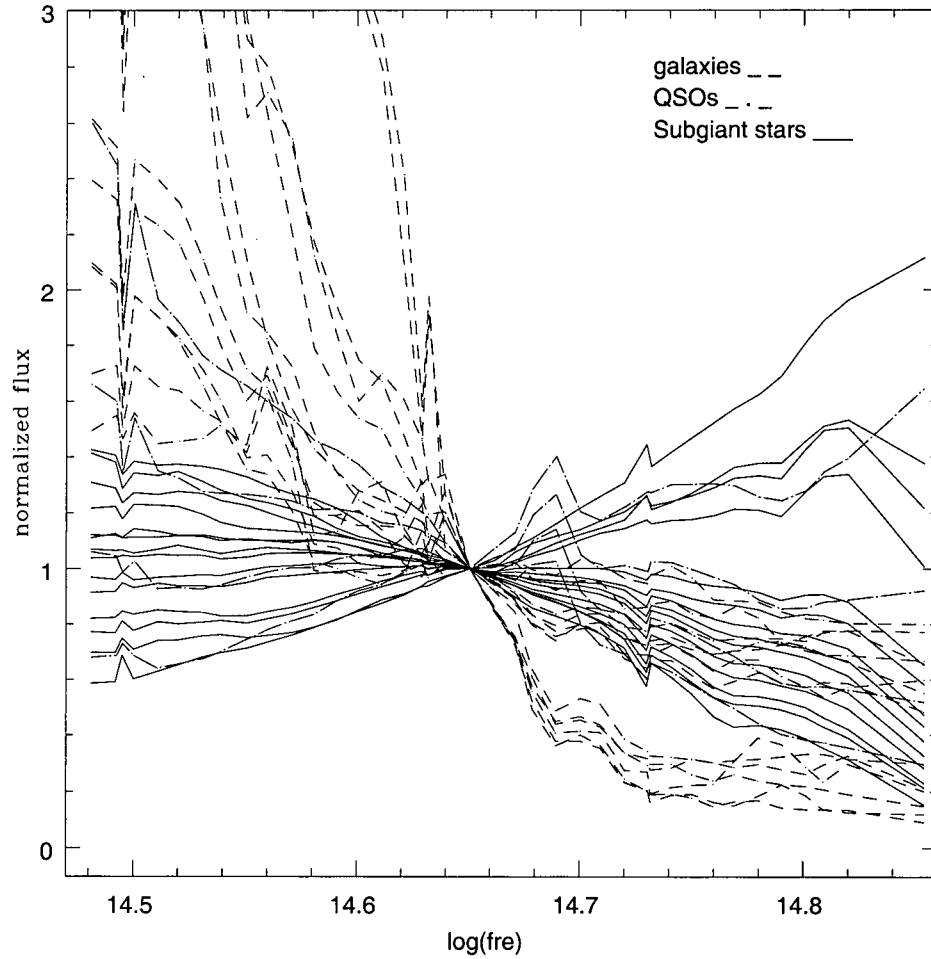


Figure 4.16: Galactic (dashed line) and quasar (dashed-dot line) templates at redshift $z=1.2$ with sub-giant star templates (solid line).

explains why these plots show only the bottom region and not the complete range). The blue line represents the comparison with galactic templates, the red line quasar templates and the green line stellar template.

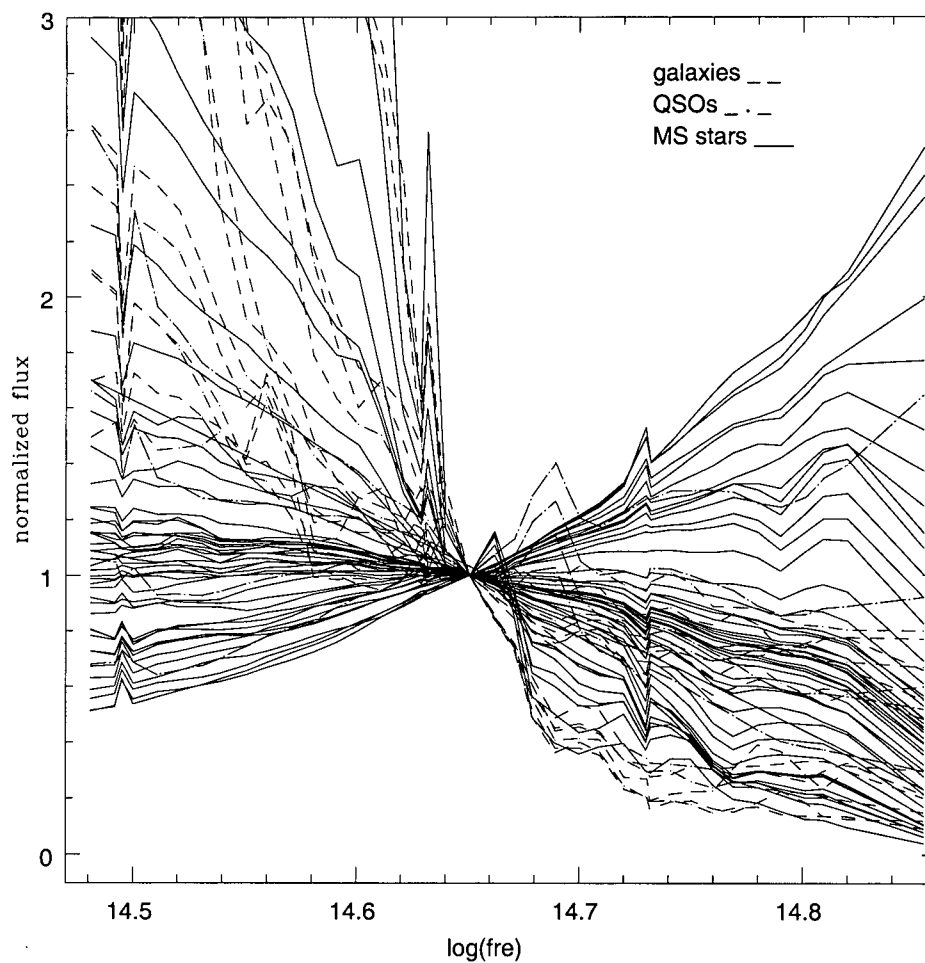


Figure 4.17: Galactic (dashed line) and quasar (dashed-dot line) templates at redshift $z=1.2$ with main sequence stars (solid line).

When the template-object is just one of the models, it is logical that the lowest χ^2 comes from the original template. From these plots it is important to see is that there are some stellar and galactic models with low χ^2 and close

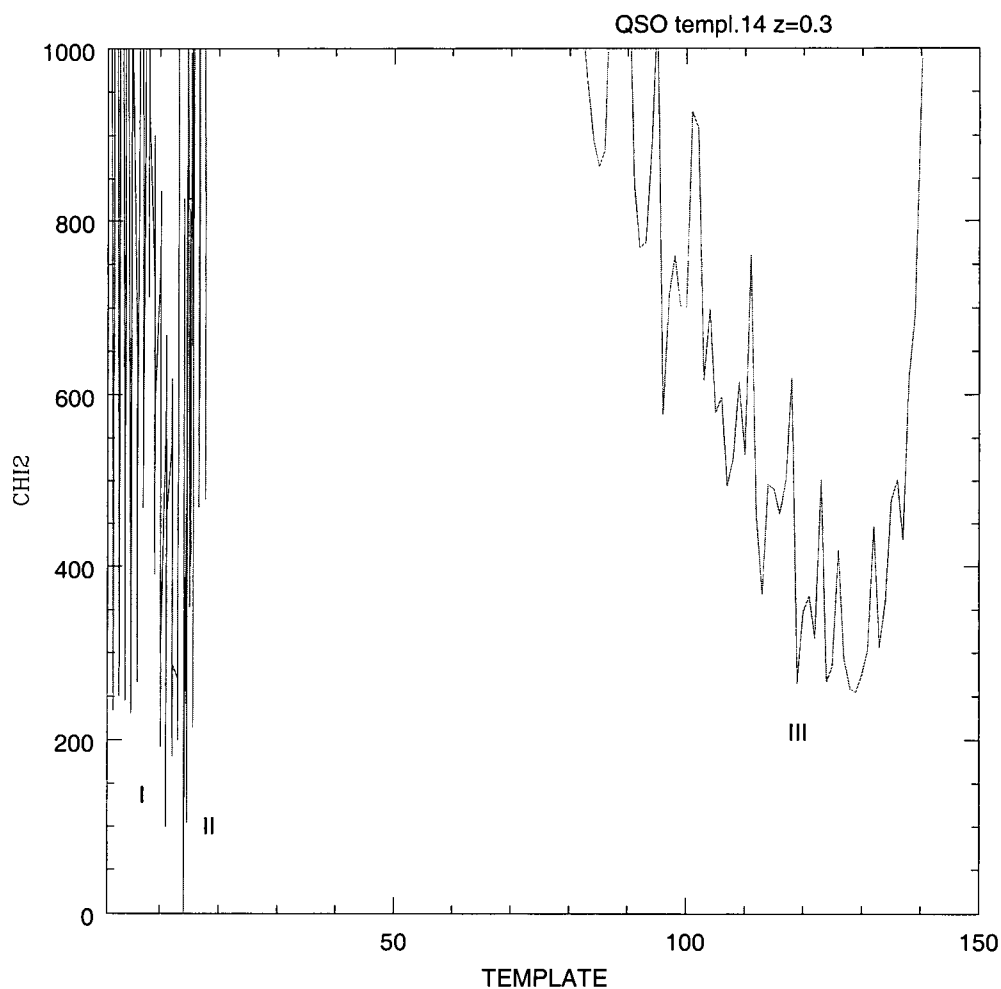


Figure 4.18: χ^2 distribution for 4 QSO N.14 at $z=0.3$: line I, II and III come from the comparison respectively to galactic, quasar and stellar templates.

to the object in question. For example, quasar N.14 is close to the first six galactic models at low redshift (mostly ellipticals and spirals) and to K and

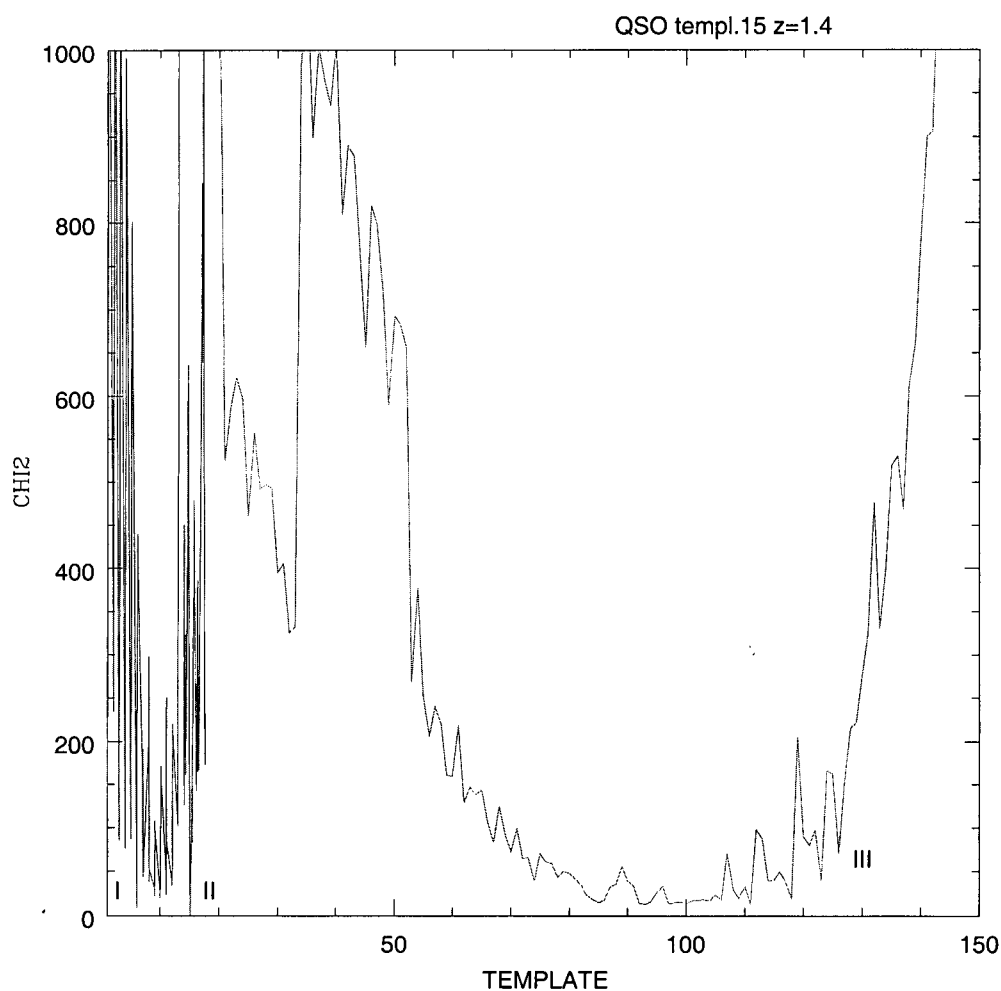


Figure 4.19: χ^2 distribution for QSO N.15 at $z=1.4$: line I, II and III come from the comparison respectively to galactic, quasar and stellar templates.

M stellar templates; quasar N.15 is very close to late spirals and starburst galaxies and to G and K stars, quasar N.16 is mostly near F stars and finally

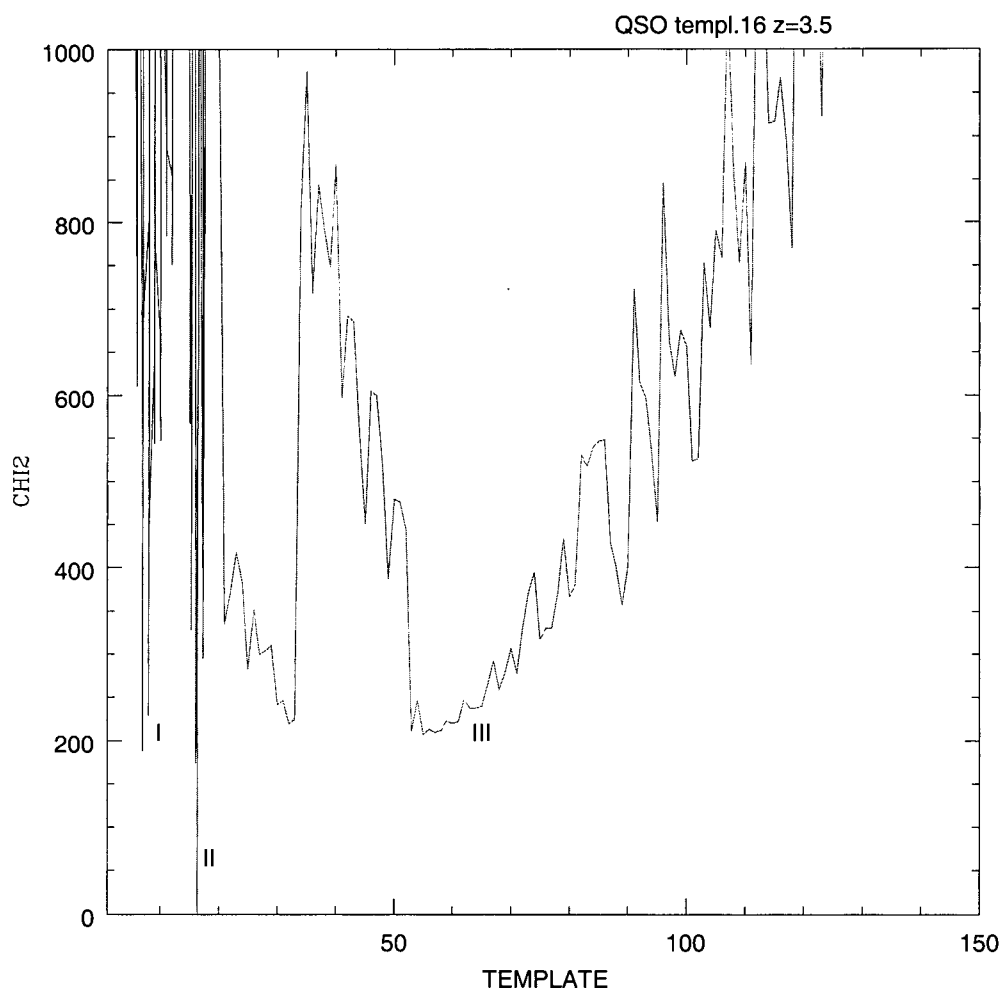


Figure 4.20: χ^2 distribution for QSO N.16 at $z=3.5$: line I, II and III come from the comparison respectively to galactic, quasar and stellar templates.

quasar N.17 is very close to starburst galaxies .

This situation is confirmed by the odds ratio's results: 40 objects, all from

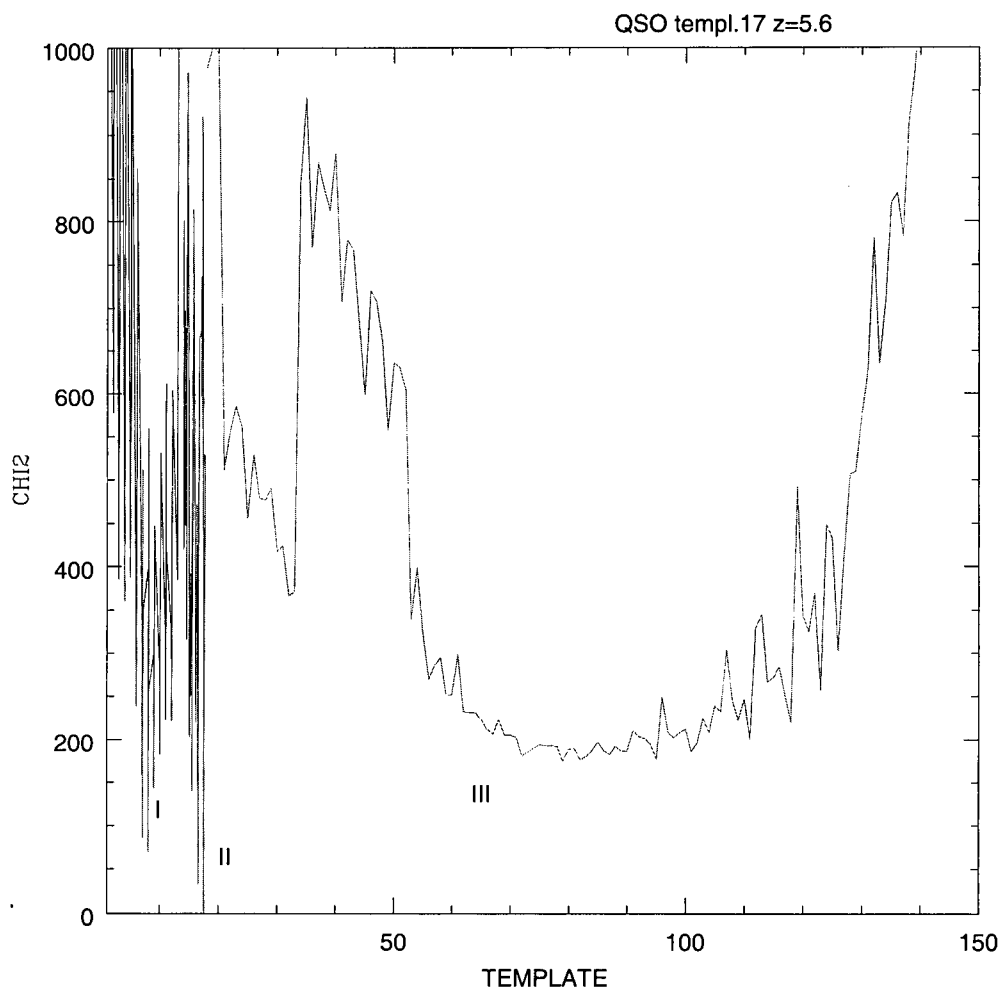


Figure 4.21: χ^2 distribution for QSO N.17 at $z=5.6$: line I, II and III come from the comparison respectively to galactic, quasar and stellar templates.

the quasar category, are infact misidentified. In particular N.14 quasars in the redshift range 1.30-1.46 are mostly identified as UVhot and spiral galaxies at

low and medium redshift. Quasars N.15, N.16 and N.17 are mostly confused with F and B stars.

The 40 misclassified elements are just a small portion of the entire sample which involves more than 3000 test objects. Since the final goal is to find quasars in a catalog of real objects, it is interesting to analyze the results from the same test applied to altered models, as we explain below.

4.4.3 χ^2 and odds ratio procedures applied to altered templates.

For the second test, template-objects were modified to simulate realistic conditions. Noise was added to them simulating 39 measurements, from the standard Gaussian distribution [4]:

$$P_G(q)dq = \frac{1}{\sqrt{2\pi}} \exp\left[-\frac{q^2}{2}\right] dq \quad (4.15)$$

with mean 0 and standard deviation 1. The “ i^{th} ” deviated flux is given by

$$F_{i,dev} = F_i + \delta F_i q_i \quad (4.16)$$

where F_i and δF_i are the flux with its error in the “ i^{th} ” filter.

Fig. 4.22-4.25 show the χ^2 distribution found for the same objects cited in the previous paragraph, this time with noise added: as expected, the χ^2 between the smeared template-object and the original model is no longer null but is of the same order as those of other templates.

This kind of ambiguity is fatal for ~ 500 template-objects for which the χ^2 method fails to recover the correct model.

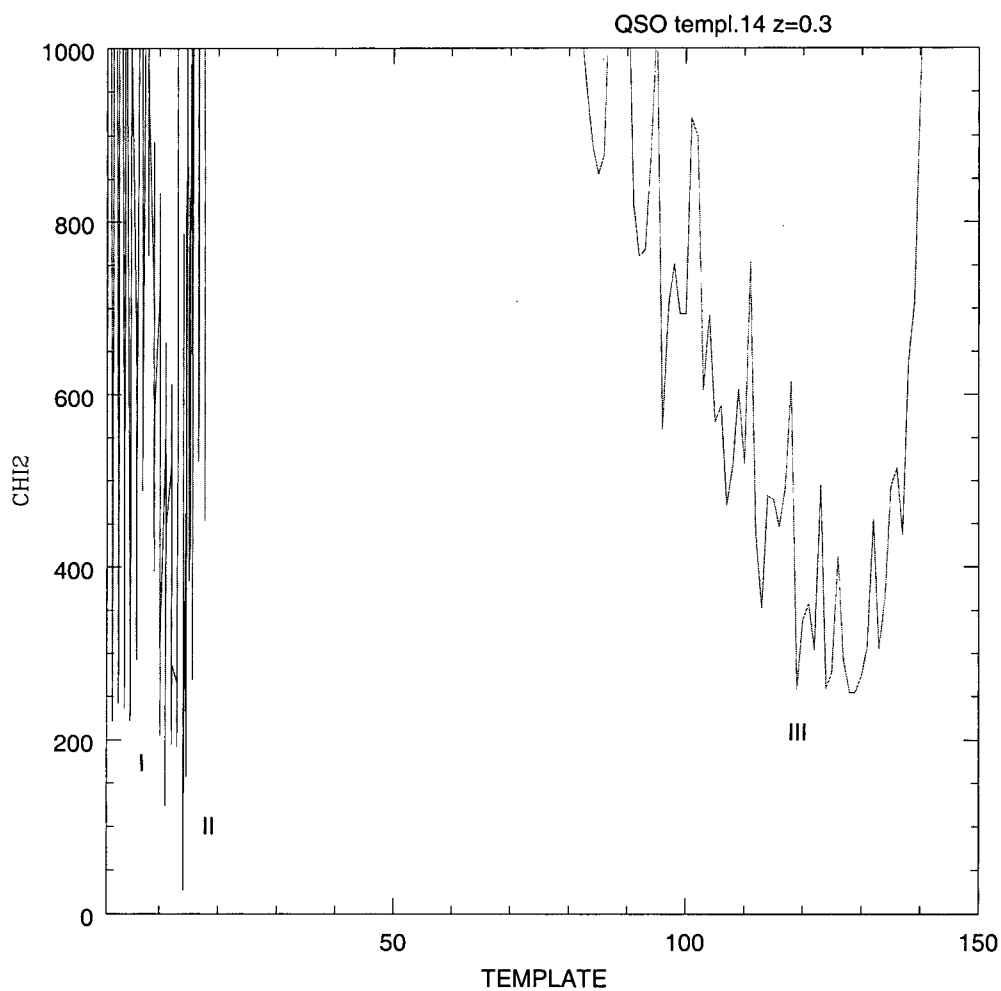


Figure 4.22: χ^2 distribution for the altered QSO N.14 at $z=0.3$: line I, II and III come from the comparison respectively to galactic, quasar and stellar templates.

From the odds ratio approach, 1082 template-objects of 3048 are misclassified. In particular, N.14 quasars are confused with UVhot, elliptical and

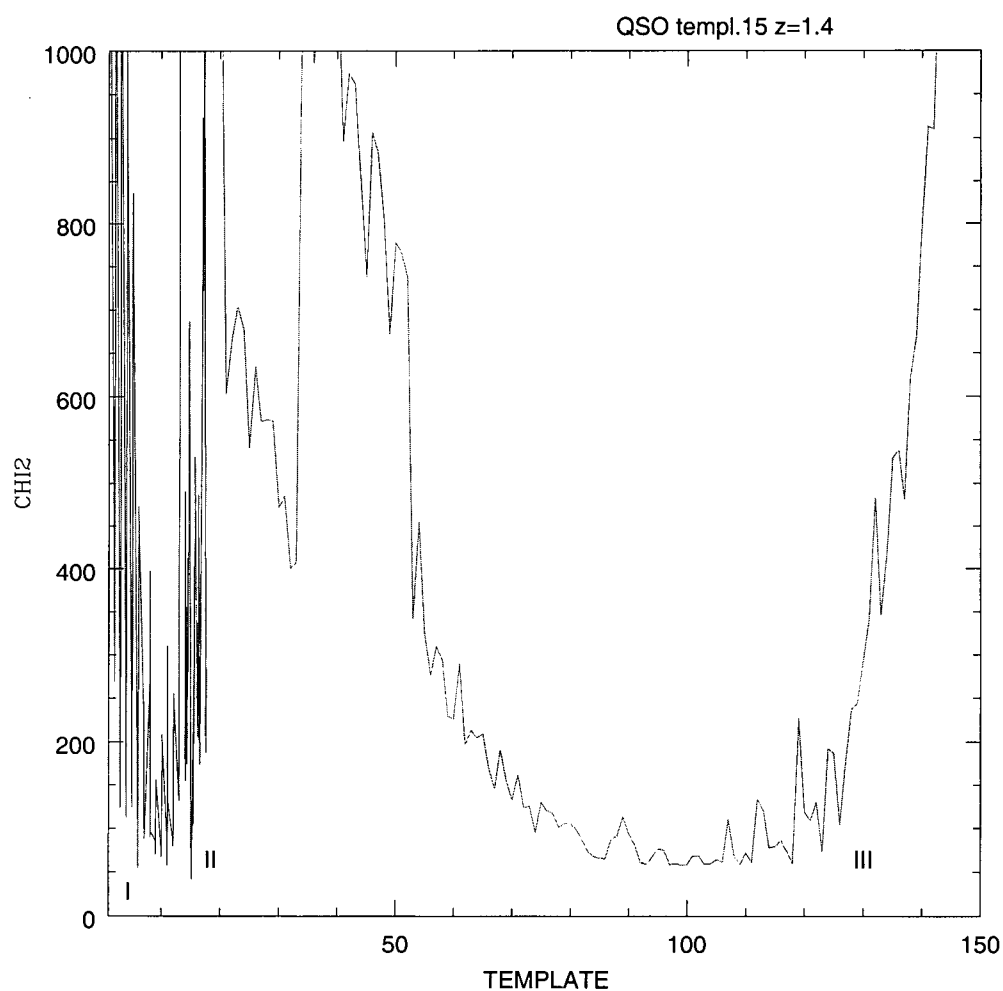


Figure 4.23: χ^2 distribution for the altered QSO N.15 at $z=1.4$: line I, II and III come from the comparison respectively to galactic, quasar and stellar templates.

spiral galaxies, N.15 quasars are mainly classified as starburst and late spiral galaxies, and G and F stellar types, N.16 quasars is mostly seen as F type

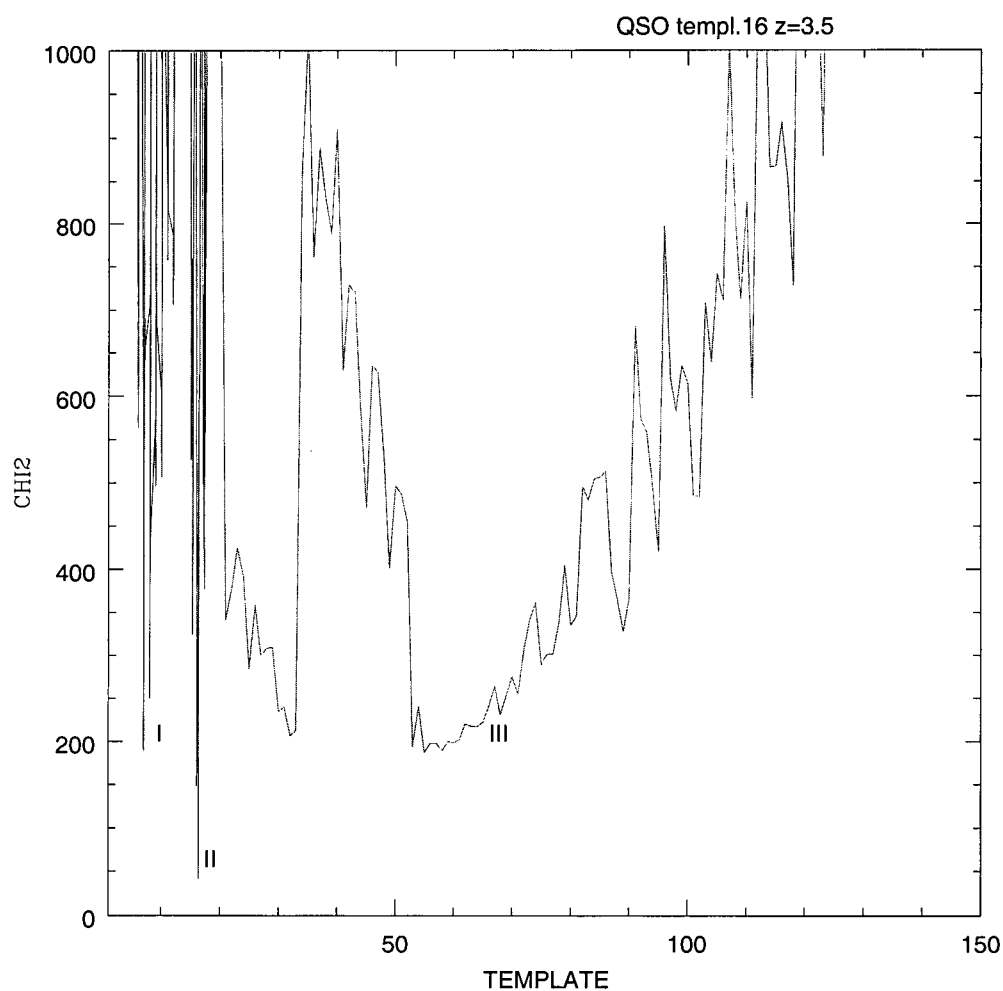


Figure 4.24: χ^2 distribution for the altered QSO N.16 at $z=3.5$: line I, II and III come from the comparison respectively to galactic, quasar and stellar templates.

stars and quasars N.17 with B type stars.

Until now all the results are based on template-objects with 39 flux mea-

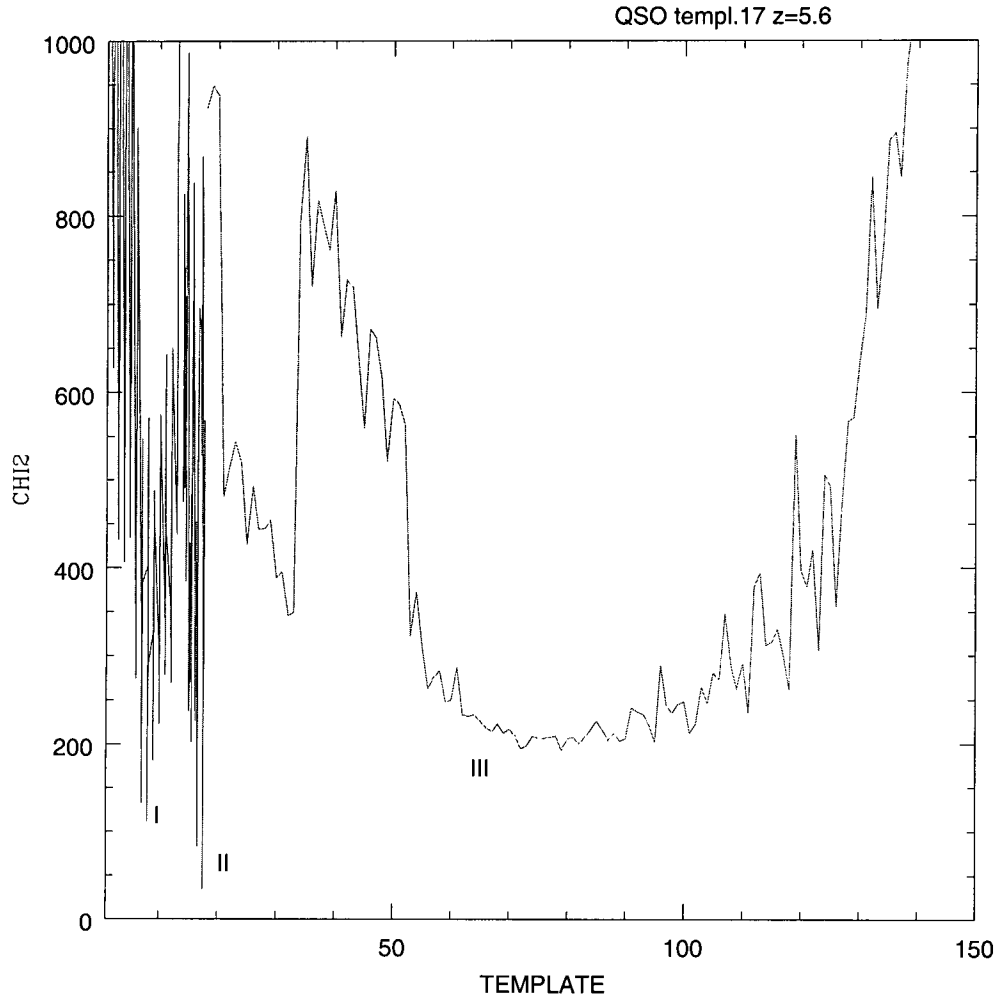


Figure 4.25: χ^2 distribution for the altered QSO N.17 at $z=5.6$: line I, II and III come from the comparison respectively to galactic, quasar and stellar templates.

surements in the optical range. This situation is not very realistic: in the UNMS1 catalog, most of the sources have 10-20 filters and only 4% of the

entire database has more than 35 magnitudes. So, it is important not only to add noise to these template-objects, but also to analyze the results when more and more filters are randomly neglected (jackknife approach).

Fig. 4.26 shows the distribution of stars (green line), galaxies (blue line) and quasars (red line) as classified by the program against the number of filters: each distribution is normalized to the object number available for each category (131 stars, 1573 galaxies and 1344 quasars). Note that the number of stars and quasars increases and decreases respectively when more and more filters are randomly neglected, while the galaxy distribution is nearly unaffected. 10-15 point quasar SEDs (with some emission lines missed) can be easily confused with star SEDs and this suggests the importance of using a criterion on the minimum filter number when the odds ratio method is applied. The fact the galaxy distribution is practically flat means galaxies are not easily confused with other types of objects and the number of filters is not so important for this category.

It is interesting to split the distribution of stars, galaxies and quasars into 4 redshift ranges and include the fraction of template-objects correctly classified (coloured line) and the fraction of models incorrectly classified in that category (black line). In this way it is possible to understand how this misclassification between stars and quasars changes with redshift. In order to do that, 4 redshift ranges are considered:

- range I at $z=0-0.6$ which involves 131 stars, 793 galaxies and 64 quasar (Fig. 4.27-4.29) ;
- range II at $z=0.6-1.2$ which includes 780 galaxies and 120 quasars (Fig. 4.30-4.31);

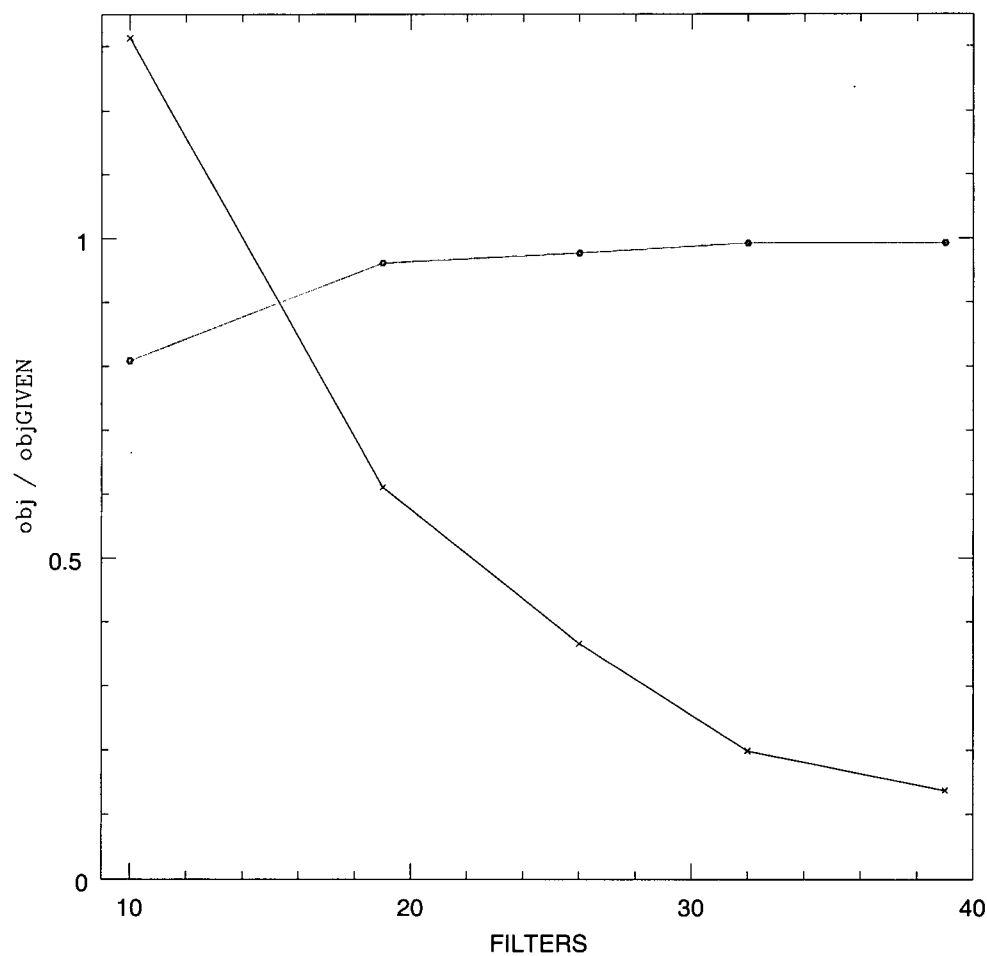


Figure 4.27: Normalized distribution for correctly classified stars (hexagon) and for objects wrongly classified as stars (cross).

As usual, these distributions were normalized to the object number available in each redshift range.

For galaxies the distribution is almost flat in every range. When SEDs

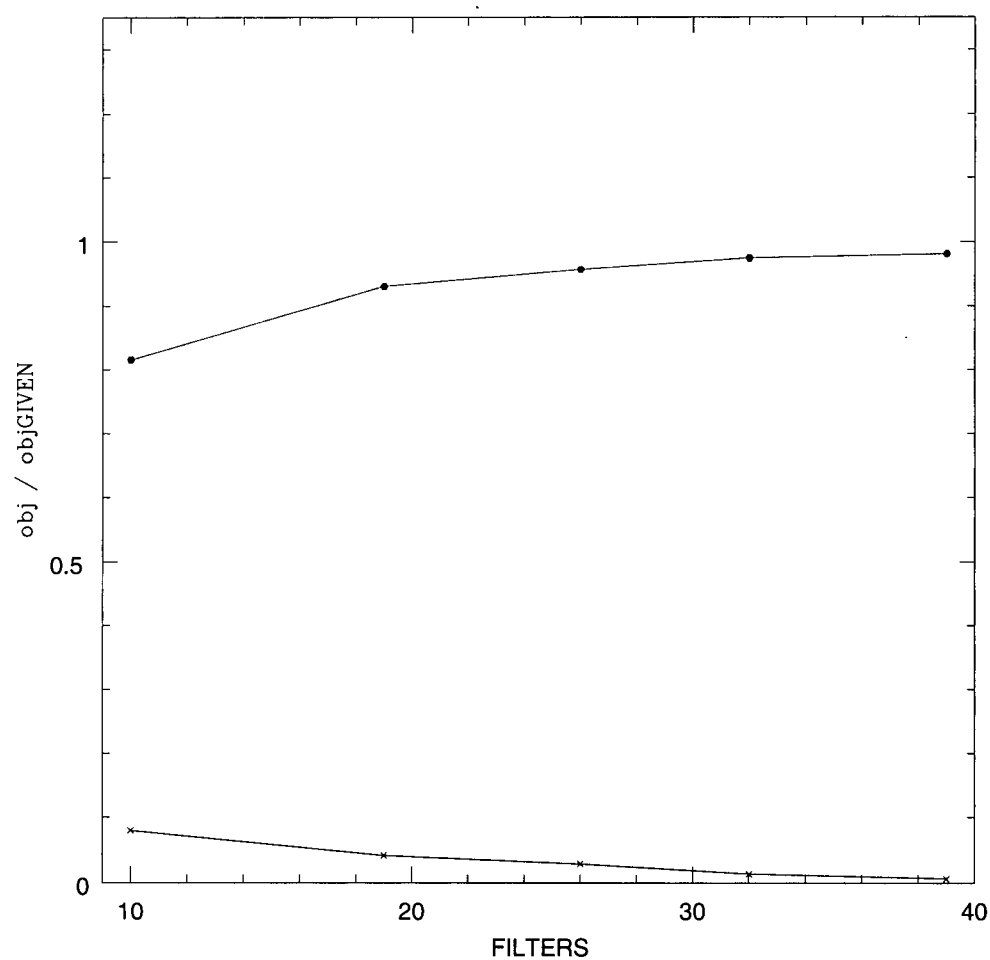


Figure 4.28: Normalized distribution in the redshift range $z=0-0.6$ for correctly classified galaxies (hexagon) and for objects wrongly classified as galaxies (cross).

are constructed with only 10 flux points, 85% of galaxies are still correctly classified.

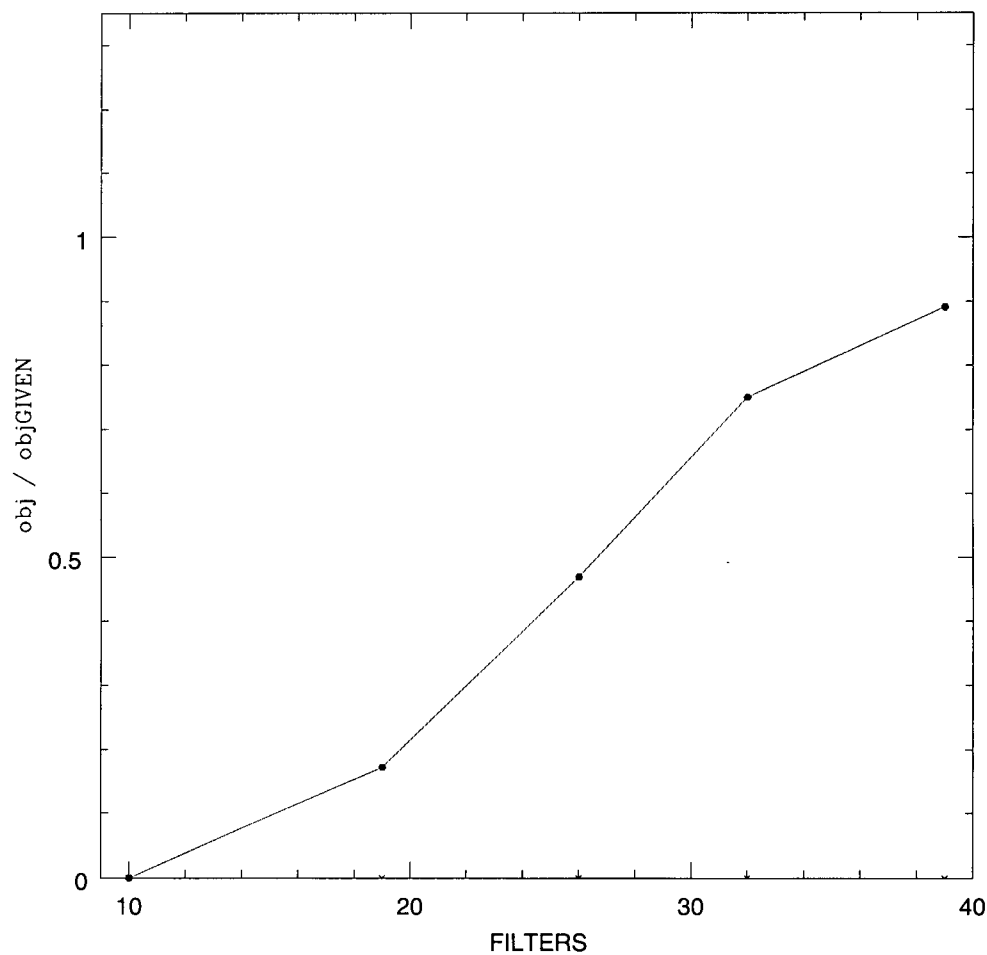


Figure 4.29: Normalized distribution in the redshift range $z=0-0.6$ for correctly classified quasars (hexagonal) and for objects wrongly classified as quasars (cross).

For quasars, as the number of filters decreases, the distribution drops very quickly, first of all in the second redshift range. This behavior is consistent

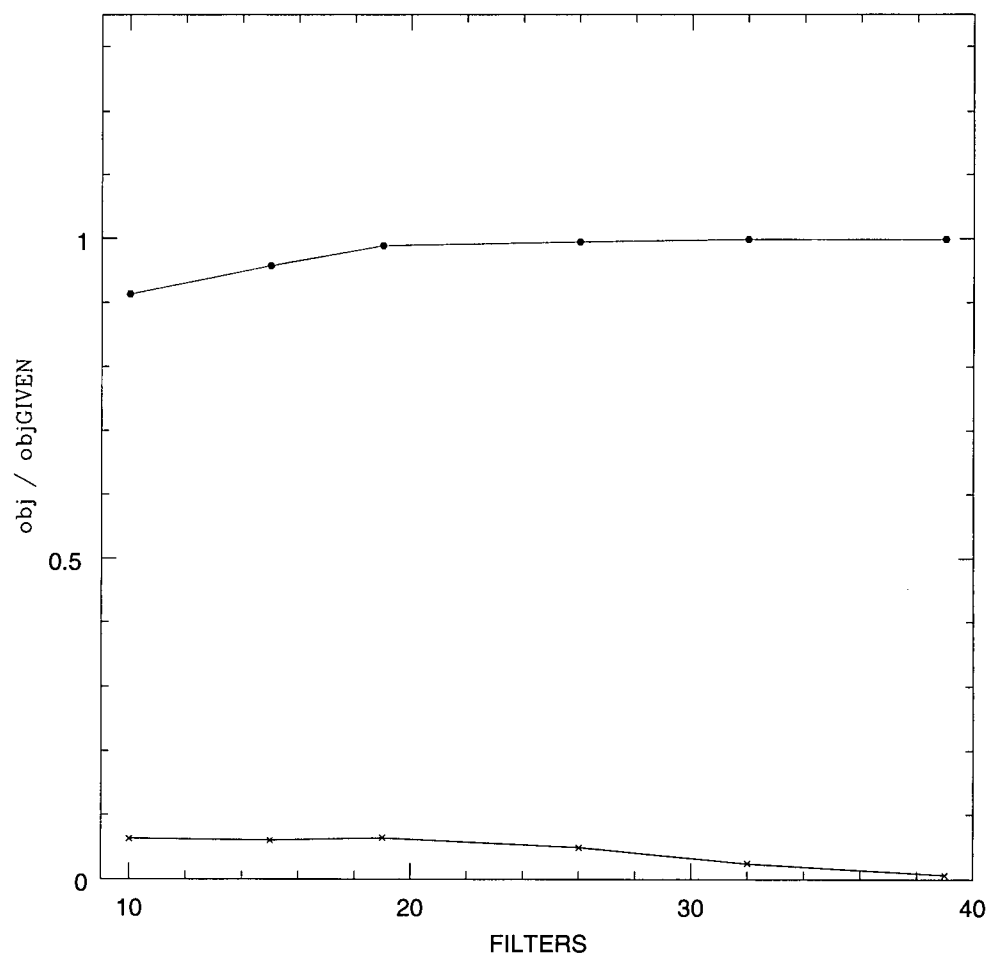


Figure 4.30: Normalized distribution in the redshift range $z=0-0.6$ for correctly classified galaxies (hexagon) and for objects wrongly classified as galaxies (cross).

with that of stars uncorrectly classified in the first range: the black line increases when fewer filters are used and this opposite trend implies that most

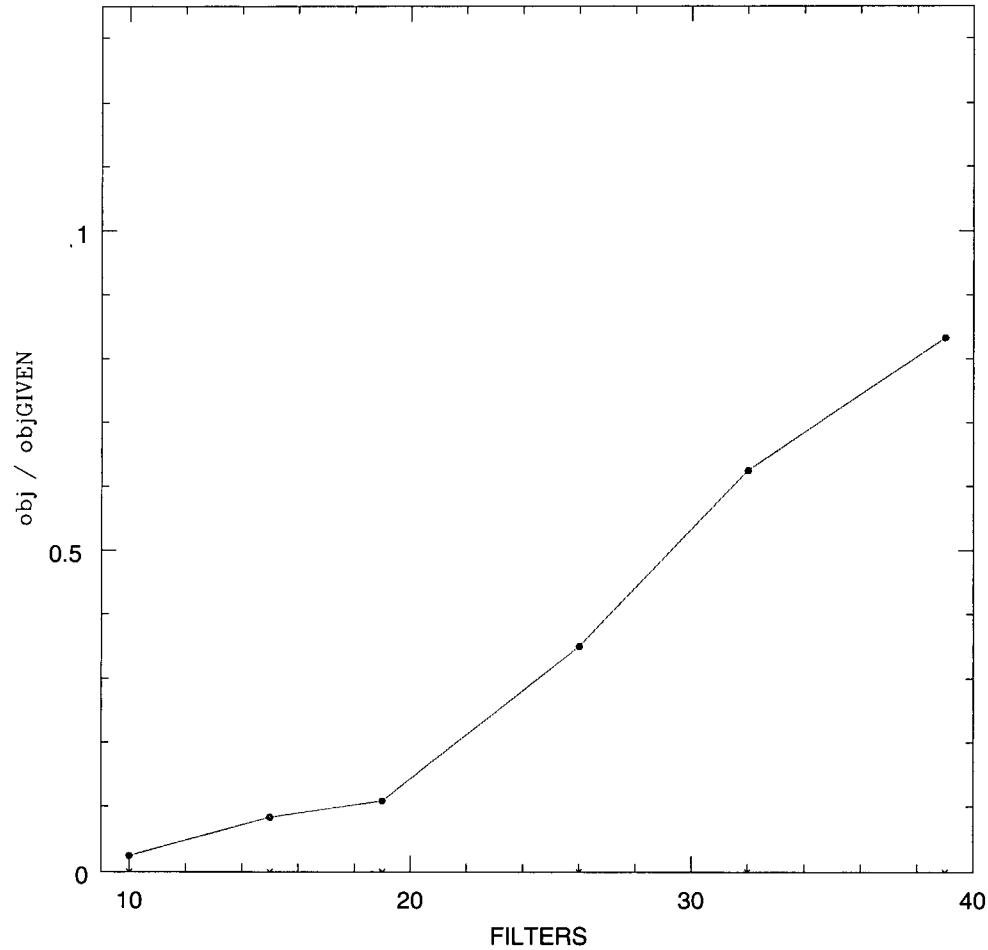


Figure 4.31: Normalized distribution in the redshift range $z=0.6-1.2$ for correctly classified quasars (hexagon) and for objects wrongly classified as quasars (cross).

of them are in real terms QSOs. This could be due to the presence of lines in the quasar SED which resemble those in the stellar spectrum or, since

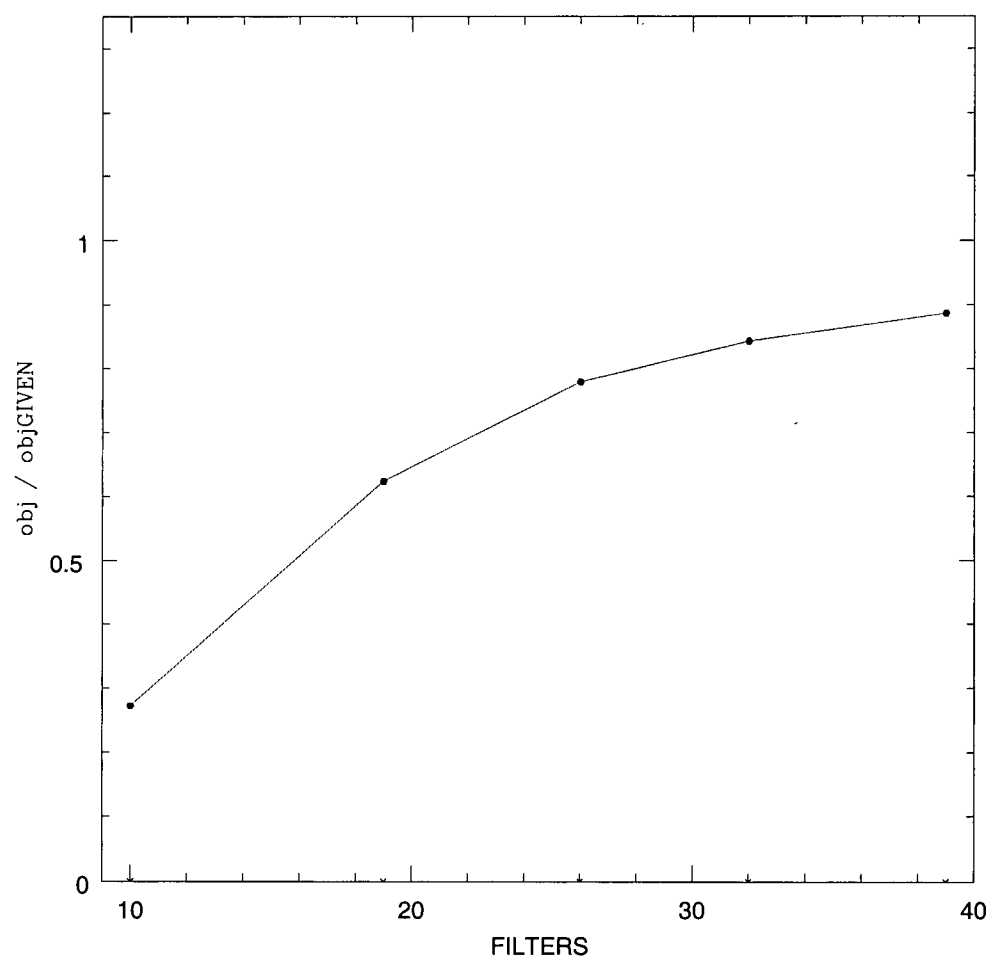


Figure 4.32: Normalized distribution in the redshift range $z=1.2-4.1$ for correctly classified quasars (hexagon) and for objects wrongly classified as quasars (cross).

filters are neglected randomly, some emission features are not considered and the quasar's continuum is easily confused to a stellar "spectrum". Another

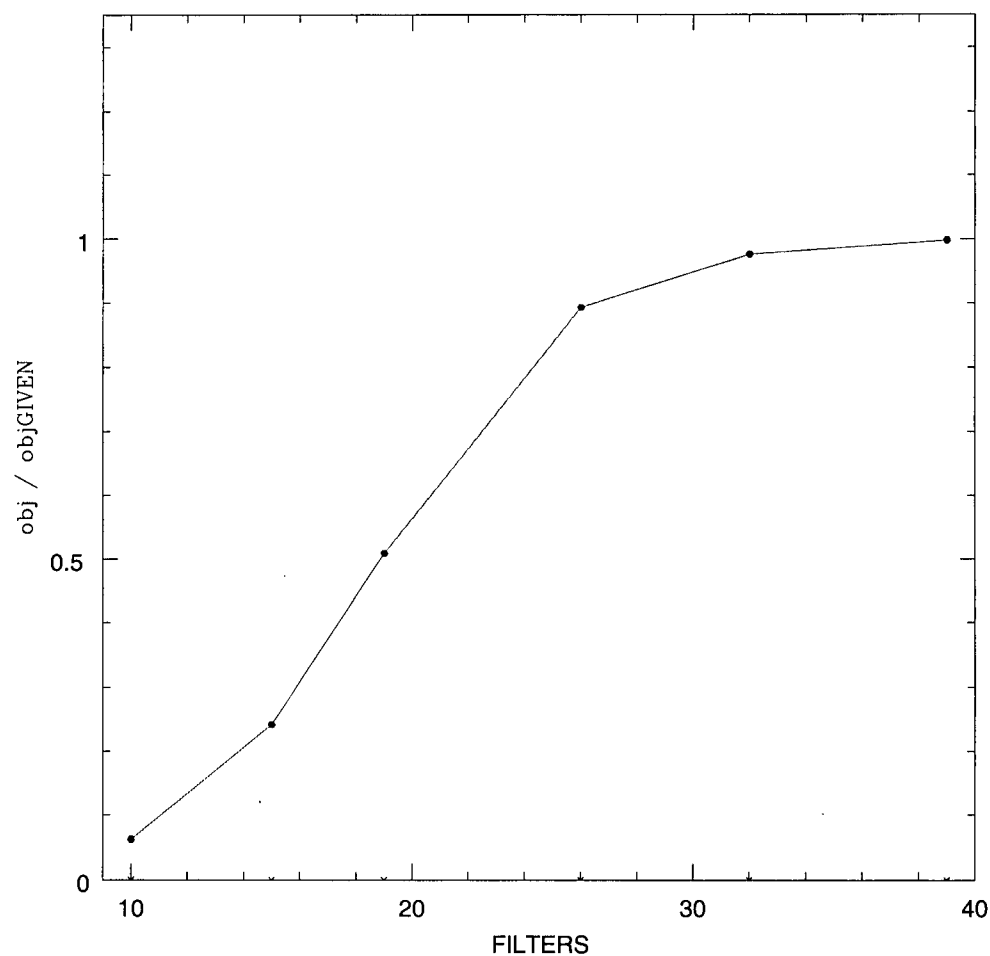


Figure 4.33: Normalized distribution in the redshift range $z=4.1-7$ for correctly classified quasars (hexagon) and for objects wrongly classified as quasars (cross).

interesting consideration is that the black line, which represents the number of sources misclassified as quasars, does not appear in any plot for quasars.

This means that when a test object is classified as quasar, it is really so. We can conclude that in order to have at least 80% of well classified quasars, the method should be applied only to sources with 30 or more magnitudes. The situation is improved for galaxies: in this case the threshold is closer to 20 magnitudes.

To confirm the validity of this criterion, fig. 4.34-4.39 show the distribution of the odds ratio's logarithm normalized to the one from the correct category and calculated with 39 filters, for 4 quasars and 2 galaxies at different redshift (black line).

The odds ratio can be used to determine which of two models is the preferred one considering the ratio of their probabilities. In each plot, the black line represents the odds ratio distribution in favour of the correct category, and the red, green and blue lines are the odds ratio distributions in favour of quasar, star and galaxy models as the best fit of the template-object analysed. When a line exceeds the other ones in a plot, the related category of models is the preferred one. For quasar test objects, in most cases the odds ratio in favour of stars and galaxies (wrong classification) is lower than the one in favour of quasars (correct classification) for more than 25 filters at least. For galaxies fewer filters are required to avoid an eventual misclassification: it is reasonable to expect that only 20 filters are required.

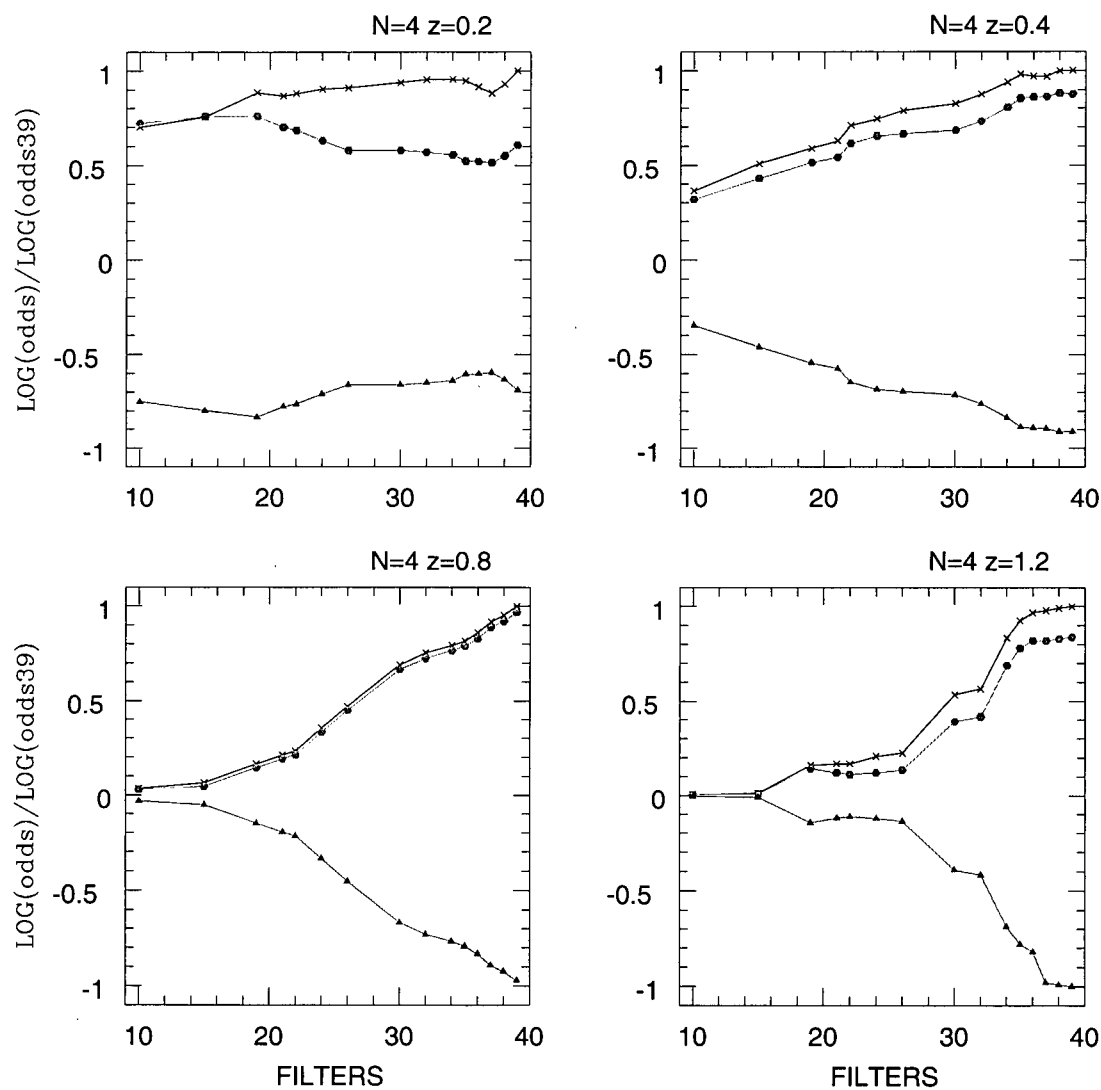


Figure 4.34: Normalized odds ratio distribution for a Sa spiral galaxy (N.4) at redshift 0.2, 0.6, 0.8 and 1.2 in favor of stellar (hexagon), galactic (cross) and quasar (triangle) template.

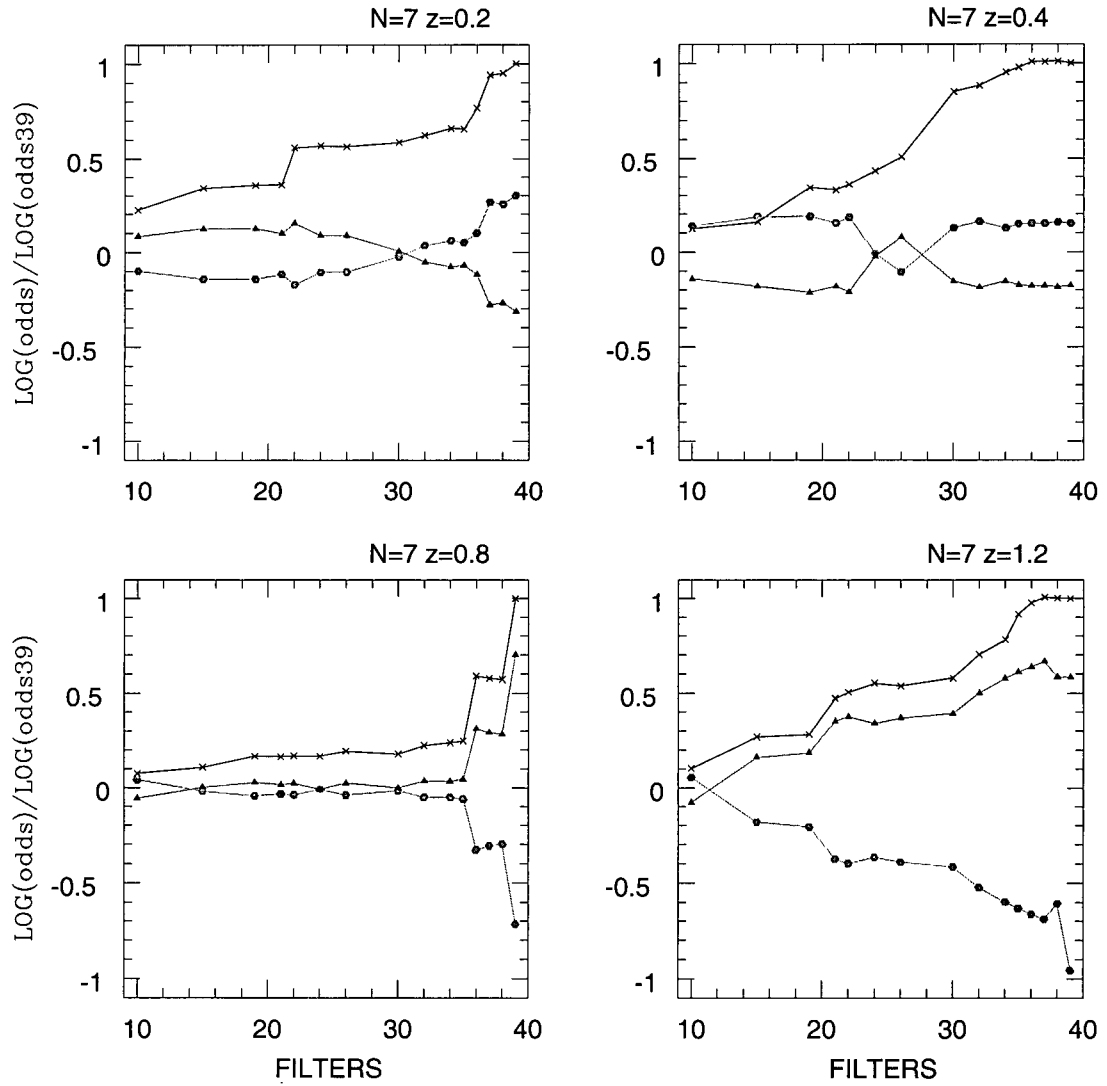


Figure 4.35: Normalized odds ratio distribution for a starburst galaxy (N.7) at redshift 0.2, 0.6, 0.8 and 1.2. in favour of stellar (hexagon), galactic (cross) and quasar (triangle) template.

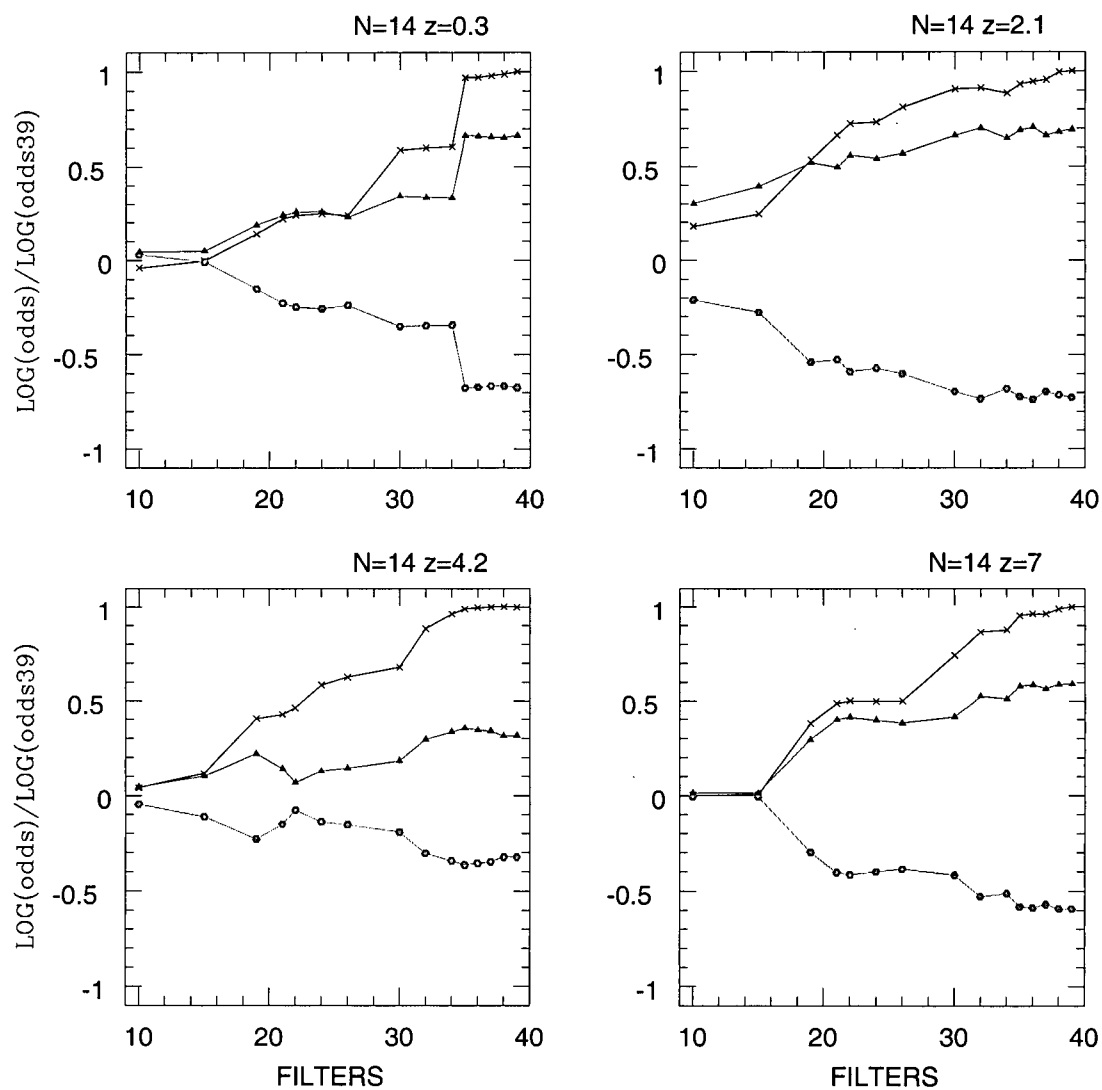


Figure 4.36: Normalized odds ratio distribution for QSO N.14 at redshift 0.3, 2.1, 4.2 and 7. in favour of stellar (hexagon), galactic (triangle) and quasar (cross) template.

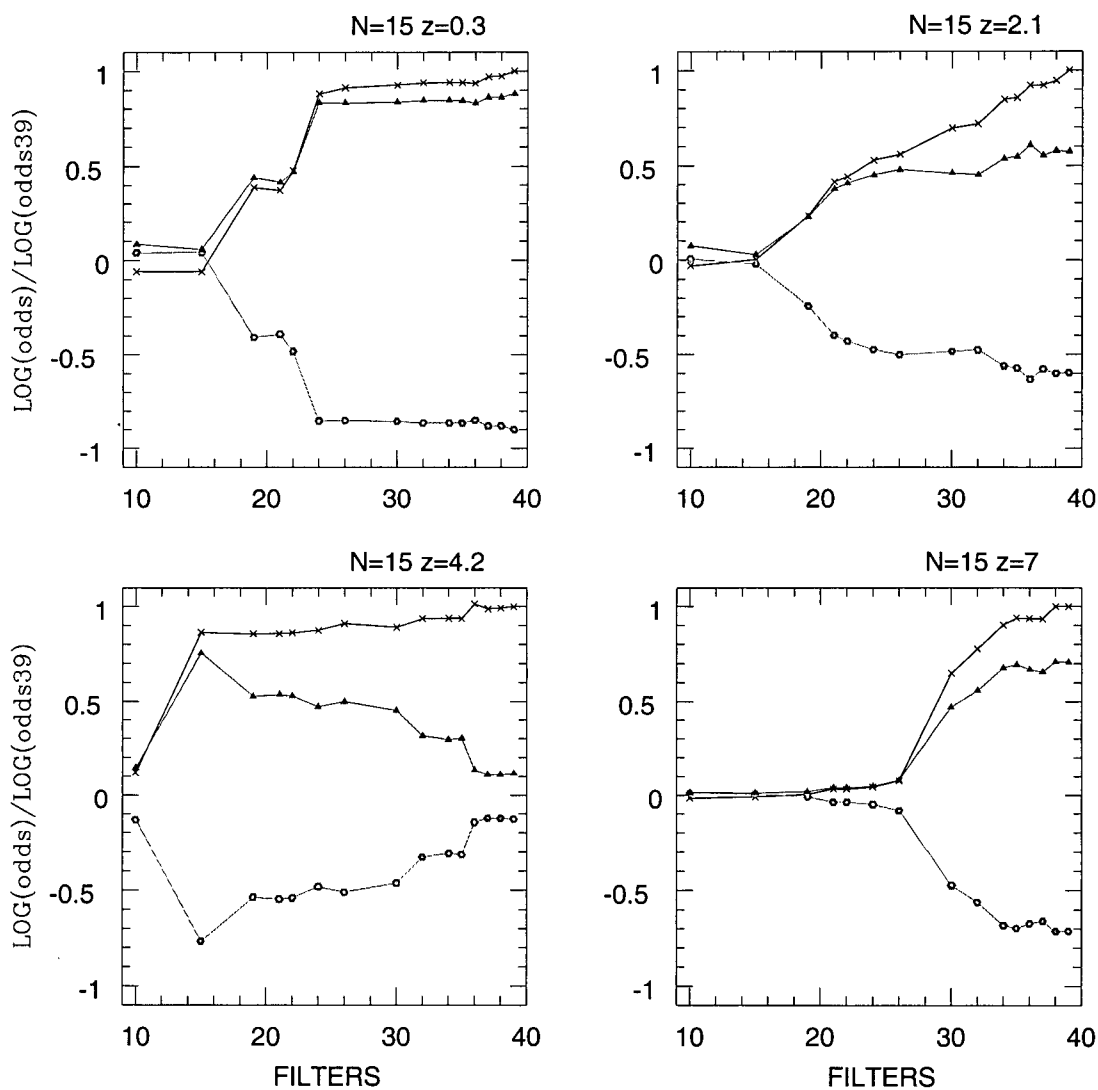


Figure 4.37: Normalized odds ratio distribution for QSO N.15 at redshift 0.3, 2.1, 4.2 and 7. in favour of stellar (hexagon), galactic (triangle) and quasar (cross) template.

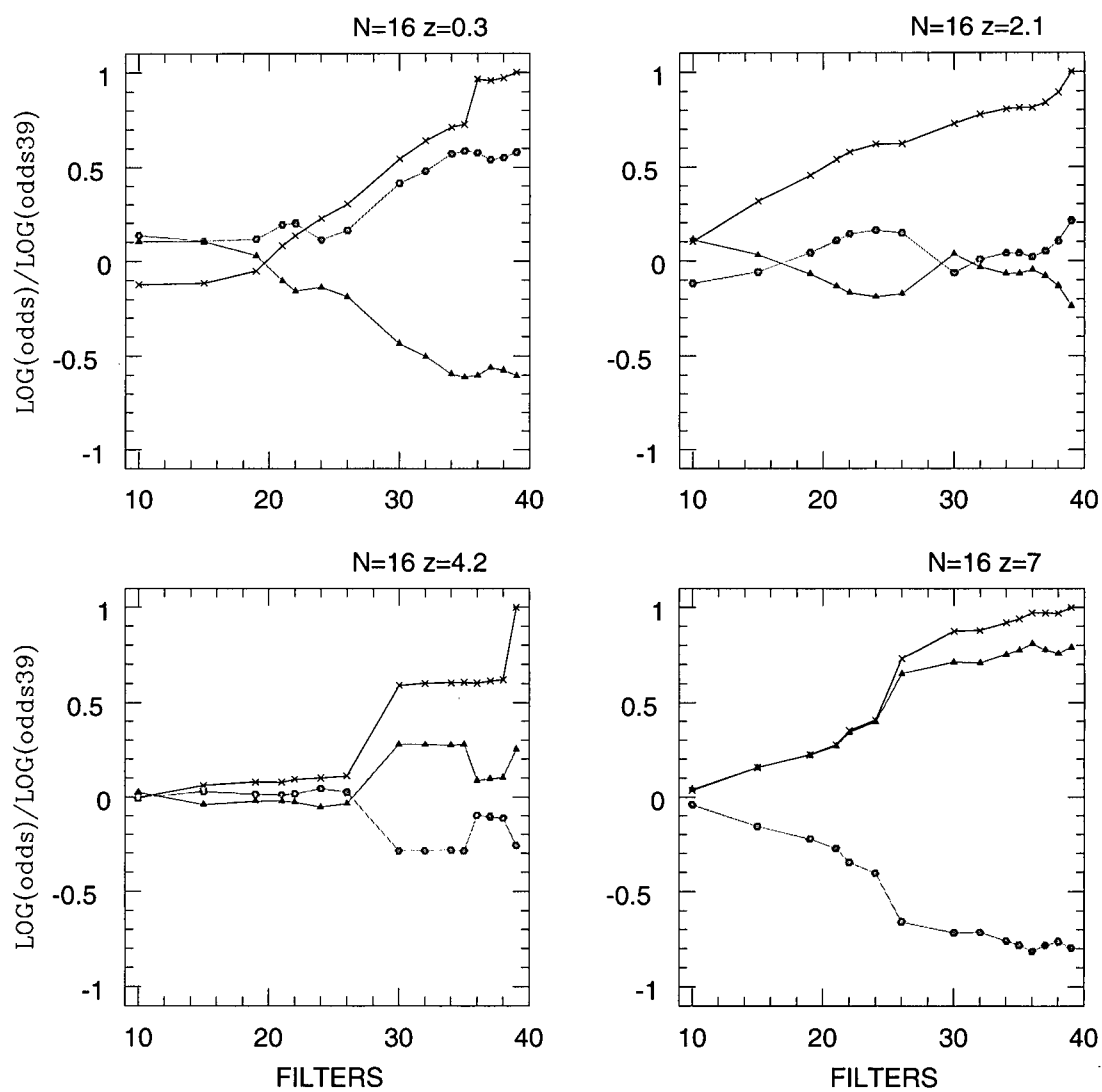


Figure 4.38: Normalized odds ratio distribution for QSO N.16 at redshift 0.3, 2.1, 4.2 and 7. in favour of stellar (hexagon), galactic (triangle) and quasar (cross) template.

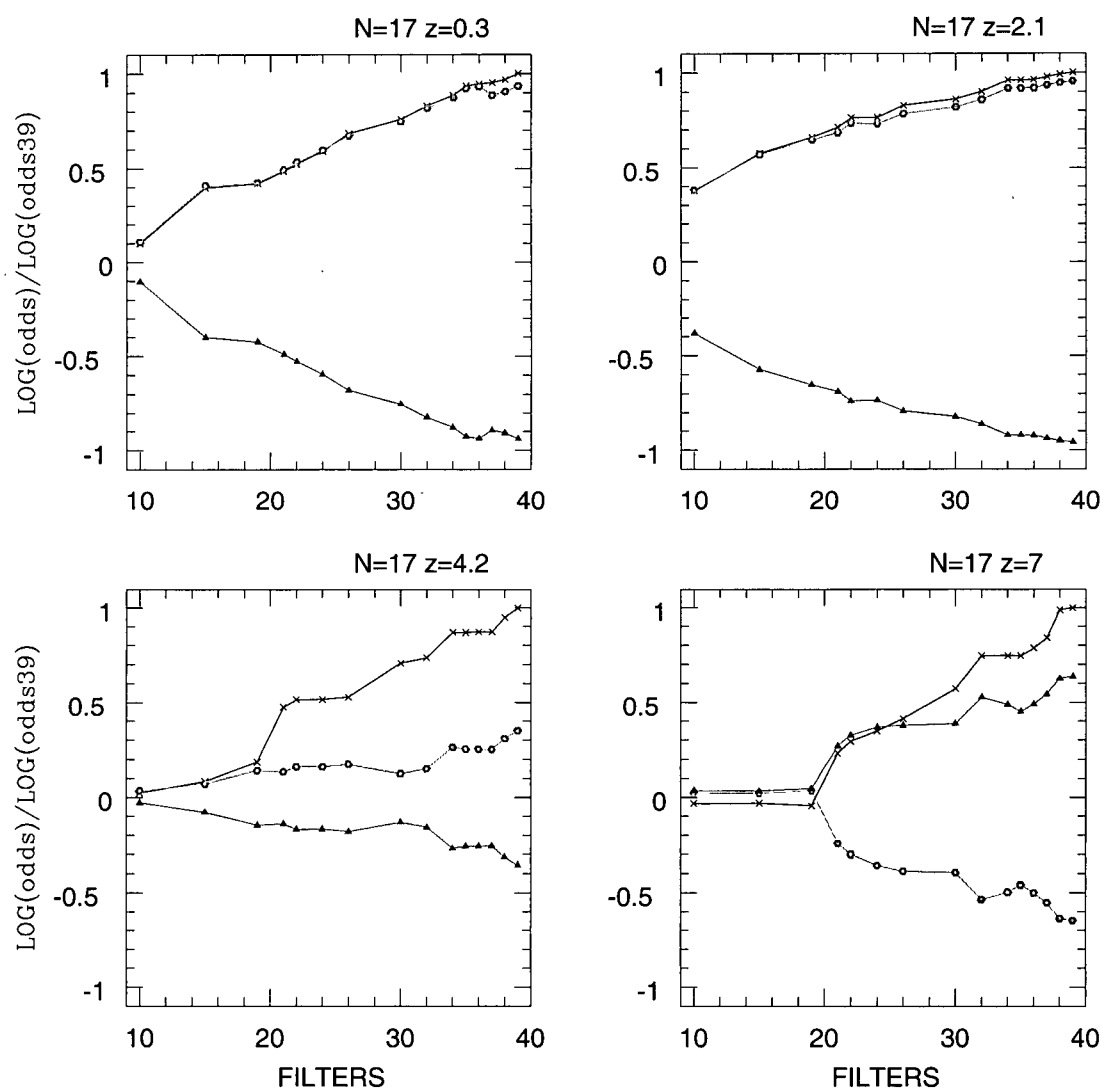


Figure 4.39: Normalized odds ratio distribution for QSO N.17 at redshift 0.3, 2.1, 4.2 and 7. in favour of stellar (hexagon), galactic (triangle) and quasar (cross) template.

CHAPTER 5

QUASARS IN THE UNMS1 CATALOG.

5.1 Results.

As shown in the previous chapter, QSOs can be found and identified with a completeness of $\sim 85\%$ when the method described in §4 is applied to the UNMS1 catalog for objects satisfying two criteria: a minimum number of 30 flux measurements and a minimum separation radius of 3 arcsecs. Based on these criteria, our algorithm selects 39040 sources out of the 20.13-deg^2 field.

Table 5.1 summarizes the number of objects.

Category	#
STARS	25193
GALAXIES	10791
QUASARS	3056

Table 5.1: Star, galaxy and quasar identifications.

We first describe star and galaxy candidates; quasar candidates will be discussed in §5.2.

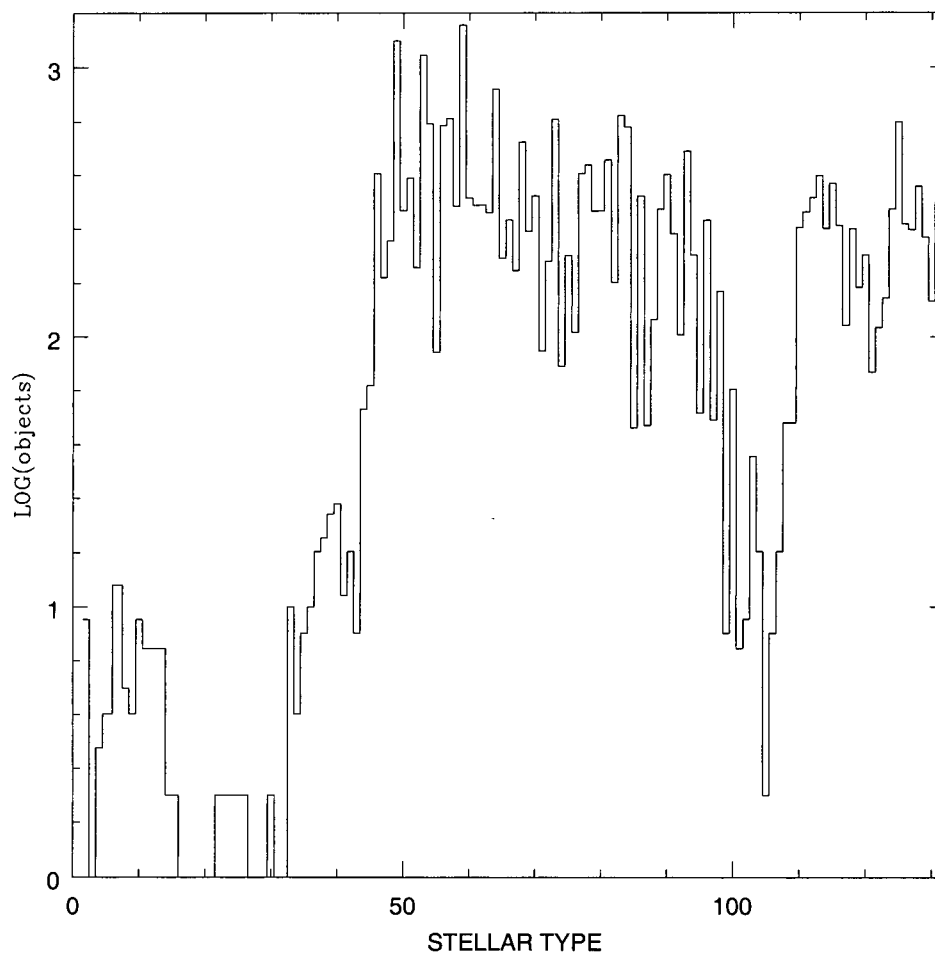


Figure 5.1: Star counts by spectral types.

5.1.1.1 Stellar candidates in the UNMS survey.

Fig. 5.1 shows the distribution of stars, organized according to the order presented in Table 5.2.

Two major structures appear: from the 46th to the 99th stellar type and

from the 108th to the 131th stellar type. The first group corresponds to F, G, K and M stars of any luminosity class; the second group correspond to metal-weak and metal-rich F, G, K and M stars, mainly main sequence and giant stars. The most common templates are main sequence G stars and giant G stars.

A and B stars (1-32) and O stars (105-108) represent just a small fraction of the stellar distribution. This result is in agreement with the star counts by spectral type commonly known. Table 5.3 shows the number density logarithm of stars [$\# / 10^4 pc^3$] by spectral types from data published in Allen (1973) [6] [1]: for every luminosity class, F-G-K-M stars are the most frequent.

Table 5.4 is similar to Table 5.3 but shows the results from the LMT survey: it is useful to see if the method can recognize stars not only of different type but also of different luminosity classes. The comparison of these two tables confirms that the method separate stars of different stellar types: many F, G, k and M stars are found with respect to other types; the only discrepancy is in large offsets of O stars in the LMT sample. The star distribution according to the luminosity class, is not good: the number of giants and supergiants is too high with respect to that of main sequence stars.

5.1.2 Galaxy candidates in the UNMS survey.

Fig. 5.2 shows the galaxy counts by morphological type according to the order described in Table 5.5: the term “Bulge” refers to galaxies with a pronounced bulge (spheroidal central region); the term “SB” refers to starburst

NUM.	TYPE	NUM.	TYPE	NUM.	TYPE	NUM.	TYPE
1	a0i	34	f0i	67	k0iv	100	m5v
2	a0iii	35	f0ii	68	k0v	101	m6iii
3	a0iv	36	f0iii	69	k1iii	102	m6v
4	a0v	37	f0v	70	k1iv	103	m7iii
5	a2i	38	f2ii	71	k2i	104	m8iii
6	a2v	39	f2iii	72	k2iii	105	m9iii
7	a3iii	40	f2v	73	k2v	106	o5v
8	a3v	41	f5i	74	k34ii	107	o8iii
9	a47iv	42	f5iii	75	k3i	108	o9v
10	a5iii	43	f5iv	76	k3iii	109	rf6v
11	a5v	44	f5v	77	k3iv	110	rf8v
12	a7iii	45	f6v	78	k3v	111	rg0v
13	a7v	46	f8i	79	k4i	112	rg5iii
14	b0i	47	f8iv	80	k4iii	113	rg5v
15	b0v	48	f8v	81	k4v	114	rk0iii
16	b12iii	49	g0i	82	k5iii	115	rk0v
17	b1i	50	g0iii	83	k5v	116	rk1iii
18	b1v	51	g0iv	84	k7v	117	rk2iii
19	b2ii	52	g0v	85	m0iii	118	rk3iii
20	b2iv	53	g2i	86	m0v	119	rk4iii
21	b3i	54	g2iv	87	m10iii	120	rk5iii
22	b3iii	55	g2v	88	m1iii	121	wf5v
23	b3v	56	g5i	89	m1v	122	wf8v

Table 5.2: Continue.

NUM.	TYPE	NUM.	TYPE	NUM.	TYPE	NUM.	TYPE
24	b57v	57	g5ii	90	m2.5v	123	wg0v
25	b5i	58	g5iii	91	m2i	124	wg5iii
26	b5ii	59	g5iv	92	m2iii	125	wg5v
27	b5iii	60	g5v	93	m2v	126	wg8iii
28	b6iv	61	g8i	94	m3ii	127	wk0iii
29	b8i	62	g8iii	95	m3iii	128	wk1iii
30	b8v	63	g8iv	96	m3v	129	wk2iii
31	b9iii	64	g8v	97	m4iii	130	wk3iii
32	b9v	65	k01ii	98	m4v	131	wk4iii
33	f02iv	66	k0iii	99	m5iii		

Table 5.2: Conversion table between stellar type and number.

	O	B	A	F	G	K	M
Giants and Supergiants				-0.3	0.2	0.6	-0.6
Main Sequence	-3.6	0.0	0.7	1.4	1.8	2.0	2.8

Table 5.3: Logarithmic star counts [$\# / 10^4 pc^3$] by stellar type and luminosity class from data published in Allen (1973) [1].

galaxies of different types as shown in Table 4.5.

Each histogram bin in Fig. 5.2 includes galaxies of the same type integrated over all redshifts (the redshift ranges from 0 to 1.2, with step $\delta z = 0.01$). There are three pronounced peaks which correspond to S0 and Sc galaxies, and starburst galaxies. As explained later, the fact to have many

	O	B	A	F	G	K	M
Giants and Supergiants				1.9	3	2.9	2.1
Main Sequence	1.0	0.0	0.64	2.2	2.8	2.9	2.6

Table 5.4: Logarithmic star counts [$\# / 10^4 pc^3$] for candidates found in the LMT survey.

NUM.	TYPE	NUM.	TYPE	NUM.	TYPE
1	Bulge	6	Sc	11	SB 5
2	E	7	SB 1	12	SB 6
3	S0	8	SB 2	13	UVhot
4	Sa	9	SB 3		
5	Sb	10	SB 4		

Table 5.5: Conversion table between galaxy type and number.

spirals is reasonable if compared with other works on galactic types [6].

It is useful to check the galaxy distribution with that found in the CfA1-2 Redshift Surveys [50]. The CfA1 sample includes 2397 galaxies (ellipticals, S0, Sa, Sb, Sc, Sd and Sm spirals, Irregular galaxies) distributed over 2.7 steradians; the CfA2 survey has 1862 galaxies over 0.42 steradians. Table 5.6 shows the galaxy percentage distributed according to the morphological type for CfA1-2 and LMT surveys. Discrepancies between the CfA1 and CfA2 surveys are due to the fact they sample different structures: the morphological mix varies with local density [19]. For the UNMS survey, the fraction of Sc galaxies does not include Sd spirals.

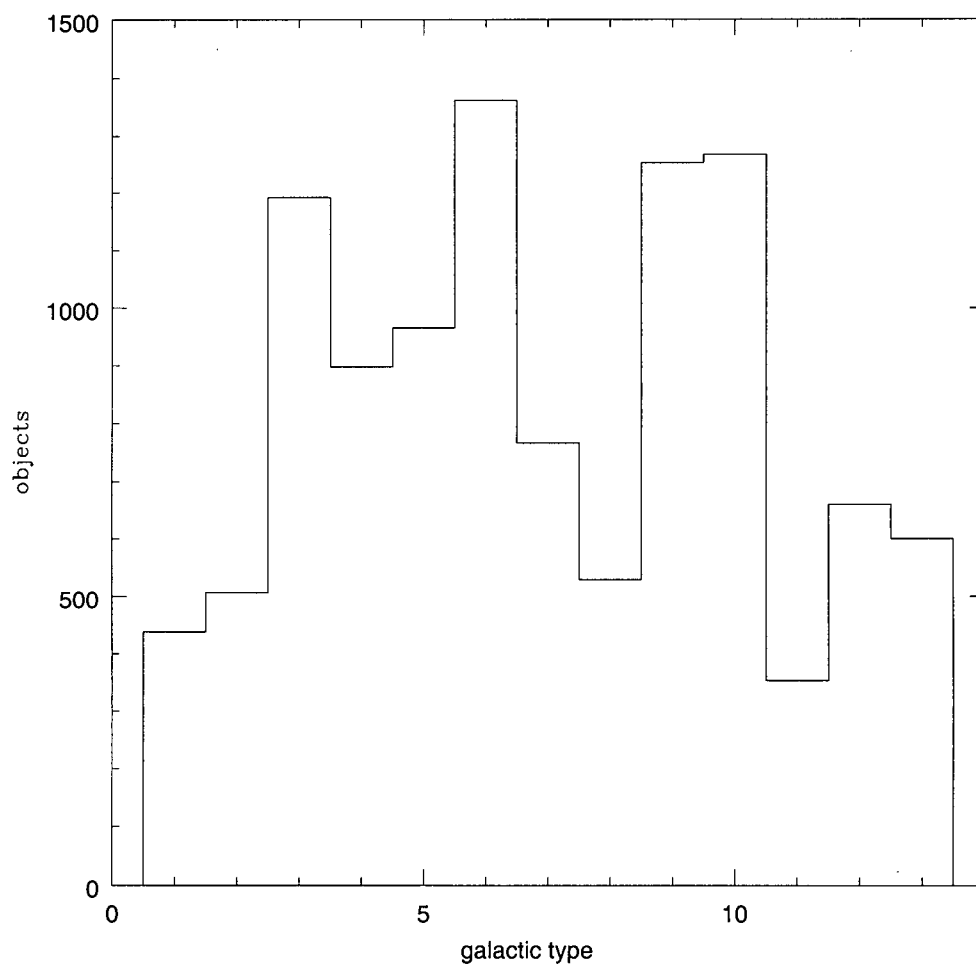


Figure 5.2: Galaxy distribution by the morphological type.

Considering only common galactic types, what appears evident in each survey is the low fraction of ellipticals: at this point, this result seems reasonable.

The major discrepancy is the smaller number of spiral candidates found

	CfA1	CfA2	LMT
	%	%	%
bulge	4.1
E	11.1	5.3	4.7
S0	25.3	34.4	11
Sa+sb	33.2	40.3	17.3
Sc+Sd	22.1	12.9	12.6
Sm+Im	25.3	5.1
SB1-6	38.6
UVhot	6.1

Table 5.6: Fraction of ellipticals (E), S0 galaxies, Sa+Sb, Sc+Sd and Sm spirals, Irregular (Im) galaxies, Starburst (SB1-6) and UVhot galaxies in the CfA1, CfA2 and LMT galaxy samples.

in the LMT sample: this spiral fraction is not in fact completely consistent with the luminosity function of Binggeli, Sandage and Tammann [5] where, considering the galaxy distribution in the local field, the fraction of spirals with respect to ellipticals seems higher than that obtained using the method described in §4.

Among galaxy candidates, there is a big number of starbursts with respect to normal galaxies. This third result doesn't agree with the luminosity function of Sanders & Mirabel (Fig. 1) [2]: for bolometric luminosity lower than $10^{11} L_{\odot}$, the luminosity function of normal galaxies is well above that of starbursts; for higher luminosities, it seems there are more irregular galaxies than normal galaxies but the trend of starburst luminosity function is not

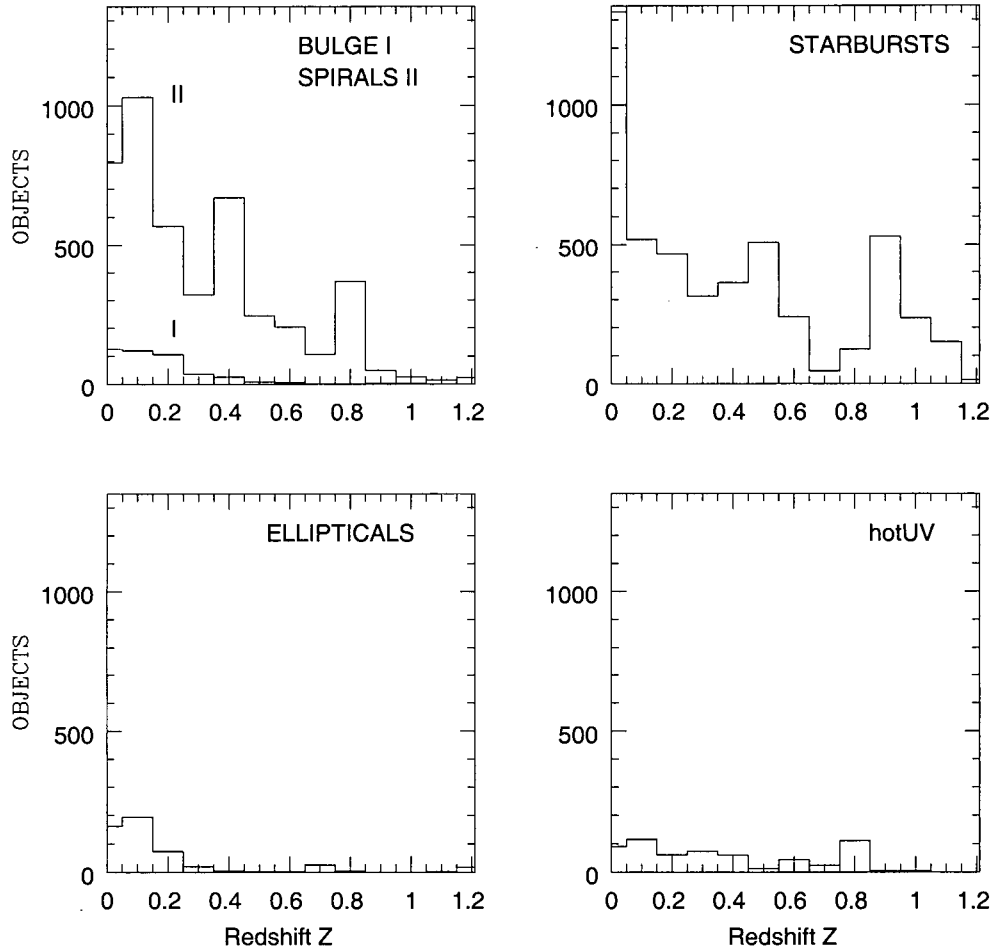


Figure 5.3: Distribution of galaxy counts with spectral type and redshift.

well defined. Since starbursts are characterized by a great stellar activity and their spectrum show emission lines, it is possible that some stars were misidentified as starburts.

Fig. 5.3 shows the galaxy distribution in redshift according to the galactic

type. Ellipticals are more concentrated at low redshifts: this is a selection effect due to the difficulty to observe non-emission like objects at high redshifts.

Spirals are mainly found in the range $z = 0-0.6$: this is consistent with the fact that, though dwarf spheroidal ellipticals are the closest galaxies to the Milky Way, they are not as easily detected as spirals, the most luminous field galaxies close to our Galaxy.

Starburst candidates are detected at all redshifts: although they are mainly concentrated in the range $z = 0 - 0.3$, there are pronounced peaks at $z \sim 0.5$ and $z \sim 0.9$. Many of the features such as tails and ringlike structures visible in starburst pictures can be convincingly explained in terms of colliding and/or merging galaxies [67]. The fact that galaxies need time to form and, first of all, to come so close to the point to interact, could explain the great number of starbursts found at low redshift. Another explanation for the peak in the range $z = 0 - 0.3$ could be that some of these local starbursts are misidentified stars.

5.2 Properties of quasar candidates.

5.2.1 The number - redshift distribution.

Fig. 5.4 shows the number of quasar candidates in each redshift range $\delta z = 0.3$, from $z = 0.3$ to $z = 7.0$. Most sources fall in two regions: $0.5 - 1.5$ and $3.5 - 5.5$.

It is useful to check this result with other redshift distributions such as the Hewett & Burbidge catalog (7110 quasars) [35] and the Sloan Sky

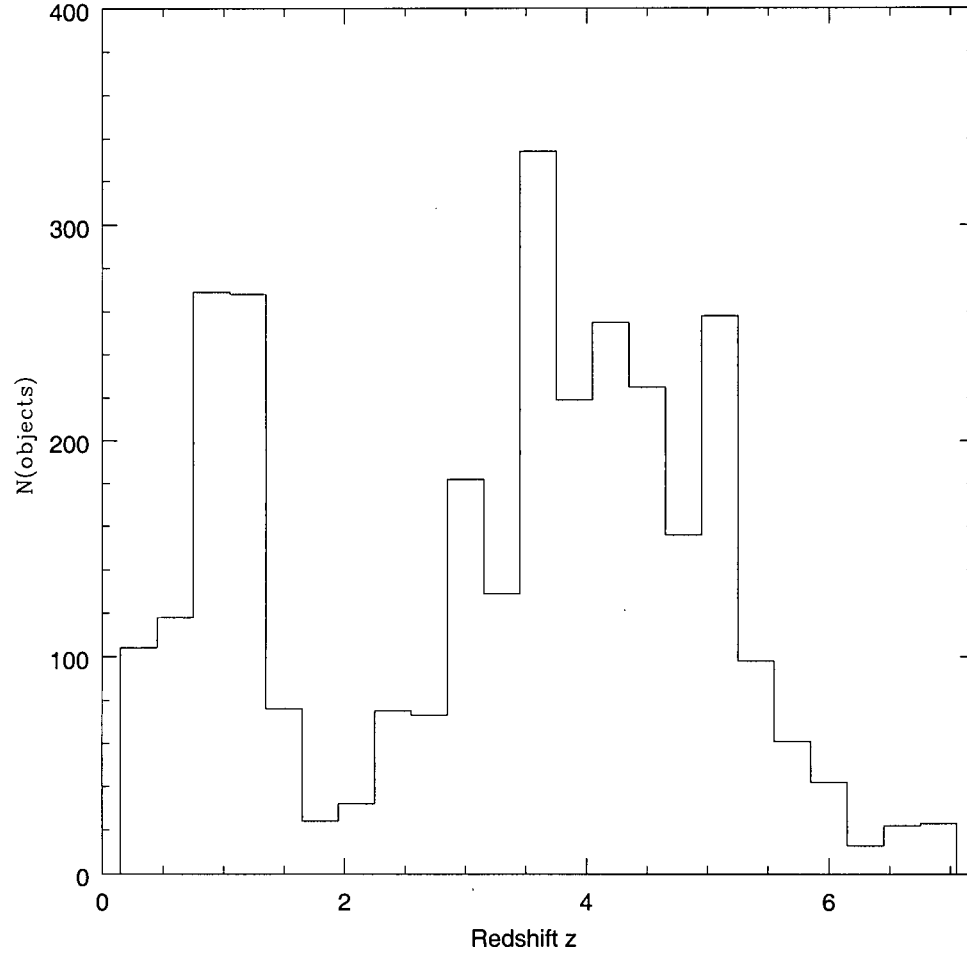


Figure 5.4: Redshift distribution of quasar candidates.

Survey catalog (3814 quasars) [66] (see Fig. 5.5). In the first work, quasars are mostly concentrated in the range 0 - 2.3 with a tail extending up to $z = 4$. The second study shows many quasars in the range 0.25 - 2 but there are still objects at $z = 5$. In this last case, the peak at $z \sim 0.25$ is caused by

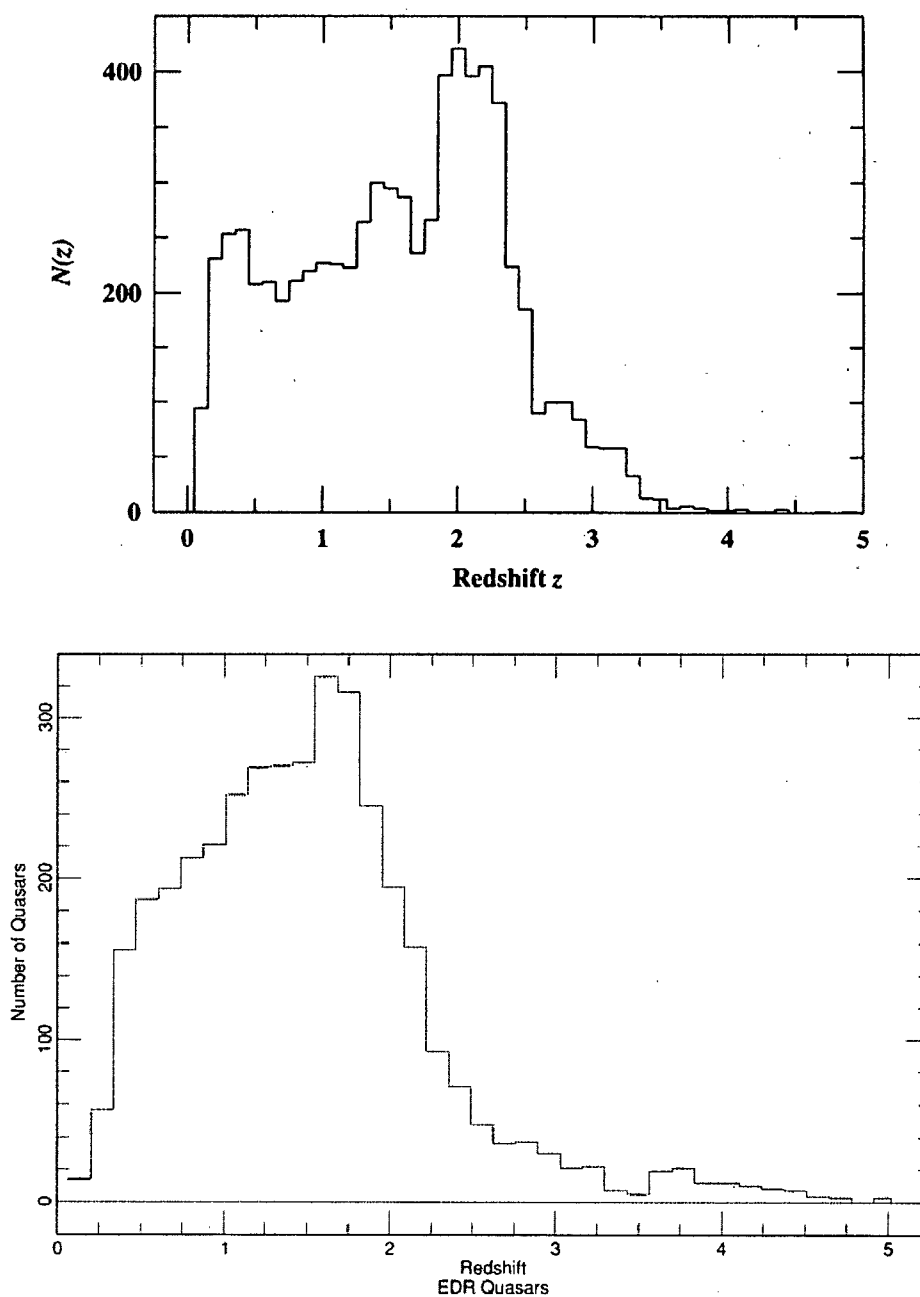


Figure 5.5: The redshift distribution for quasars in the Hewett&Burbidge catalog (top) and in the Sloan Sky Survey catalog (bottom).

Seyfert galaxies.

Comparing all these distributions, two discrepancies can be noted: the LMT sample shows a dirth of detections for $z \sim 2$ and an unusual number of objects at redshift $z > 4$. The Ly α emission line could explain both these two effects. At $z \sim 2$ the Ly α is not visible in the optical part and this, besides having an incomplete SED, could contribute to the misclassification of some quasars as stars: this could be the reason behind the first discrepancy. The second effect could be explained in the following way: the Ly α emission line enters into the optical spectrum (e.i. it can be observed in quasar templates at wavelengths $\lambda > 4500 \text{ \AA}$) at redshift higher than 3. If a galaxy spectrum or, more likely a stellar spectrum, shows a strong line but it misses other important flux measurements, this source can be misclassified as quasar.

This misclassification was in part expected: the method is supposed to separate quasars from galaxies and stars with an accuracy of 85%. Since a lot more than 15% quasars seem misidentified, it is then necessary to analyse more carefully the quasar sample in order to catch unlikely quasar candidates.

5.2.2 The number - apparent V magnitude distribution.

Fig. 5.6 shows the object distribution according to the apparent V magnitude: quasar candidates are peaked around magnitude 19, with a long and thick tail extending to magnitude 12.

Even though the brightest quasar (3C 273, <http://www.seds.org/~spider/spider/Misc/3c273>.) has a visual brightness 12.8, it is unlikely that all the objects brighter than magnitude 16 are correctly classified.

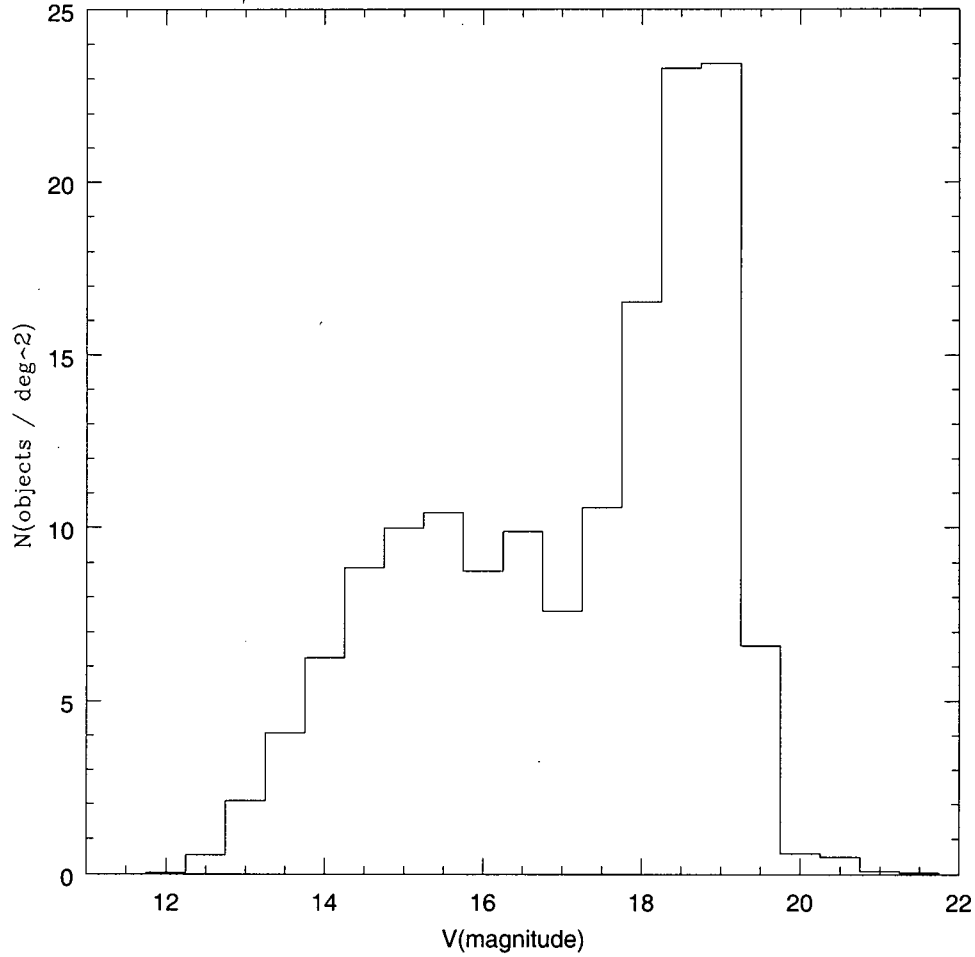


Figure 5.6: The V magnitude distribution for quasar candidates.

The magnitude distribution is compared to that of Hewett & Burbidge (Fig. 5.7): both distributions show a pronounced peak at magnitude 19 and the fact our sample misses many faint objects at $V > 20$ could be due to the lower limiting magnitude reached by the NODO-LMT (21 mag) and also

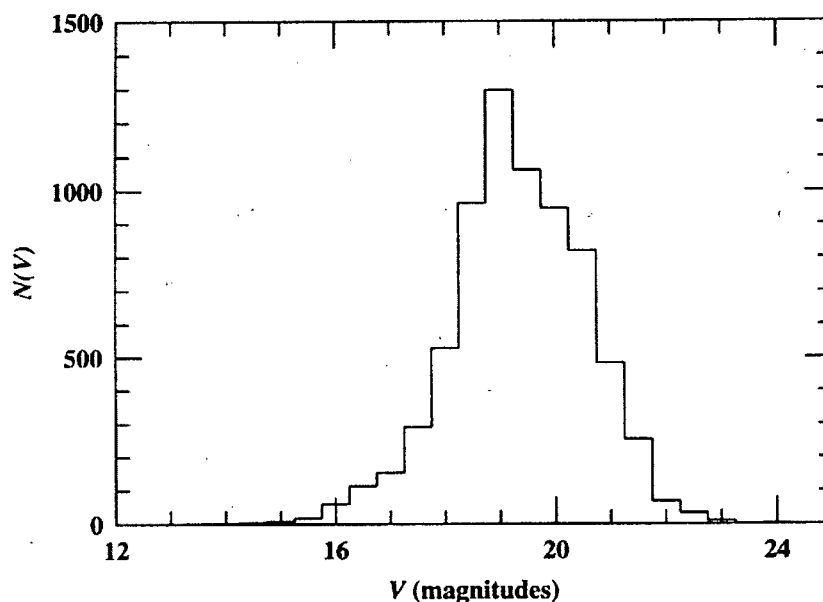


Figure 5.7: The V magnitude distribution from the Hewett&Burbidge catalog.

to the smaller number of quasar candidates counted in the UNMS1 sample (30% of that of Hewett & Burbidge). The real discrepancy between these two distributions is the bigger number of bright sources in the LMT sample: it is possible that many quasar candidates with magnitude brighter than 16 are misclassified stars.

5.2.3 The number - spectral index α distribution.

The continuum part of a quasar spectrum can be modeled by a simple power law $F_\nu \propto \nu^\alpha$, where F_ν is the flux in frequency and α is the spectral index.

To determine the continuum, one must exclude emission lines. This is done in steps. First, the SED is fitted with a power law considering all magnitudes. Second, all the points for which

$$|F_{obs,\nu} - \beta\nu^\alpha| > 2\delta F_{obs,\nu} \quad (5.1)$$

are rejected as possible lines. Here $F_{obs,\nu}$ and $\delta F_{obs,\nu}$ are the observed flux and its error at frequency ν , α and β are the characteristic parameters of the best power law fit. The third and final step is to fit a second time the SED with the restricted set of magnitudes.

Fig. 5.8 shows the object distribution according to the spectral index α . A prominent peak at $\alpha \sim -1$ and a second peak for $\alpha \sim -2$ are the most interesting characteristics.

Fig. 5.9 shows spectral index distributions by Warren et al. [77] and by Francis et al. [24]. The first study is a multicolour survey for high redshift quasars and it includes 144 sources; the second work uses quasars taken from the Large Bright Quasar Survey to create a high signal-to-noise composite spectrum (718 sources). Both of them show a peak around $\alpha \sim -0.5$, a bit shifted from the peak at $\alpha \sim -1$ observed in this survey. The main difference between the UNMS α distribution and those found in these works is the second peak, centered at $\alpha \sim -2$ and extending up to $\alpha \sim -5$. Since typical values of α cited in literature (§4.3.3) are in the range $[-2.5, 1]$, it is likely that some misclassified stars are included in this second peak, but it is also possible that the elimination of some points (no more than 9 points according to the criterion used) in spectra has contributed to make quasar SEDs steeper if the flux measurements eliminated are at the edges of the optical range.

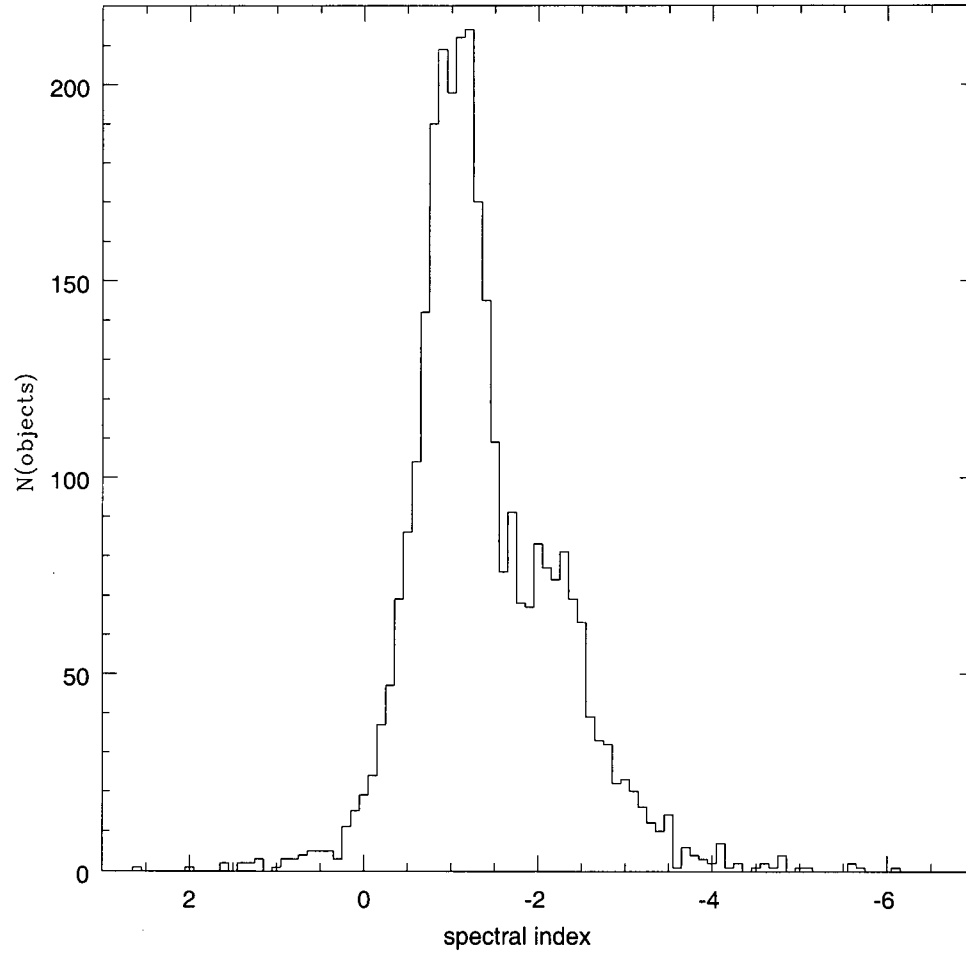


Figure 5.8: Spectral index distribution for quasar candidates in the UNMS1 catalog.

5.3 Discussion.

In §4 we found that it is possible to identify quasars with a completeness of 85%. Yet, result diagrams, shown in the previous section, are not fully

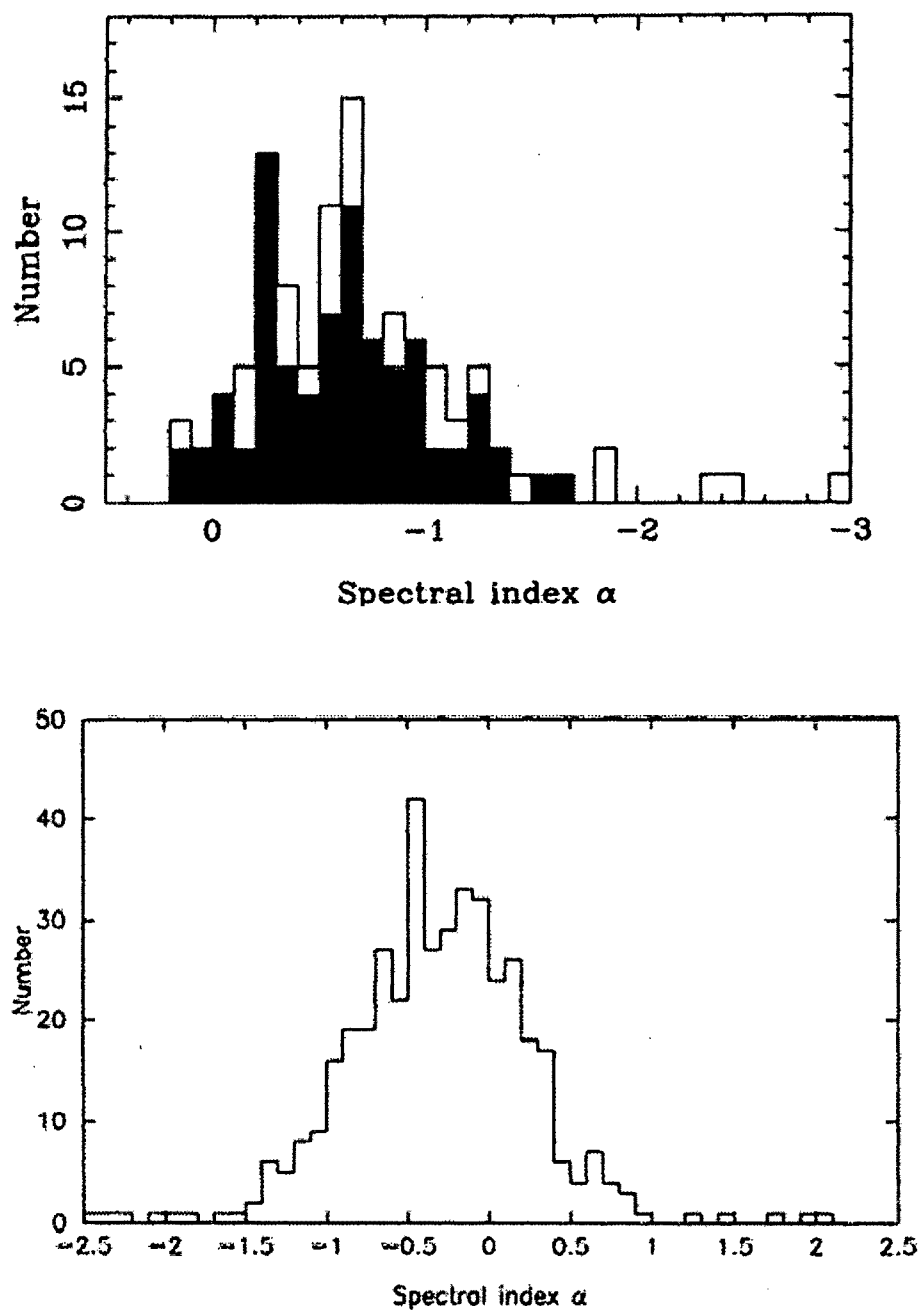


Figure 5.9: The spectral index distribution by Warren et al. (top picture, upper line) and by Francis et al. (bottom).

consistent with the results obtained from other surveys. Therefore, objects outside expected ranges of redshift $[0.5, 4]$, magnitude $[16, 23]$ and spectral index $[-3, 1]$ were analysed more completely.

To do that, three more diagrams were considered: object distribution in the redshift - V magnitude plane (Fig. 5.10), in the redshift - spectral index plane (Fig. 5.11) and in the spectral index - V magnitude plane (Fig. 5.12).

Fig. 5.10 shows that, faint sources are equally distributed at high and low redshifts, but quasar candidates brighter than the 16th magnitude are mostly localized in the redshift range 3-6. This last result is not acceptable because those quasars would have to have exceptionally high luminosities.

The second diagram (Fig. 5.11) shows that sources are mainly grouped around $\alpha \sim -1$. Most of those having spectral index lower than -3, have redshift higher than 4. They represent just a small group (78 sources) and neglecting them would have little effect.

The next diagram (Fig. 5.12) shows the source distribution in the spectral index - V magnitude plane: only few of the bright objects have unusual spectral indexes lower than -3.

These considerations suggest that, in order to reduce misclassification, criteria should be based on the first diagram (Fig. 5.10). Though we wish to eliminate objects that satisfy one or more of the following criteria:

- $V \text{ mag} < 16$ and $z > 3.5$;
- $V \text{ mag} < 16$ and $\alpha < -3$;
- $z > 3.5$ and $\alpha < -3$.

The fact that we chose $\alpha = -3$ as the minimum value for the spectral index

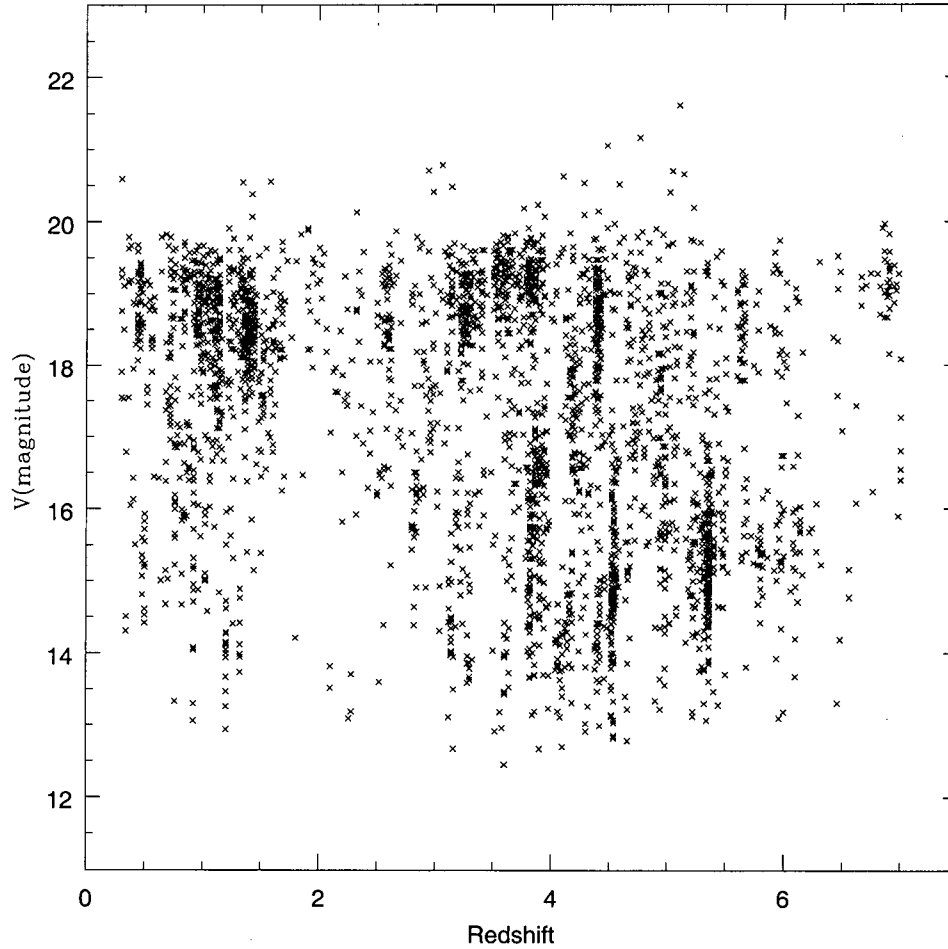


Figure 5.10: Quasar candidates in the redshift - V magnitude plane.

instead of -2.5, cited in §5.2.3, is justified by the desire to retain as good quasar candidates as possible. Each object has a minimum number of 30 flux measurements over a total of 39: if an observed SED shows the flux of an emission line and no flux in the filters right beside it, the continuum part of

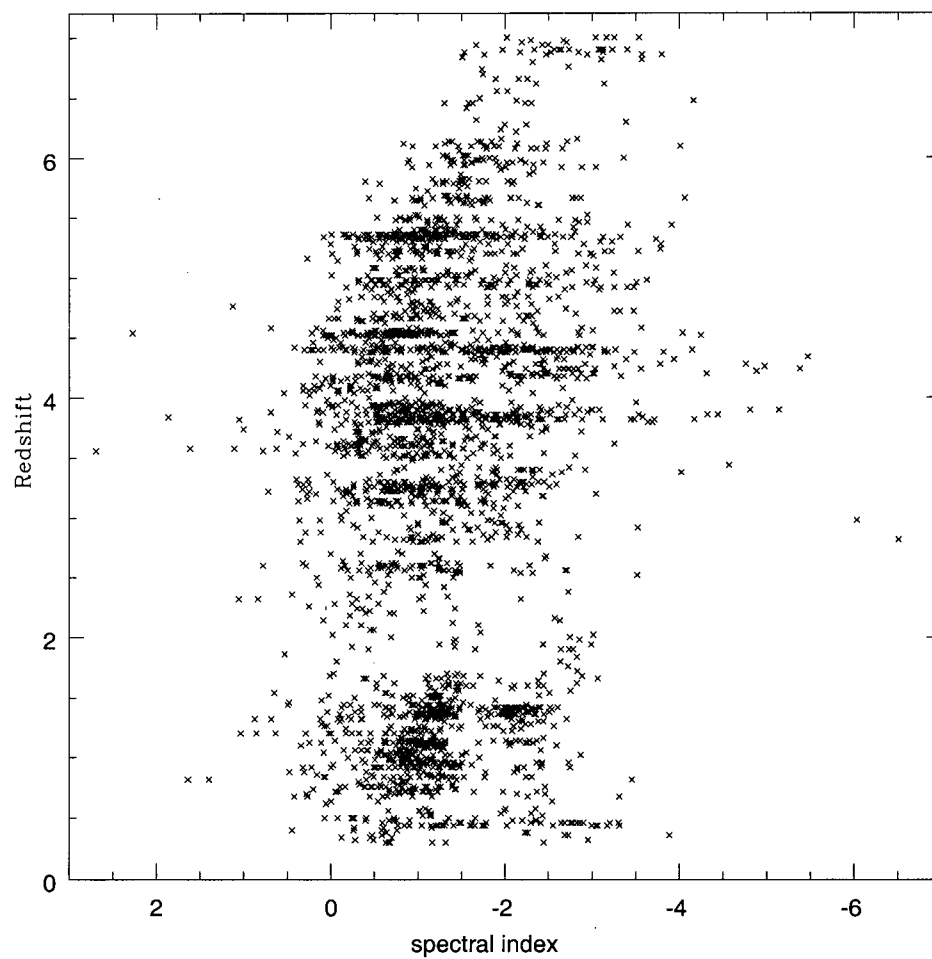


Figure 5.11: Quasar candidates in the redshift - spectral index plane.

the spectrum would appear steeper ($\alpha < -2.5$).

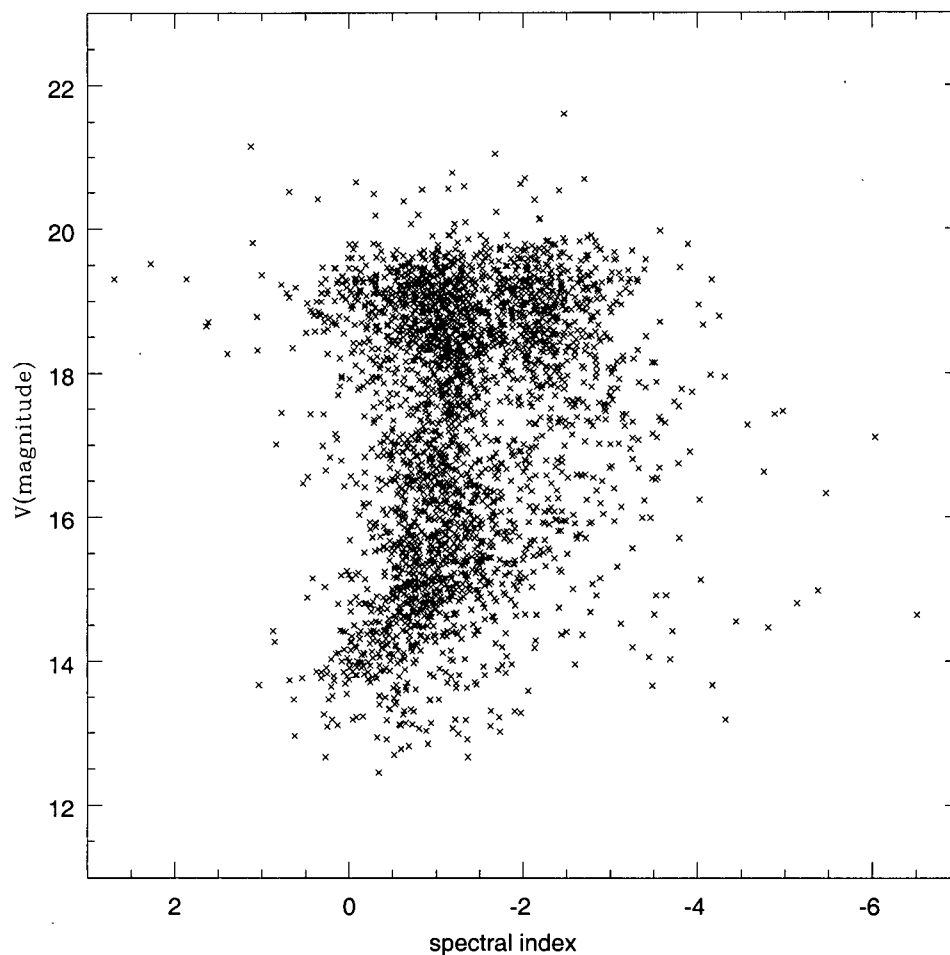


Figure 5.12: Quasar candidates in the spectral index - V magnitude plane.

5.4 Quasar candidates.

Weeding out misclassified quasar candidates which satisfy at least one of the criteria mentioned above, the final list now includes 2294 objects, 6% of the entire group of sources analysed with this method.

According to the surface densities mentioned in §4, the distribution of stars, galaxies and quasars should be respectively 49.5%, 49.5% and 1% of the object sample: it is clear that the number of quasars found is still higher than

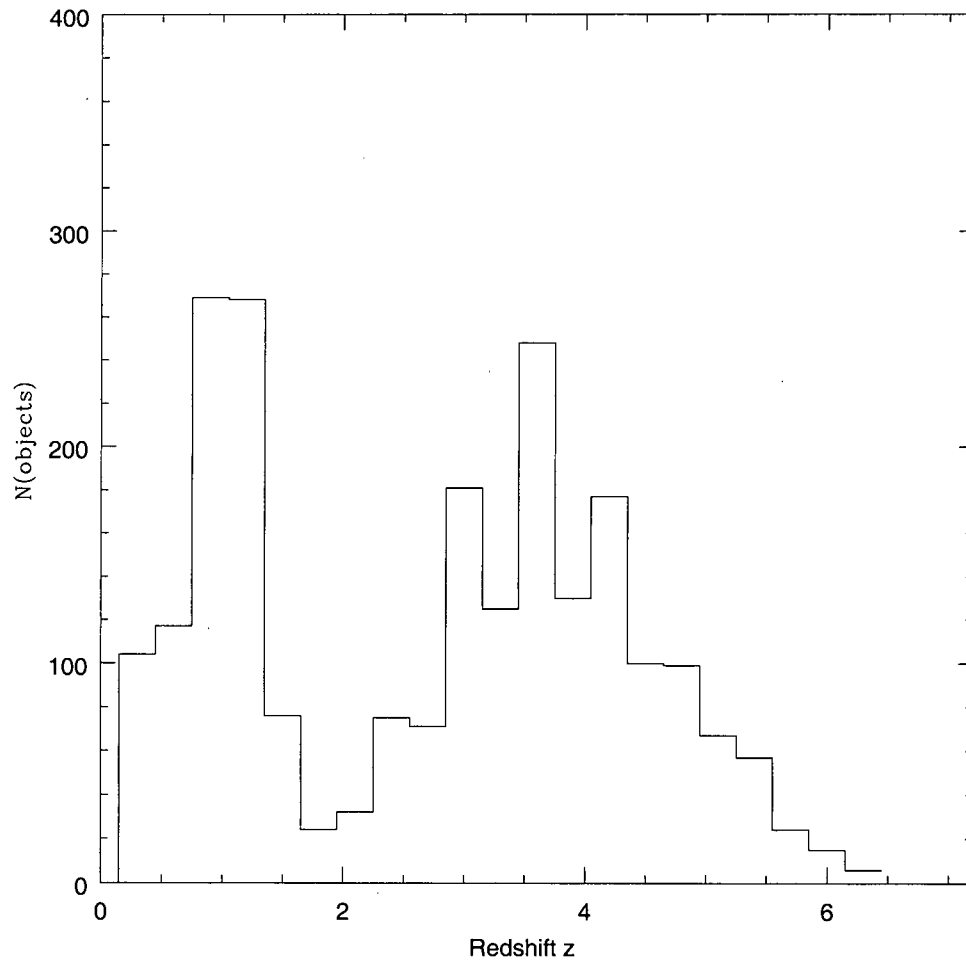


Figure 5.13: The number - redshift distribution for the “cleaned” set of quasars.

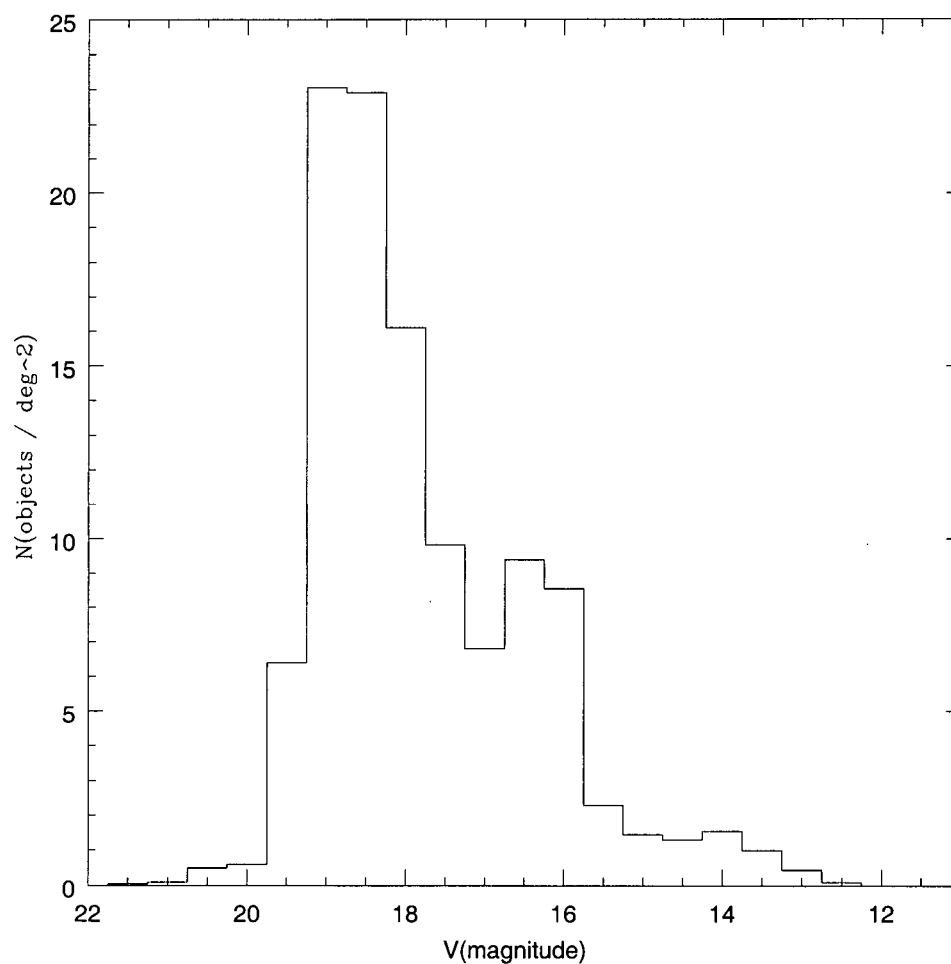


Figure 5.14: The number - V magnitude distribution for the “cleaned” set of quasars.

expected and it is likely this list still includes misclassified objects. Diagrams in Fig. 5.13, 5.14 and 5.15 show the distribution in redshift, magnitude and spectral index using the new quasar candidate sample: these plots are now

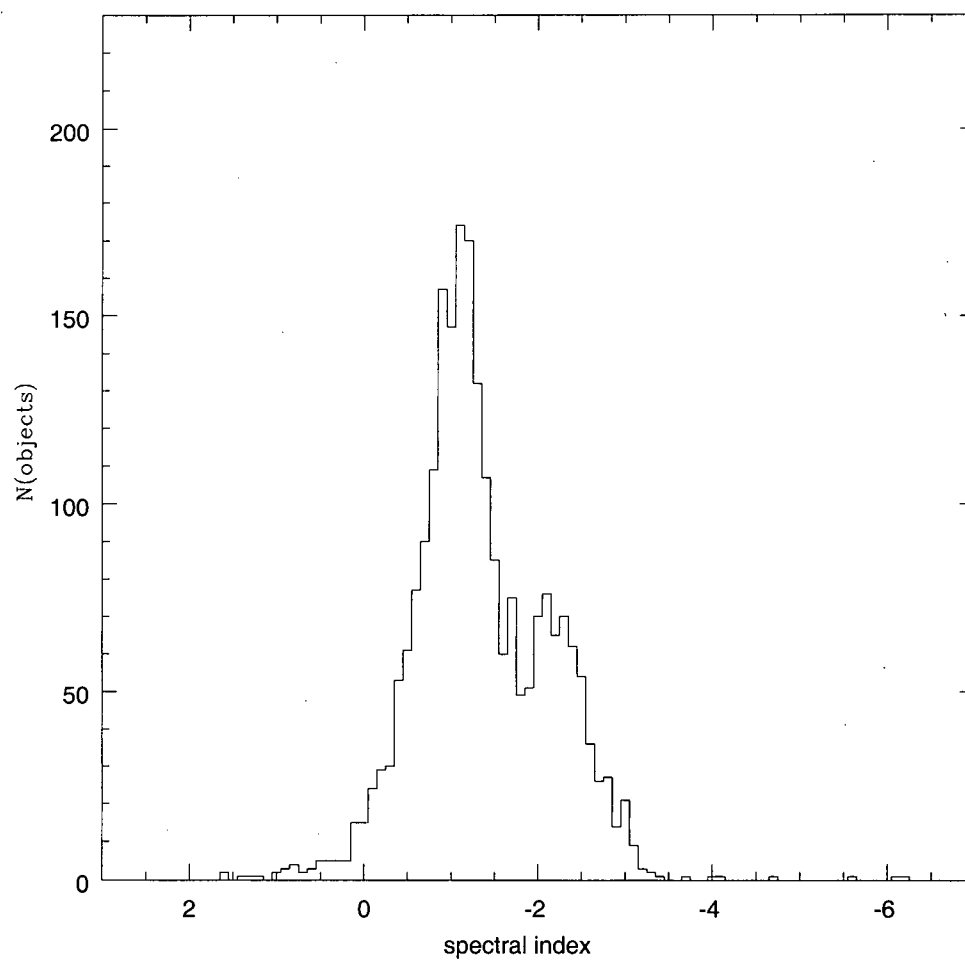


Figure 5.15: The number - α distribution for the “cleaned” set of quasars.

more consistent with the knowledge that we have about quasars and no other criteria seem possible to further reduce the quasar candidate list.

5.5 Identification.

As another way to test the reliability of quasar candidates, the UNMS1 quasar catalog was cross-correlated with Veron's database [75], which, recently updated after the first release of the 2dF quasar catalogue (Croom et al.), now includes 23760 quasars, 608 BL Lac objects and 5751 active galaxies (of which 2765 are Seyfert1s).

In the region observed by the LMT Survey ($12^h \leq \alpha \leq 18^h$, $32.5^\circ \leq \delta \leq 33.5^\circ$), Veron's catalog has 100 quasars among which 1 is in common with the quasar candidate catalog found in this thesis. Since the unavailability of optical SEDs, the cross-correlation was done using the object position and visual brightness.

Table 5.7 shows coordinates, V magnitude and redshift of this object.

	VERON	UNMS1
NAME	RX J1730.0+3301	
RA	17:30:4	17:30:4
DEC	33:01:02	33:01:05
V	17.9	16.43
z	0.632	0.62

Table 5.7: Equatorial coordinates (RA, DEC), apparent V magnitude and redshift z for the quasar common to Veron's catalog and UNMS1 quasar catalog.

CHAPTER 6

SUMMARY AND CONCLUSIONS.

This thesis has attempted to develop a method to identify quasars from stars and galaxies included in the UNMS1 catalog, compiled from observations taken in 1996-1997 and 1999 with the NODO Liquid Mirror Telescope.

The method proposed in this thesis is based on a χ^2 minimization procedure combined with a Bayesian approach. The χ^2 parameter (eq. 4.12), between the theoretical and observed SED, estimates how well a SED model fits the data. The odds ratio (eq. 4.15), from Bayes' theorem, includes other important considerations: it accounts for the number of models, which differs from category to category (131 stellar templates, 1573 galaxy templates and 1344 quasar templates), and our prior knowledge of the number of quasars to be expected in 1 degree square at a particular magnitude (surface densities are generally obtained from other surveys).

The method was first tested on templates: each was treated as test object, modified by adding noise, resampling the flux measurements in a jackknife approach and analysed in terms of χ^2 and odds ratio. It was found that 1082 template-objects of 3048 are misclassified: using the notation of Table 4.7, type-I quasars are confused with UVhot, elliptical and spiral galaxies, type-II quasars are mainly classified as starburst and late spiral galaxies, and G and F stellar types, type-III quasars are mostly seen as F type stars and type-IV

quasars as B type stars.

An important step was to realize how important the number of reliable magnitudes is on classifying objects correctly : in the UNMS1 catalog most of the sources have 10 - 20 filters and only 35% of the entire database have more than 35 flux measurements. If important spectral features are missed, it is easy to misclassify objects. The final test was to analyse method's results when more and more filters are randomly neglected. From the distribution of stars, galaxies and quasars (Fig. 4.16), two features appear: the number of stars increases and the number of quasars decreases when more and more filters are randomly neglected. However, the galaxy distribution is almost flat. This situation and further studies described in §4 leads us the conclusion that, in order to classify galaxies properly, with an accuracy of 85% or higher, 20 flux measurements or more are required. To classify stars and quasars, it is necessary to have 30 or more flux measurements.

The method, applied to the UNMS1 sources satisfying the above criterion and more separated by more than 3 arcsec, produced the results summarized in Table 6.1:

Category	Object NUM.
STAR	25193
GALAXY	10791
QUASARS	3056
TOT.	39040

Table 6.1: Distribution of star, galaxy and quasar candidates.

Comparing surface density values cited in §4 with these results, there are

more quasars than what are expected.

Useful results are obtained from the quasar candidate distribution in redshift, magnitude and spectral index: there are many objects brighter than magnitude 16, localized at redshift higher than 4, and with the spectral index α lower than -3.5.

Considering that bright objects cannot be too distant (otherwise they would emit an extremely large amount of energy) and that, generally, quasar spectra can be well fitted by a power law with spectral index in the range $[-2.5, 1]$, sources satisfying the following criteria are not considered reasonable quasar candidates:

- $V \text{ mag} < 16$ and $z > 3.5$;
- $V \text{ mag} < 16$ and $\alpha < -3$;
- $z > 3.5$ and $\alpha < -3$.

After this “cleaning procedure”, the new quasar sample includes 2294 objects: it is likely there are still misclassified quasars, but we cannot identify any new selection criteria to further refine our catalog.

From the cross-correlation of our quasar list with Veron’s quasar catalog, which has 100 objects in the sky region observed with the NODO-LMT, 1 object was identified; basic parameters are shown in Table 5.7.

BIBLIOGRAPHY

- [1] Allen, C.W, 1973, *Astrophysical Quantities*, 3rd ed. Athlone Press, London.
- [2] Bachiller, R. et al., 1996, *Annual Review in Astronomy and Astrophysics*, Vol. 34.
- [3] Beauchemin, M., 1985, M.Sc. Thesis, Laval University.
- [4] Bevington, P. R., Robinson, D. K., 1992, *Data reduction and error analysis for the physical sciences*, ed. S. J. Tubb and J. M. Morris, USA.
- [5] Binggeli, B., Sandage, A., Tammann, G.A., 1988, *Annu. Rev. Astron. Astrophys.*, 26, 509.
- [6] Binney, J., Merrifield, M., 1998, *Galactic Astronomy*, ed. Princeton University Press, Princeton, New Jersey.
- [7] Borra, E.F., astro-ph/950319.
- [8] Borra, E.F., Moretto, G., Wang, M., 1995, *A&A*, 109, 563.
- [9] Borra, E.F., astro-ph/9706098.
- [10] Borra, E.F., Ritcey, A., Artigau, E., astro-ph/9901295.
- [11] Boyle, B.J., Fong, R., Shanks, T., Peterson, B.A., 1990, *MNRAS*, 243, 1B.

-
- [12] Boyle, B.J., Shanks, T., Jones, L.R., 1991, MNRAS, 251, 482B.
- [13] Burbidge, Geoffrey & Margaret 1967, *Quasi-Stellar Object*, ed. W.H.Freeman and Company, San Francisco.
- [14] Cabanac, R.A., astro-ph/9706156.
- [15] Cabanac, R.A., de Lapparent, V., Hickson, P., astro-ph/0206062
- [16] Carroll, B.W, Ostlie, D.A., 1996, *An Introduction to Modern Astrophysics*, ed. Addison-Wesley Publishing Company, United States of America.
- [17] Cristiani, S., Barbieri, C., Iovino, A., La-Franca, F., 1989, A&A, 177, 161C.
- [18] Cristiani, S. et al., 1995, A&A, 112, 347C.
- [19] Dressler, A., 1980, ApJ, 236, 51.
- [20] Fairall, A., 1998. *Large-scale structures in the Universe*, ed. John Wiley & Sons, New York.
- [21] Fan, X. et al., 2001, AJ, 122, 2833F.
- [22] Fanti, Carla & Roberto, 2000, *Lezioni di Radioastronomia*, Dipartimento di Astronomia, Bologna.
- [23] Foster, K., Green, P.J., & Aldcroft, T.L., Vestergaard, M., Foltz, C.B., Hewett, P.C., 2001, ApJS, 134, 35F.

-
- [24] Francis, P.J., Hewett, P.C., Foltz, C.B., Chaffee, F.H., Weymann, R.J., Morris, S.J., 1991, *ApJ*, 373, 465F.
- [25] Gibson, B.K., 1991, *JRASC*, 85, 158.
- [26] Gilmozzi, R., *Science with 100 m telescope*, 2000, SPIE 4005.
- [27] Goldschmidt, P. et al., 1991, *The Space Distribution of Quasars*, proc. 93G.
- [28] Grazian, A., Cristiani, S., D'Odorico, V., Omizzolo, A., Pizzella, A., 2000, 119, 2540-2555.
- [29] Grebel, E.K., astro-ph/0105138.
- [30] Gregory, P.C., 2002, *Statistical Inference in Science: Bayesian and Frequentist Perspectives*, PHYS509 notes.
- [31] Groote, D., Reimers, D., Wohler, T., Wisotzki, L., 1996, *A&A*, 115, 227W.
- [32] Hagen, H-J., Engels, D., Reimers, D., 1999, *A&A*, 134, 483.
- [33] Hatziminaoglou, E., Mathez, G., Pello', R., 2000, *A&A*, 359, 9H.
- [34] Hewett, P.C., Foltz, C.B., Chaffee, F.H., 1995, *AJ*, 109, 1498H.
- [35] Hewitt, A., Burbidge, G., 1993, *ApJS*, 87, 451H.
- [36] Hickson, P., Gibson, B.K., Borra, E.F., Content, R., 1990, project description.

-
- [37] Hickson, P., Walker, G.A.H., Borra, E.F., Cabanac, R.A., 1994, SPIE, 2199, 922.
- [38] Hickson, P., Borra, E.F., Cabanac, R.A., Content, R., Gibson, B.K., Walker, G.A.H., 1994, ApJ, 436, 201H.
- [39] Hickson, P., Mulrooney, M.K., 1998, ApJS, 115, 35.
- [40] Hickson, P., Richardson, E.H., 1998, PASP, 110, 108 .
- [41] Hickson, P., Mulrooney, M.K., 1998, ApJ, 506, 191.
- [42] Hickson, P., 2002, MNRAS, 330, 540H.
- [43] Jenkner, H., Lasker, B.M, Sturch, C.R., McLean, B.J., Shara, M.M., Russel, J.L., 1990, AJ, 99, 2082.
- [44] Kinney, A.L., Calzetti, D., Bohlin, R.C., McQuade, K., Storchi-Bergmann, T., Schmitt, H.R., 1996, ApJ, 467, 38K.
- [45] La-Franca, F., Cristiani, S., Barbieri, C., 1992, AJ, 103, 1062L.
- [46] La-Franca, F., Cristiani, S., 1997, AJ, 113, 1517L.
- [47] Lasker, B.M. et al. 2000, 119, 2540-2555.
- [48] Lasker, B.M., Sturch, C.R., McLean, B.J., Russel, J.L., Jenkner, H., Shara M.M., 1990, AJ, 99, 2019.
- [49] Malkan, M.A., Sargent, W.L.W., 1982, ApJ, 254, 22M.
- [50] Marzke, R., Geller, M., Huchra, J.P., Corwin, H.G.J., 1994, ApJ, 108, 437MM.

-
- [51] McGraw, J.T., Angel, J.R.P., Sargent T.A., 1980, *In Application of Digital Image Processing to Astronomy*, ed. Eliot D.A. (Bellingham: SPIE), 20.
- [52] Mitchell, K.J., Warnoch, A., Usher, P.D., 1984, ApJ, 287L, 3M.
- [53] Mitsouras, D., Brandenberger, R., Hickson, P., astro-ph/9806360.
- [54] Monet, D., 1996, A&A, 188, 5404.
- [55] Monet, D. et al., 1997, USNO1, C, 0M .
- [56] Pickles, A. J., 1998, AJ, PAPS 110, 863.
- [57] Potter, A.E., Mulrooney, M., 1997, AdSpR, 19, 213P.
- [58] Richstone, D.O., Schmidt, M., 1980, ApJ, 235, 361R.
- [59] Rocca-Volmerange, B., Guiderdoni, B., 1988, A&AS, 75, 93R.
- [60] Russel, J.L, Lasker, B.M., McLean, B.J., Sturch, C.R., Jenkner, H., 1990, AJ, 99, 2059.
- [61] Sandage, A.R., Veron, P., 1965, ApJ, 142, 412.
- [62] Schmidt, M., 1963, Nature, 197, 1040.
- [63] Schmidt, M., Green, R., 1983, AJ, 269, 352.
- [64] Scholz, R.D., Meusinger, H., Irwin, M., 1997, A&A, 315, 417S.
- [65] Schneider, D.P., Schmidt, M., Gunn J.E., 1994, AJ, 107, 1245S.
- [66] Schneider, D.P. et al., 2002, AJ, 123, 567.

-
- [67] Schweizer, F., 1990, *Dynamics and Interactions of Galaxies*, ed. Wielen, R., (Berlin: Springer), p.60, Observational phenomena associated with mergers.
- [68] Shanks, T. et al., astro-ph/0003206.
- [69] Shields, G.A., 1978, Nat, 272, 706.
- [70] Skey, H., 1872, Trans. New Zealand. Inst., 5, 119.
- [71] Storrie-Lombardi, L.J., McMahon, R.G., Irwin, M.J., Hazard, C., 1996, ApJ, 468, 121S.
- [72] Storrie-Lombardi, L.J., Irwin, M.J., McMahon, R.G., Hook I.M., astro-ph/0012446.
- [73] Unsold, A., Baschek, B., 1991, *The New Cosmos.*, 4th ed. Springer-Verlag, Berlin.
- [74] Vanden-Berk, D.E. et al., 2001, AJ, 122, 549V.
- [75] Veron-Cetty, M.P., Veron, P., 2001, A&A, 374, 92V.
- [76] Voges, W., 1992, *Environment Observation and Climate Modelling Through International Space Projects: Space Sciences with Particular Emphasis on High Energy Astrophysics.*, (Noordwijk:ESA), 9-19(RASS).
- [77] Warren, S.J., Hewett, P.C., Osmer, P.S., 1991, ApJS, 76, 23W.
- [78] Zheng, W., Kriss, Z.G.A., Telfer, R.C., Grimes, J.P., Davidsen, A.F., 1997, ApJ, 475, 469Z.

-
- [79] Zheng, W., astro-ph/0005247.